Controlling Two-Phase Flow in Microfluidic Systems using Electrowetting


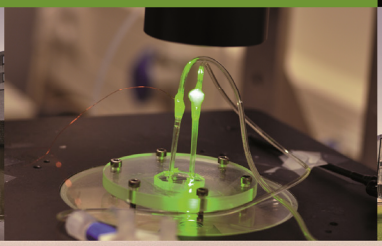


Hao Gu

Controlling Two-Phase Flow in Microfluidic Systems using Electrowetting

Hao Gu

The research described within this thesis was carried out in the Physics of Complex Fluids group at the IMPACT and MESA+ Institutes at the University of Twente, Enschede, the Netherlands. The MicroNed programme, part of the Decree on subsidies for investments in the knowledge infrastructure (Bsik) from Dutch government, financially supported this research.

Thesis committee members

Chairman:
Prof. dr. G. van der Steenhoven University of Twente

Promotor:
Prof. dr. F. Mugele University of Twente

Assistant Promotor:
Dr. M. H. G. Duits University of Twente

Other members:
Prof. dr. ir. R. M. Boom Wageningen University
Prof. dr. ir. A. van den Berg University of Twente
Prof. dr. J. G. E. Gardeniers University of Twente
Prof. dr. ir. R. G. H. Lammertink University of Twente

Title: Controlling two-phase flow in microfluidic systems using electrowetting
Author: Hao Gu
ISBN: 978-90-365-3156-6
DOI: 10.3990/1.9789036531566

Cover design and photography: Lanti Yang and Hao Gu
Printed by Ipskamp Drukkers B.V., Enschede, The Netherlands, 2011.

CONTROLLING TWO-PHASE FLOW IN MICROFLUIDIC SYSTEMS USING ELECTROWETTING

DISSERTATION

to obtain
the degree of doctor at the University of Twente,
on the authority of the rector magnificus,
prof. dr. H. Brinksma,
on account of the decision of the graduation committee,
to be publicly defended
on Friday, 18th of March, 2011 at 12:45

by

Hao Gu

born on June 11th, 1979
in Beijing, China

This dissertation has been approved by:

Promotor:	Prof. dr. Frieder Mugele
Assistant Promotor:	Dr. Michel H. G. Duits

This thesis is dedicated to my parents, my wife and my baby daughter

Contents

Chapter 1

General Introduction

1.1 The Development of Microfluidics

In the last two decades, the development of microfluidics has shown a strong upsurge. In the beginning, microfluidics was applied for ink jet printing and a few other applications, for instance feeding droplets into micro-motors. Nowadays, microfluidics can be found in numerous applications, such as emulsification, chemical synthesis, biomedical diagnostics, drug screening and more.[1-4] Compared to conventional techniques, microfluidic technology offers several unique advantages like (i) much less volume of sample or reagents is used, which is practical and reduces costs; (ii) the results (diagnostic) or the products (chemistry and biology) are obtained in a shorter time, because the high surface-to-volume ratios at the microscale lead to shorter heat and mass transfer times; (iii) miniaturization allows for an increase in parallelization and automation. For instance it offers a way of screening and systematic testing in the domain of drug discovery.

However, there are still some challenges in the development of microfluidic systems. The most important one is the integration of all the components of the system on one chip, which means pumps, valves, channels *etc.* must be miniaturized in order to obtain an integrated system. It raises questions about choosing energy sources between active methods – efficient but difficult to miniaturize due to extra parts, and passive methods – easier to integrate but less efficient. Another challenge is that the rising complexity of the devices also imposes higher demands on the microfabrication technologies. Many multi-functional devices nowadays involve composite materials consisting of a number of chemically different structures like layers or electrodes, each of which has to be introduced without affecting the functional materials or structures that are already present.

1.2 Droplet Microfluidics

In initial development of microfluidics, mostly continuous flow systems were considered. These systems are more or less derived from macroscopic devices. The reagents consumption is less and the processing time is shorter compared to conventional technology. However, the desire to further downscale the amounts of reagents and to further minimize the processing time have remained as a driving force in the development of microfluidics. In recent years, droplet-based microfluidics has become more and more attractive due to the dramatic reduction in reagent volume and reaction time it can offer. A second advantage of using droplets is that contact with solid walls is eliminated. This strongly reduces problems due to adsorption of dissolved components to the channel walls, and increases the efficiency of chemical reactions. And thirdly, new functionalities can be implemented: simple Boolean logic functions can be performed in droplet microfluidic systems.[5-7]

One of the commonly used platforms for droplet microfluidics is so-called digital microfluidics (DMF), which is mainly based on the use of electrowetting (EW) to manipulate individual droplets as digital entities on a planar surface. The other popular platform is based on structures containing closed microchannels. There discrete droplets are produced and manipulated in an immiscible continuous flow. It can be considered as a subset of the more general two-phase flow systems (TPF). Both platforms differ considerably from each other: DMF provides precise control over individual droplet, such as transport, splitting, merging and mixing. On the other hand, TPF is suitable for the treatment of micro-droplets at high throughput in continuous processes.

1.2.1 Electrowetting and digital microfluidics

Electrowetting refers to an electrostatically induced reduction in the contact angle of an electrically conductive liquid droplet on a surface. As early as 1857, the EW effect was described by Gabriel Lippmann.[8] In the early 1990s, Berge *et al.* introduced the concept of separating the electrode and the conductive liquid by a thin insulating layer to eliminate the problem of electrolysis.[9] Since then many applications based on EW have seen the light. In recent years it has emerged as one of the most flexible and reliable methods to modulate surface tension and

hence manipulate droplets with volumes ranging from O(nL) to O(mL).[10-13]

The most commonly used EW-based system is digital microfluidics, in which manipulations are carried out on the surface of a planar substrate, or between two substrates. Successive actuation of electrodes is used to digitally activate targeted droplets. Droplets are initially produced from a reservoir, then transported from one electrode to the next one, merged with other droplets for desired reaction and further mixed for complete reaction. It is also possible to split droplets and transport them to an exit.

EW-based DMF offers several advantages for lab-on-a-chip applications. First, no external microvalves are needed, since EW provides the actuation force; Second, individual control over droplets is possible since EW can be applied very locally using micro electrodes; Third, EW-based DMF allows for a high level of automation and integration: all manipulations can be performed on one digital microfluidic device. However, there are still some limitations that need to be addressed, such as sample contamination, droplet sticking and the relatively low throughput.

1.2.2 Droplet-based two-phase flow microfluidics

As mentioned, another approach to manipulate droplets is via two-phase flow. In TPF, discrete droplets are produced and transported by a continuous flow of an immiscible liquid through closed microchannels. This approach offers possibilities for producing droplets with diameter in the nanometer or micrometer range in a controlled and reproducible manner, also with a high throughput. For lab-on-a-chip applications, the generated droplets can be regarded as microreactors (single droplet or merged droplets) to perform chemical or biochemical reactions. In general, droplet-based TPF is well adapted to continuous processes, for instance the production of a large number of encapsulated biological targets.[3-4, 14-15]

Practically, the manipulation of droplets with high precision and flexibility is still a central issue, for example generating droplets on-demand or merging droplets at certain location is still challenging. Extensive investigations with different approaches for manipulating droplets, in terms of formation, merging, splitting

and sorting of droplets are currently explored by many researchers.

Surfactants play an important role in TPF to stabilize droplets by reducing the surface tension between dispersed and continuous phases. By residing at the interface of the two fluid phases with their hydrophilic heads in the aqueous phase and hydrophobic tails in the oil phase, surfactants can turn unstable emulsion droplets into metastable colloids. An unavoidable consequence of this stabilization is that it also becomes more difficult to let two such droplets merge when this is needed.

The wettability of the channel surfaces is also essential for droplet-based TPF. The continuous phase should favor the channel surface, while the dispersed phase should dislike the channel surface. For instance, water droplets suspended in oil need hydrophobic channels, whereas oil-in-water emulsions require hydrophilic channels. Therefore, the materials used for fabricating microchannels and surface modification technologies are quite important for producing and manipulating droplets.

1.3 Aim and Outline of this Thesis

From the foregoing analysis it is clear that EW-based DMF and droplet-based TPF each have their advantages and disadvantages, and that these two systems are in fact complementary. This offers an interesting potential for the development of microfluidic systems in which both approaches are combined.

The aim of this work is to explore the combination of EW technology and droplet-based TPF platform, which would bring the advantages of both worlds together: (i) high throughput (from pressure-driven channel-based TPF) and (ii) precise control over each individual droplet (from EW). To achieve this goal, different approaches and microfabrication technologies have been explored in this thesis work. Also the (potential) functionalities of such chips have been explored and demonstrated.

Chapter 2 presents an overview on EW, covering the basic principle, as well as key aspects such as the conductivity of aqueous phase, contact angle saturation and hysteresis, and contact line motion. EW-based DMF is discussed in terms of

its operations and suitability for lab-on-a-chip applications. In the same chapter, we also review the state-of-the-art in droplet-based TPF with particular emphasis on droplet formation and droplet merging under both hydrodynamic and electric control conditions. Also novel microfabrication methods for TPF are discussed.

In **Chapter 3**, we discuss the integration of insulator-covered electrodes (EW capacity) into a microfluidic flow focusing device (FFD). We demonstrate how EW can assist the formation of water droplets in a continuous oil phase and identify experimentally a specific region where droplet formation can be triggered by EW. A theoretical description based on the balance of external inlet pressures and a voltage-dependent capillary pressure will be compared to the observations.

We demonstrate a flexible and high throughput droplet formation based on EW and pressure-driven flow in **Chapter 4**. We will show that with the integration of EW, the droplet size and droplet generation frequency can be tuned with much better precision than hydrodynamic control, accessing also novel drop generation scenarios with variable charge (such as conical spray mode with charged micron-sized drops). In this regime, monodisperse tiny drops with only a few microns in diameter or even smaller can spray out off an orifice with a generation frequency of the order of kHz.

In **Chapter 5**, we present a simple, rapid and inexpensive method to fabricate microchannels with insulator-covered EW electrodes. Use of a thiolene precursor allows defining the channel geometry via soft imprint lithography, as well as bonding of the chip via exposure to UV light. Compared to earlier poly-dimethylsiloxane (PDMS)-based designs, this method allows to make micro-channels with smaller dimensions, lower aspect ratios, and electrodes on both the bottom and top of the channel. The enhanced capabilities with the EW functionality are demonstrated with two examples: droplet formation and the displacement of oil by water (imbibition).

In **Chapter 6**, we demonstrate a microfluidic platform in which (programmable) local electric fields originating from embedded and protected electrodes are used to control the formation and merging of droplets in a microchannel, *on-demand*. EW-based droplet-on-demand (DOD) offers the possibility of synchronizing the

formation of droplets, which can be used for subsequent operations. One of these is the merging of two droplets, which is achieved via electrocoalescence (EC).

The last experimental part of this thesis, **Chapter 7** deals with the development and testing of a tensiometric device, that makes use of a tapered channel and control over the hydrostatic pressures of oil and water. Since in such a channel the mean curvature of the interface depends on the axial position, mechanical equilibrium will be achieved only at a certain axial location. This allows to measure the interfacial tension, either at equilibrium or when it is slowly changing.

The overall summary and outlook are presented in **Chapter 8**. The detailed experimental process documents are included in **Appendix**. Most of the work described in this thesis has been published or will be published in the near future (see **Publication List**).

References

1. H. A. Stone, A. D. Stroock and A. Ajdari, *Annu Rev Fluid Mech*, 2004, **36**, 381-411.
2. H. Song, D. L. Chen and R. F. Ismagilov, *Angew Chem Int Edit*, 2006, **45**, 7336-7356.
3. S. Y. Teh, R. Lin, L. H. Hung and A. P. Lee, *Lab Chip*, 2008, **8**, 198-220.
4. D. Mark, S. Haeberle, G. Roth, F. von Stetten and R. Zengerle, *Chem Soc Rev*, 2010, **39**, 1153-1182.
5. M. J. Fuerstman, P. Garstecki and G. M. Whitesides, *Science*, 2007, **315**, 828-832.
6. M. Prakash and N. Gershenfeld, *Science*, 2007, **315**, 832-835.
7. M. Schindler and A. Ajdari, *Phys Rev Lett*, 2008, **100**, 044501.
8. G. Lippmann, *Ann Chim Phys*, 1875, **5**, 494.
9. B. Berge, *C. R. Acad. Sci.*, 1993, **II 317**, 157.
10. F. Mugele and J. C. Baret, *J Phys-Condens Mat*, 2005, **17**, R705-R774.
11. R. B. Fair, *Microfluid Nanofluid*, 2007, **3**, 245-281.
12. F. Mugele, *Soft Matter*, 2009, **5**, 3377-3384.
13. M. Jebrail and A. Wheeler, *Curr Opin Chem Biol*, 2010, **14**, 574-581.
14. C. N. Baroud, F. Gallaire and R. Dangla, *Lab Chip*, 2010, **10**, 2032-2045.
15. L. Shui, S. Pennathur, J. C. T. Eijkel and A. van den Berg, *Lab Chip*, 2008, **8**, 1010-1014.

Chapter 2

Electrowetting and Droplet Microfluidics*

2.1 Introduction

In recent years, microfluidic devices based on manipulation of discrete droplets have attracted growing attention. Electrowetting (EW)-based digital microfluidic systems (DMF) and two-phase flow microfluidic systems (TPF) are both widely used platforms at present. In general, DMF provides precise control, such as merging, splitting, mixing and handling, over each individual droplet. This makes the platform well adapted to biodiagnostics and biorecognition. On the other hand, TPF is well suited to the treatment of small droplets at high throughput in continuous processes, like producing and sorting.

In section 2.2, we will give an overview on EW, covering the basic theory and including practically relevant aspects such as the conductivity of aqueous phase, contact angle saturation and hysteresis. Then finally EW-based DMF is discussed. In section 2.3, a review on current developments in TPF is presented. We focus especially on two main operations: droplet formation and merging. Also innovative microfabrication methods for TPF will be discussed. This overview chapter will highlight the advantages and disadvantages of both EW-based method and TPF-based technique separately. It will become clear what the potential benefits are if we combine both approaches.

2.2 Electrowetting

The EW effect was first described in 1875 by Gabriel Lippmann, who studied electrocapillarity phenomena in water, mercury and air in contact with each other.[1] Approximately two decades ago, Berge *et al.* introduced the concept of a thin insulating layer to separate the electrode and the conductive liquid in order

* Portions of this chapter has been submitted to Int. J. Mol. Sci. (invited review)

to eliminate the problem of electrolysis.[2] This concept has also become known as electrowetting on dielectric. Initially, applications included electrometers and ink jet printing. More recently, EW has also become a popular tool for the actuation of tiny amounts of liquid in microfluidic systems, via a modulation of the local contact angle of a liquid and its underlying substrate.[3] In this section the basic principle of EW will be explained, along with its working ranges and limitations. Subsequently an overview of the current applications of EW, in particular the "digital microfluidics toolbox" will be presented.

2.2.1 Basic principle

Electrowetting is the phenomenon whereby the contact angle of a conductive liquid on a dielectric-coated electrode reduces under the influence of an external electrical field applied across the solid/liquid interface. In essence, the wetting property of a polarizable and/or conductive liquid in contact with a hydrophobic, insulated electrode can be modified by the electrical field. The classical EW configuration (see Fig. 2.1) comprises a planar solid electrode surface covered with a thin dielectric material. In case the latter is not hydrophobic, it is coated with an additional thin hydrophobic layer. A conducting wire is plunged into the droplet to close the electrical circuit. Application of an electric potential between the solid electrode and the aqueous liquid then allows a quantitative control over the deformation of the liquid surface.

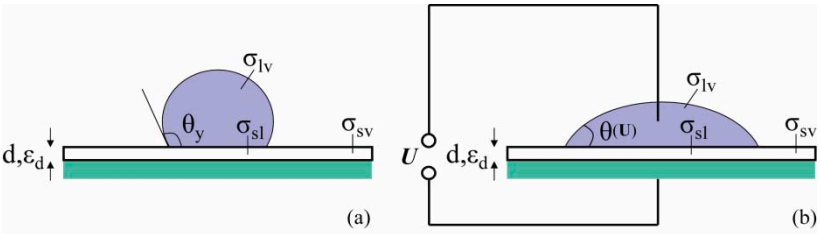

Figure 2.1 Standard EW setup. d is the thickness of insulator. (a) Droplet with Young's contact angle θ_y without applying voltage. (b) Droplet with reduced contact angle $\theta(U)$ at finite voltage.

In most practical cases the droplets have a typical size of 1 mm and contain an aqueous salt solution. Air or an immiscible liquid, frequently an oil, is utilized as the ambient medium. Under typical conditions, the so-called Bond number, $Bo = \Delta\rho g L^2/\sigma$ which measures the relative strength of gravity and surface tension, is

smaller than unity. Thus gravity can be neglected and surface tension dominates the behavior of the droplets.

The Helmholtz free energy F is then a functional of the droplet shape. F contains two contributions. F_{surf} is due to the surface energies with i (i = lv (liquid-vapor), sl (solid-liquid) and sv (solid-vapor)). Here we denote the ambient medium as vapor for simplicity. The other contribution is the electrostatic free energy F_{el}:

$$F = F_{surf} + F_{el} = \sum_i \sigma_i A_i - \int \frac{1}{2} \vec{E}\vec{D} dV \tag{2.1}$$

$\vec{E}$ and $\vec{D}$ denote the electric field and the electric displacement. Note that the negative sign of the electric contribution results from considering the entire system that includes both the droplet and the power supply ("battery") required to apply the voltage. In the absence of an external electric field, the minimization of F under the constraint of constant droplet volume leads to a spherical-cap equilibrium shape for the droplet, with a contact angle θ_Y given by the Young-Laplace equation:

$$\cos\theta_Y = \frac{\sigma_{sv} - \sigma_{sl}}{\sigma_{lv}} \tag{2.2}$$

When a voltage is applied between the droplet and the counter-electrode, electrical charges are generated on both sides of the insulating layer: a charge on the lower electrode, and a counter-charge at the bottom of the aqueous phase. In this picture, both the electrode and the aqueous phase act like perfect conductors. In reality, the spatial distribution of the charges can be more complex, but for most purposes the assumption of an ideally conducting fluid with a surface charge density is sufficiently precise. Then the electrical contribution to F can be modeled using a parallel plate capacitor with area A_{sl} and thickness d_{ins}.

$$F_{el} = -\frac{1}{2} \frac{\varepsilon\varepsilon_0}{d_{ins}} U^2 A_{sl} \tag{2.3}$$

Here ε is the dielectric constant of the insulator, ε_0 is the dielectric constant of vacuum, and U is the applied voltage. Then Eq. 2.1 can be rewritten as:

$$F = \sigma_{lv} A_{lv} + (\sigma_{sl} - \sigma_{sv} - \frac{1}{2}\frac{\varepsilon\varepsilon_0}{d_{ins}} U^2 \cdot \Phi_{el}(\vec{r}))A_{sl} \qquad (2.4)$$

Here $\Phi_{el}(\vec{r}) = 1$ where $\vec{r}$ coincides with the electrode and zero elsewhere. If we consider a single homogeneous electrode ($\Phi_{el} \equiv 1$), this equation shows a similar form as Eq. 2.1, but now with an electric term that gives rise to a modified prefactor for A_{sl}. Therefore, based on free energy minimization, combining Eq. 2.4 and Eq. 2.2, we obtain the basic equation for EW:

$$\cos\theta = \cos\theta_Y + \frac{\varepsilon_0\varepsilon_d}{2d\sigma_{lv}} U^2 = \cos\theta_Y + \eta \qquad (2.5)$$

Here, $\eta = \varepsilon_0\varepsilon_d U^2/2d\sigma_{lv}$ is the dimensionless EW number, which measures the relative strength of electrostatic and surface tension forces. It is now seen that the voltage required to achieve a certain contact angle decrease in EW depends on the properties of the insulating layer. Fig. 2.2 gives a typical outcome of an EW experiment. Indeed a behavior corresponding to Eq. 2.5 is found, as long as the voltage is not too high. Beyond a (system dependent) threshold voltage, the contact angle becomes independent of the applied voltage. This will be discussed in Section 2.2.3.

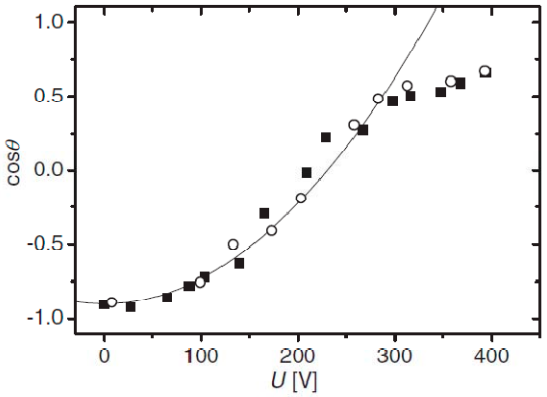

Figure 2.2 Contact angle θ versus applied voltage U_{rms} for advancing (filled squares) and receding (open circles) contact line of water droplet with salt (NaCl, conductivity: 3 mS·cm^{-1}; *ac* frequency 10kHz) surrounded by silicone oil as the ambient medium. Teflon AF 1601 is used as insulator ($d \approx 5$ μm). Solid line: parabolic fit according to Eq. 2.5. Reprinted from [4] with permission from IOP Science.

The theoretical discussion of EW given so far is applicable to both *dc* and *ac* electric fields. However, in the case of *ac* electrowetting, additional physical phenomena may enter the picture. In this light it is useful to distinguish three frequency regimes: 1. at low frequencies (<< 10 Hz), the contact angle and droplet shape can respond fast enough to follow the changes in the voltage amplitude. 2. near the mechanical resonance frequency of the droplet (≈ 100 Hz for a mm sized droplet), strong oscillations in the droplet shape occur. 3. at high frequencies (>> 1000 Hz) the droplet cannot follow the *ac* signal anymore, but still responds to the average of the squared voltage. In this regime, Eq. 2.5 can be used again, but now with the root mean square (rms) value of U.

2.2.2 Conductivity of the aqueous phase

In the basic theory, it was assumed that the liquid is a perfect conductor. However this assumption will ultimately break down when the *ac* frequency is increased. At high frequency, a substantial fraction of the voltage that is applied to the wire, will be spent to drive the ion currents inside the droplet. This effect can be understood by modeling the droplet as an RC (resistor + capacitor) circuit,[5] where the electrical resistance is determined by the salt concentration. If the characteristic time of the *ac* signal becomes shorter than the RC-time of the droplet, then both the voltage at the contact line and the free energy decrease upon moving the latter are reduced. Fig. 2.3 demonstrates this effect for a millimeter-sized droplet of demineralized water.

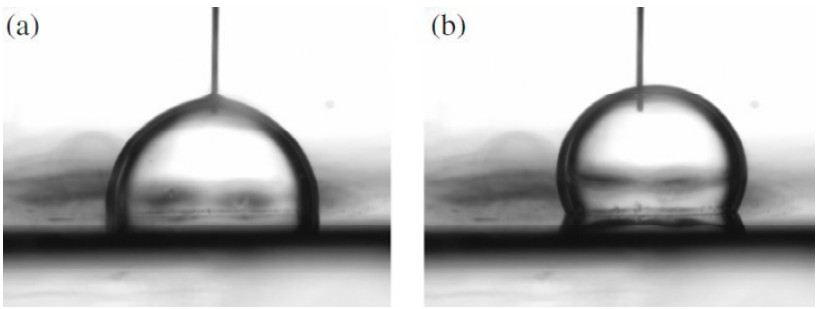

Figure 2.3 Influence of the *ac* frequency on the contact angle (U_{rms} = 50V, droplet: water with NaCl; conductivity is 0.2 mS·cm^{-1}; diameter is approximately 2 mm; ambient medium is silicone oil, insulator is 1 μm thermally grown Si oxide) Reprinted from [6].

Fig. 2.4 illustrates the contact angle versus *ac* frequency for a variety of salt concentrations. At relative low salt concentrations, the liquid shows dielectric behavior. When salt concentrations correspond to 1850 μS·cm^{-1} or higher, the liquid can be considered as a perfect conductor.

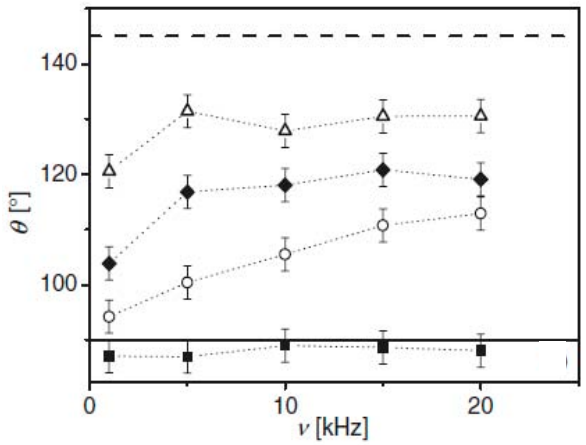

Figure 2.4 Contact angle θ versus *ac* frequency at constant U_{rms} for aqueous droplets with different conductivities: 42 μS·cm^{-1} (Δ), 91 μS·cm^{-1} (♦), 197 μS·cm^{-1} (○) and 1850 μS·cm^{-1} (■). Contact angles in the absence of a voltage, and in presence of a *dc* voltage $U = U_{rms}$ are shown as dashed and solid lines, respectively. Reprinted from [4] with permission from IOP Science.

2.2.3 Contact angle saturation

In principle, according to Eq. 2.5, complete wetting should occur when cosθ equals unity. However it has never been observed experimentally. At relatively low voltage, the applied voltage and the observed contact angle (c.a.) show a parabolic relation (see Fig. 2.2), which is in agreement with Eq. 2.5. On the other hand, at high voltage, the c.a. reaches a saturation value and eventually becomes independent of the applied voltage (see Fig. 2.5a). The physical mechanism of c.a. saturation is still a matter of debate. Several mechanisms explaining c.a. saturation have been proposed: (i) Verheijen and Prins reported that it may be induced by trapping of electric charges in the dielectric film.[7] Results presented by Janocha support the possibility of charge penetration into the polymer dielectric film.[8] (ii) Quilliet and Berge ascribed the contact angle saturation seen in *ac* EW to gas ionization in the vicinity of the sharp droplet edge, and in the *dc* case

to charge trapping in the insulator. (iii) Papathanasiou *et al.* proposed locally dielectric breakdown due to the diverging fields close to the three phase contact line (TPL).[9-11] Fig. 2.5a presents a computed dependence of the c.a. on the applied voltage (solid line) which is in agreement with experimental results (dotted line). In Fig. 2.5b, there is a growing conductive region from the TPL with the increase of applied voltage up to 80 V. Any further increase of voltage does not induce increase of the maximum field strength at the TPL. Notice that this highest strength is lower than 10 MV/cm which is SiO_2 breakdown strength.

Different effects dominate under different experimental conditions. Vallet *et al.* found a particularly interesting effect that is called contact line instability.[12] They observed that at high voltage, an emission of small satellite droplets from the edge of the mother droplet occurs rather than the droplet reaching complete wetting. This observation was later reproduced by Mugele and Herminghaus for mixtures of water and glycerol (see Fig. 2.5c).[13]

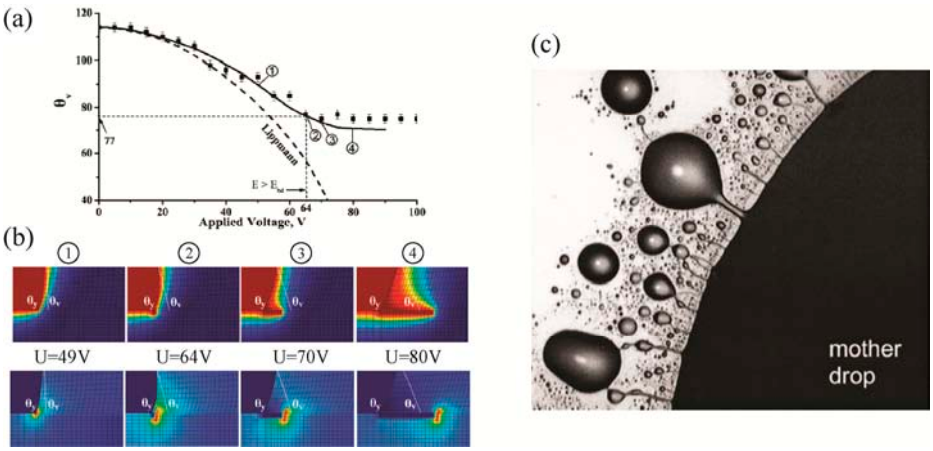

Figure 2.5 (a) Contact angle θ_V is a function of applied voltage for 1 μm SiO_2 as insulator covered with thin Teflon layer. Dashed line: EW equation, Eq. 2.5; solid line: numerical curve based on local dielectric breakdown; dots: experimental data. Symbols ①~④ are selected points which are close to TPL. (b) The potential and the field strength distribution for ①~④, respectively. Reprinted from [11] with permission from the American Chemical Society (ACS). (c) Contact line instability and ejection of satellite droplets at high voltage (U = 600V, f = 300Hz). Image size: approx. 1×1 mm^2. Reprinted from [13] with permission from the American Institute of Physics (AIP).

The qualitative explanation for contact line instability is that electric charges generated at the contact line repel each other. At relative low voltage, surface tension counteracts this electrostatic repulsion. Beyond a threshold voltage however, the electrostatic repulsion becomes too strong and the droplets start to emit small charged droplets, as in the classical Coulomb explosion in three dimensions. Despite this convincing qualitative image, theoretical models that describe this instability have not appeared in literature.

Differences in the saturation angles were also found for the same system, when different voltage waveforms were used. So far there is no unique explanation for contact angle saturation. It seems that diverging electric fields at the contact line can induce several distinct effects. Which of these effects dominate, depends on specific conditions. This is still a topic for further research.

2.2.4 Contact angle hysteresis

Contact angle hysteresis is generally defined as the deviation of the contact angle from its theoretical value (Young's angle) due to physical phenomena like microscopic surface defects and roughness. So-called dynamic hysteresis refers to the advancing and receding contact angles during the motion of an interface. Hysteresis is also observed in electrowetting. For many applications in EW based microsystems, it is (at least a potential) obstacle in moving droplets accurately and reproducibly. Thus it has been a key parameter in many studies to determine aimed at reducing it as much as possible. [7, 14-16]

Li and Mugele demonstrated that the contact angle hysteresis can significantly decrease from 13° to 2° upon application of an *ac* voltage. However using a *dc* voltage turned out to be futile (Fig. 2.6).[14] Their model, based on a balance of surface tension, pinning and electrostatic forces at the contact line, explains the role of the electrostatic force on the behavior of advancing and receding angles. Verheijen and Prins also reported a very low hysteresis (within 2°) on a similar system consisting of an aqueous salt solution surrounded by air on a Teflon AF 1600 surface.[7] For a solid/liquid/liquid system, Paneru *et al*. reported a very low hysteresis, less than 2°, for both *ac* and *dc*.[16] These experiments indicate that the threshold voltage for droplet actuation can be reduced with the decrease of the contact angle hysteresis.

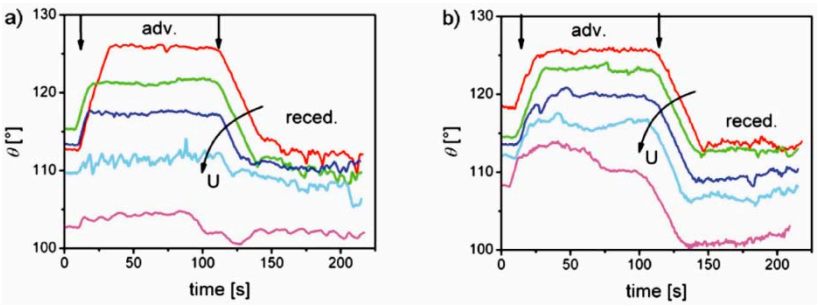

Figure 2.6 Contact angle hysteresis: advancing and receding contact lines for (a) *ac* voltage at f=1 kHz and (b) *dc* voltage. The colored lines indicate 0, 20, 40, 60, and 80V from top to bottom. Reprinted from [14] with permission from the American Institute of Physics (AIP).

2.2.5 Contact line motion

The droplet contact line motion based on EW in ambient oil has been studied by several groups.[17-20] General speaking, the dynamics of droplet motion is determined by the balance between the driving electrostatic forces and viscous dissipation. The viscous dissipation consists of contributions from bulk and contact line. A lubricated contact line can be obtained when a thin layer of the ambient oil is entrapped between the droplet and substrate.

Staicu and Mugele demonstrated this phenomenon and explained the thickness of this thin film of oil by the classical lubrication flow problems of Landau-Levich and Bretherton.[20-21] The thickness can be expressed as $h \approx (d\sqrt{R})^{2/3}(Ca/\eta)^{2/3}$, where R is the three dimensional radius of curvature of the droplet, and Ca is the capillary number ($\mu v/\sigma$; μ: oil viscosity; v: contact line velocity). Eventually the entrapped oil film became unstable due to the competing effects of the electrostatic force and surface tension, and then broke up into droplets.

2.2.6 Digital microfluidics toolbox

Electrowetting provides a very suitable and attractive means to manipulate droplets in microfluidic systems. The principal idea is that the application of a voltage to a series of individually addressable adjacent electrodes (that can be switched on or off) creates asymmetries in the contact angle, which in turn can be used to manipulate droplets.[22] Replacing the wire electrode by a coplanar embedded electrode, allows building microfluidic setups that operate without

any use of pumps or valves. The second strength is that the droplets (with volumes in the nanoliter range) can be independently controlled via a suitable programming of electrode activation sequences. Also a wide variety of aqueous solutions is compatible with EW.[23-24]

A typical DMF platform is shown in Fig. 2.7. Droplets are sandwiched between two parallel plates. The bottom substrate contains the addressable electrode array, and the top surface includes a single ground electrode in electrical contact with the droplet. Generally, the electrodes consist of a (transparent) indium tin oxide (ITO) layer on a glass substrate. At the bottom substrate, the electrode array is covered with an insulating layer. Such insulators can be Teflon,[25] silicon dioxide plus Teflon,[26] Parylene C[27] and SU8[28] *etc*. Both top and bottom surfaces should be hydrophobic to obtain to a large (Young's) contact angle. In addition, the geometrical and chemical heterogeneities should be small to minimize contact angle hysteresis. The distance between the top and bottom plates is fixed by a spacer. Silicon oil or another immiscible liquid is filled in this gap as a surrounding medium that can prevent droplet evaporation and also reduce surface contamination. To achieve reliable droplet actuation, the droplet should be large enough to cover parts of at least four adjacent electrodes at same time, allowing two-dimensional movement. As a consequence, the minimum droplet volume that can be manipulated is also determined by the scale of the electrodes.

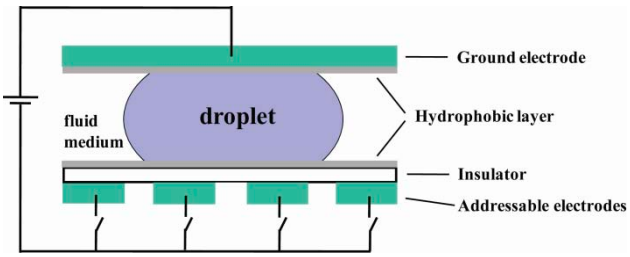

Figure 2.7 A typical digital microfluidic platform. Ground electrode is on the top substrate. By individually activating addressable electrodes that are buried in the bottom substrate, the droplet can be actuated to move from one electrode position to the next.

The ground electrode and addressable electrodes can also be located on one substrate (see Fig. 2.8). This so-called coplanar design has been developed by several groups.[29-33] In this case, the uncoated electrodes exposed at the surface

provide electrical contact to the droplet, making the top plate unnecessary. In practice, a top plate is still used to confine the liquid medium and the droplets. Also, the top plate can be designed for specific chemistry or structures appropriate for different applications.

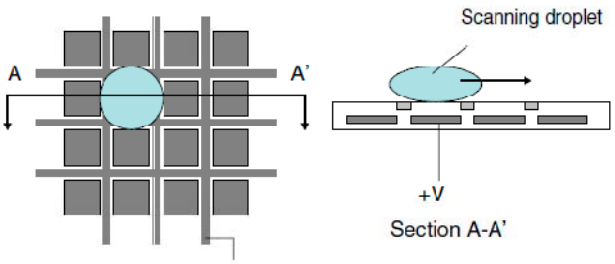

Figure 2.8 Coplanar actuation array for droplet scanning: top view (left) and side view (right). Reprinted from [34] with permission from Springer.

With such EW-based digital microfluidics setups, four different droplet operations can be realized. *Droplet transportation* is the most basic operation. A detailed review about droplet transport mechanisms using EW was reported by Mugele and Baret.[3] Successive activation of one electrode to the next will actuate the droplet transportation along the direction of the activated electrodes. *Droplet formation* is also an elementary operation of the platform. Small volumes of liquid are extracted from a reservoir by activating a series of adjacent electrodes. When the formed liquid finger overlaps the electrode on which the droplet is to be formed, all the remaining electrodes are switched off in order to form a neck in the column. The electrode underneath the reservoir is then activated to pull the liquid back, causing the neck to be broken, thus forming a droplet (see Fig. 2.9). The size of the droplet depends on the electric field strength, frequency of the applied field as well as the dimension of the channel opening. For instance, smaller droplets are generated at higher frequencies.

Droplet splitting is based on a similar strategy. As shown in Fig. 2.10a (A-C), splitting occurs when the electrodes near the opposite ends of a droplet are activated, and the central one is grounded. The activated regions will pull the droplet towards its respective ends, causing the droplet to pinch off and divide in the middle. *Droplet merging* (*i.e.* coalescence) is achieved by using three electrodes (Fig. 2.10a (D-F)). Two droplets are individually settled on two separated

electrodes. In between there is a third electrode. Activating the central electrode and deactivating its two neighbor electrodes will push the droplets together. With successive splitting and merging operations, a variety of mixing and dilution strategies can be implemented.

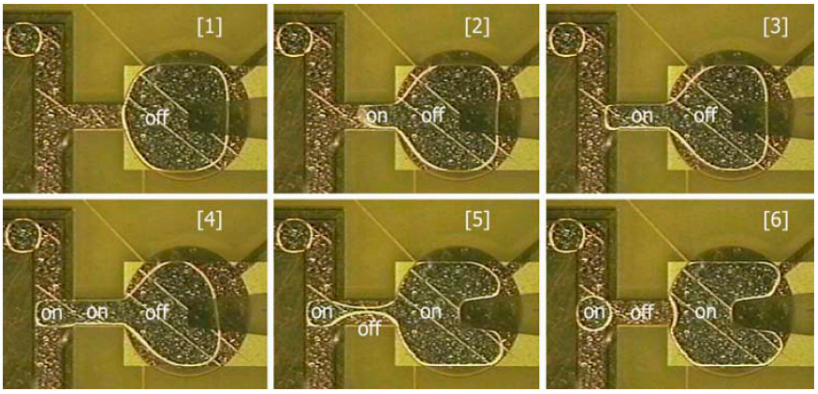

Figure 2.9 Droplet formation from an on-chip reservoir based on electrowetting forces. Reprinted from [35] with permission from the Royal Society of Chemistry (RSC).

Droplet mixing in such platform can be achieved by repetitive movement of the droplet on a rectangular path. The minimum mixing time for two 1.3 μL droplets is less than 3 s using two-dimensional arrays.[36] Paik *et al.* demonstrated that a fluorescein containing droplet could be merged with a water droplet and subsequently homogenized by transporting it back and forth over programmed adjacent electrodes. (Fig. 2.10b)

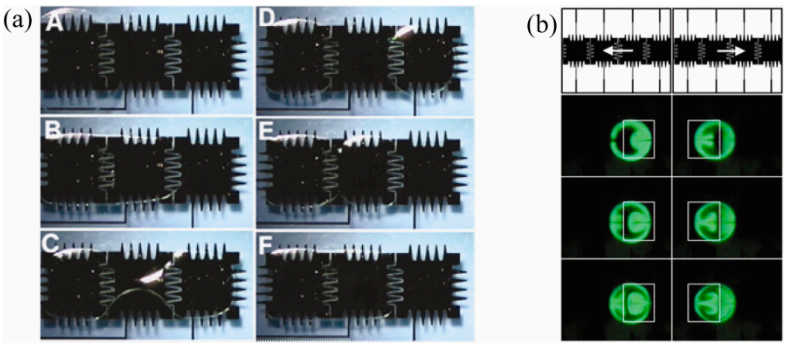

Figure 2.10 (a) Droplet splitting (A-C) and merging (D-F). (b) Mixing at 8 Hz of a coalesced droplet in a two electrode linear array. Reprinted from [27, 37] with permission from the Royal Society of Chemistry (RSC).

Realizable fluidic operations such as transportation, formation, splitting, merging and mixing have been described above. A detailed review about these basic operations and the related system integration issues was recently published by Fair[34] and Wheeler[38]. For a typical droplet volume in the microliter range, droplet motion sets in above a certain threshold voltage (typically a few tens of volts). Above that threshold, the droplet speed increases rapidly with the applied voltage, reaching values of several $cm \cdot s^{-1}$. The detailed numbers depend strongly on the insulator thickness, the quality of the surfaces and surrounding medium. Recent work aims at reducing working voltage to approximately 20 V or less, which would simplify practical applications for biotechnological applications.

2.2.7 Applications of digital microfluidics

The applications of EW-based microfluidic operations have continued to develop in the past decade, and are quite close to commercial products.[35, 39-45] One of the first applications was reported by Srinivasan *et al.* that is a colorimetric enzymatic glucose assay for clinical diagnostics (point-of-care) applications.[35] The authors illustrated the feasibility of performing bioassays on physiological fluids such as whole blood, serum, plasma and urine. The concentrations of glucoses were determined with comparable results to standard methods. The chip layout is shown in Fig. 2.11. It features high levels of integration and automation based on EW-actuated droplet manipulation: formation, transportation, splitting and mixing.

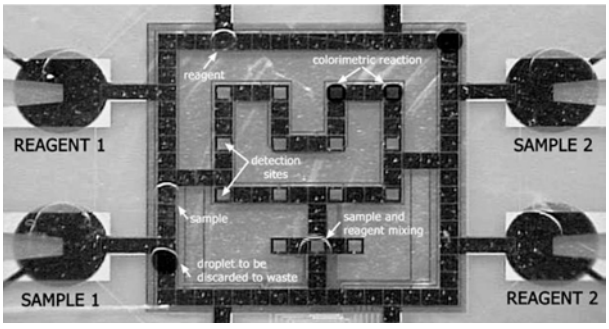

Figure 2.11 Implementation of a colorimetric glucose assay in an electrowetting-based lab-on-a-chip. Four reservoirs with injection parts are connected to an electrode circuitry, where the droplets are formed, split, mixed and transported to detection sites for readout. Reprinted from [35] with permission from Royal Society of Chemistry (RSC).

When small-volume samples are used in biochemical analysis, it is often required to isolate components that can be further processed by amplification, modified, or extracted for identification. Cho *et al*. demonstrated a microfluidic platform based on the integration of electrophoresis and EW to perform particles separation.[46] The separation procedure has three steps. First, isolation of each type of particle occurs within the droplet by applying a low-level electric field (around 3.3 V/mm). The second step is to split the droplet into two daughter droplets. The particles of each charge polarity are more concentrated in one daughter than the other. This step corresponds to the extraction of separated entities. The final step involves transporting the droplets for subsequent processing on chip (Fig. 2.12).

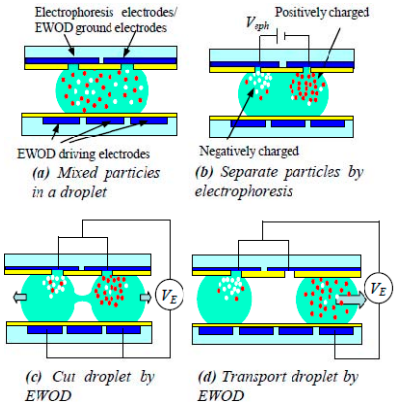

Figure 2.12 Particles separation in a droplet based on electrowetting. Reprinted from [46] with permission from IEEE.

Also the functionality of automated sample preparation of peptides and proteins for matrix-assisted laser desorption-ionization mass spectrometry (MALDI-MS) was demonstrated in an EW-based DMF.[47] In that work, standard MALDI-MS reagents, analytes, concentrations, and recipes were shown to be compatible with EW technology, and mass spectra comparable to those collected by conventional methods were obtained. Also a PCR assay has been realized on the platform by temperature cycling of a droplet at rest.[48] Additional information about the EW-based DMF platform can be found in comprehensive reviews.[34, 38]

2.3 Droplets in Two-Phase Flow Microfluidics

In the previous section, we introduced EW and EW-based DMF. In such systems, the droplets are manipulated individually as digital entities on a planar surface. However it is not the only way to manipulate droplets. In so-called TPF systems, discrete droplets are formed and transported by an immiscible continuous flow. This type of microfluidic system has seen a rapid development in the past decade, and now finds various applications in chemistry and biology.[49-54] DMF and droplet-based TPF are complementary. Generally speaking, DMF is well adapted to biodiagnostics and biorecognition. Usually this involves very small volumes of processed liquid and sophisticated operations (merging, splitting, mixing and holding) which require a lot of control. On the other hand, TPF is well suited to the treatment of small droplets at high throughput in continuous processes, like production and sorting.

In the current section, we focus on droplet-based TPF. First, we introduce the main physical parameters which can determine the flow of droplets and explain the observed behavior. Then we discuss two practical aspects in detail: (i) Droplet formation, in which the size, shape and monodispersity of the droplets is controlled using the channel geometries and flow rates. (ii) Droplet merging, including passive approaches that use the channel geometry, and active merging approaches that use electrocoalescence. Furthermore, progress in the field of micro-fabrication of the needed devices will be discussed.

2.3.1 Physical parameters

In fluid engineering, the behavior of liquids is often described in terms of dimensionless numbers which compare the importance of different physical properties. The Bond number $Bo = \Delta\rho g L^2/\sigma$, with $\Delta\rho$ the difference in mass density between the two fluids, g the gravity acceleration, L a characteristic length scale, and σ the interfacial tension[55], compares gravitational and surface forces. In microfluidics applications generally $Bo \ll 1$, which means that gravity effects can be ignored. The Reynolds number $Re = \rho v L/\mu$, where ρ is the mass density, μ the dynamic viscosity and v the mean velocity of the fluid, compares inertial forces and viscous forces. Generally, in microfluidics $Re < 1$.[56] The third quantity is the Weber number, which compares inertial forces to surface forces: $We = \rho v^2 L/\sigma$. Also

We < 1 in most applications at the microscale. From the definitions and typical magnitudes of *Re* and *We*, it follows that inertia generally becomes unimportant when the flow geometry is downscaled to dimensions in the micron range.[57] Therefore the dominant forces at the microscale are interfacial forces and viscous forces. We remark here that there are also specific scenarios in which inertial effects do play a significant role, for instance, the case for flows at very high speed, or the moment of droplet breakup.

The relative strength of these interfacial and viscous forces is represented by the (dimensionless) capillary number *Ca*, expressed by Eq. 2.6. Here μ is generally the viscosity of the most viscous fluid in the two-phase system, v is the velocity of that phase, and σ is the interfacial tension as before. Inherently, the interfacial tension tends to reduce the interfacial area, which is crucial in the formation of droplets and also for their subsequent stability. In many flow situations, viscous forces act to extend and stretch the interface.[58] At low *Ca* (< 1) the interfacial tension dominates, and spherical droplets are found. In contrast, at high *Ca* (>>1) the viscous forces play an important role, leading to deformation of the droplets and sometimes to asymmetric shapes. In some cases of high *Ca*, a completely different flow architecture, named stratified flow, can occur.[59-60] This is beyond the scope of this chapter.

$$Ca = \frac{\mu v}{\sigma} \tag{2.6}$$

2.3.2 Droplet formation

Droplet formation can be considered as the first step in the microfluidic life cycle. Many different techniques have been developed to obtain fine control over the size (distributions) and shape of droplets.[61] Those techniques for producing droplets can be either passive or active. Most of them are passive, and produce a uniform, evenly spaced continuous stream.[62] Simply said, the flow field plays a role in the deformation of the interface and promoting the growth of interfacial instabilities. Besides a continuous mechanical pressure, no external actuation or moving parts are needed. Generally the polydispersity of droplets, described as the standard deviation of the size distribution divided by the mean droplet size, can be kept as small as 1-3%.

The two most common strategies are the use of T-junction and flow focusing geometries. In general, the fluid phase to be dispersed is brought into a microchannel by a pressure-driven flow, while the flow of the second immiscible carrier liquid is driven independently. These two phases meet at a junction, where the local flow field, determined by the geometry of the junction and the flow rates of the two fluids, deforms the interface. Eventually droplets pinch off from the dispersed phase finger by a free surface instability. The pinch-off of droplets can be characterized by the competition between viscous shear stresses acting to deform the liquid interface and capillary pressure acting to resist the deformation, which is expressed by *Ca*. This number ranges between 10^{-3} and 10^{1} in most microfluidic droplet formation devices.

T-junction devices

In a typical T-junction configuration, as depicted in Fig. 2.13, the two phases flow through orthogonal channels and form droplets where they meet. This type of geometry was first demonstrated in 2001 by Thorsen *et al.*,[63] who produced monodisperse droplets with pressure controlled laminar flow in microchannels. Since then many studies were performed using T-junction geometries, to achieve a better understanding of the physical mechanism and physical parameters,[64-70] as well as to develop various applications.[71-77] The size of the droplets depends on the flow rates of the two liquids,[63] the dimensions of the channels,[64] the relative viscosity between the two phases,[78] and surfactants and their concentrations.[79]

Three main regimes can be distinguished for drop formation as the parameters are varied: dripping, squeezing and parallel flowing stream. In the dripping regime, droplet breakup occurs when the viscous shear stress overcomes the interfacial tension, analogous to the breakup of spherical droplets. If the capillary number is chosen large enough, the droplets are emitted before they can block the channel. The squeezing regime was described by Garstecki *et al.*.[64] In this regime, the capillary number is low, leading to the formation of droplets that obstruct the channel and hence restrict the continuous phase. The dramatic increase of dynamic pressure in the upstream then induces pinch-off of droplets. One theoretical study about the transition from squeezing to dripping based on the influence of *Ca* and viscosity ratio was reported by Menech *et al.*.[80]

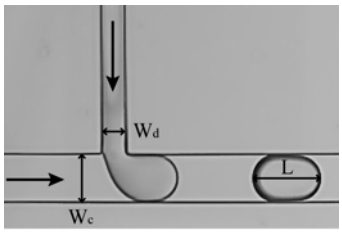

Figure 2.13 Illustration of droplet formation in a T-junction. The dispersed phase and continuous phase meet in a T-shaped junction perpendicularly.

A slightly different geometry having similar features as the above explained T junction geometry is the so-called head-on device (see Fig. 2.14a). Shui *et al.* demonstrated droplet formation in such a device, where two liquids come from opposite directions of two straight channels and form droplets upon meeting.[71, 81-82] A Y-shaped junction has also been studied by Steegmans *et al.*.[69,72] As illustrated in Fig. 2.14b, a droplet can be formed in the dripping regime in such a Y junction geometry. These authors studied the droplet formation mechanism and derived a general model predicting the droplet size. They also demonstrated that such a flat Y-junction can be used as a microfluidic tensiometer, *i.e.* a device that can measure dynamic interfacial tensions.

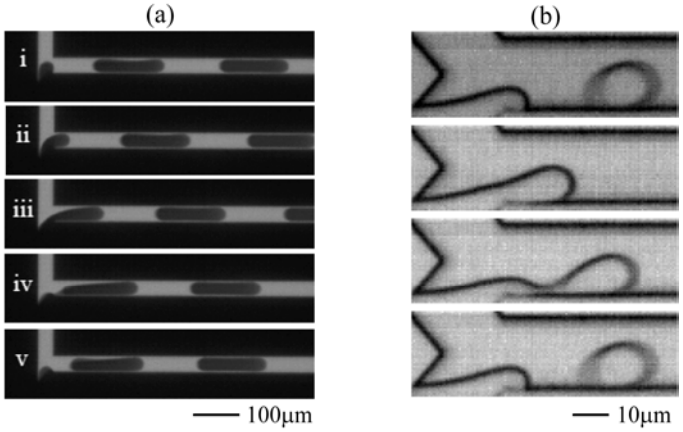

Figure 2.14 (a) Head-on device, time sequence of droplet formation in the regime of squeezing. Reprinted from [82] with permission from University of Twente. (b) Y-shaped junction, time sequence of droplet formation in the dripping regime. Reprinted from [72] with permission from the American Chemical Society (ACS).

For certain applications, a single T-junction is clearly not enough. To perform

chemical reactions or to produce droplets of alternating composition, more sophisticated designs have been realized: for example the use of double T-junctions to produce droplet pairs.[83-86] One of examples is shown in Fig. 2.15.[86] The authors of this paper demonstrated a perfect "one-to-one" droplet pair formation (self- synchronization) with the use of additional connections in the upstream and downstream channels.

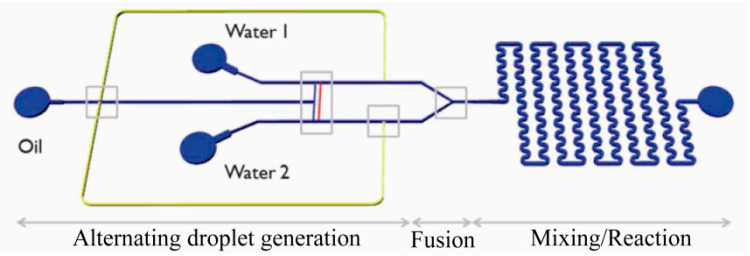

Figure 2.15 Schematic diagram of a microfluidic chip with various passive droplet manipulation capabilities. The system includes a droplet-pair generator (double T-junction), a Y-junction for droplet fusion and a winding channel for further mixing. Reprinted from [86] with permission from the Royal Society of Chemistry (RSC).

For the mass production of emulsion droplets using microfluidic devices, large scale integration of droplet generators is a necessity. For the case of T-junctions, this has been explored for up to 256 junctions in parallel.[76-77] The highest throughput was reported as 320 $mL \cdot h^{-1}$ in a 4 cm × 4 cm chip with 256 droplet formation units. Further developments along this line would be needed to achieve production at industrial scales, but the perspectives are already there. One of the challenges that may have to be faced is to minimize detrimental cross-talk between the different droplet injectors. This could occur for example if the transient pressure variation associated with the creation of a droplet would be transmitted to other droplet injectors and interfere with the droplet formation there.

Flow focusing devices

The flow focusing (FF) geometry was first proposed by Anna *et al.*[87] and Dreyfus *et al.*[88]. As demonstrated in Fig. 2.16, it consists of three inlet channels converging into a main channel *via* a narrow orifice. The dispersed phase, contained in the

middle channel, is squeezed by continuous phase flows from two opposing side channels. Both phases pass through the small orifice that is located downstream of the three channels. Finally, the stream of the dispersed phase becomes narrow and breaks into droplets. The droplet size is determined by the flow rates of the two phases and by the flow rate ratio,[89-90] in addition to the channel geometries[91] and the viscosities of the two phases.[92-93]

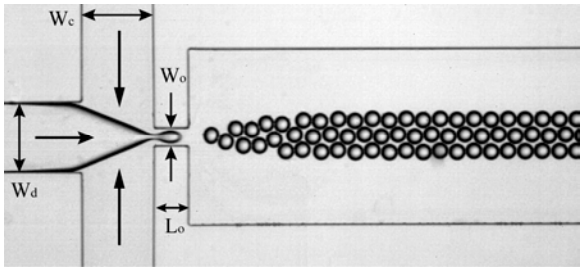

Figure 2.16 Illustration of droplet formation in flow focusing device (FFD). The widths of the inlets of dispersed phase and continuous phase, as well as the orifice are indicated as W_d, W_c and W_o. The length of orifice is indicated as L_o.

This multitude of influential parameters in principle offers a lot of control over drop formation, but it is also true that in the absence of quantitatively predicting models, each new combination of geometry, speeds and viscosities may need to be explored and tuned, in order to let the chip meet the demands (*i.e.* criteria for droplet size and formation rate). Many variations of the basic FFD geometry have recently been developed to improve the control over the size and size distribution of the droplets.[94-96] Also so-called axisymmetric flow focusing designs have been presented (Fig. 2.17). They allow the formation of monodisperse droplets with reduced size as compared to planar FFDs.[94] In these geometries, the dispersed phase is confined in the central axis of the microchannel, and pinches off by a combination of shear stresses and wetting upon contact with the inner surfaces of the channel.

Four different droplet breakup regimes have been identified in a planar FFD: squeezing, dripping, jetting and thread formation (tip-streaming), shown in Fig. 2.18. As mentioned, there are no general scaling laws that can predict the transitions between these regimes, and the same applies for the size and generation frequency of droplets. This is due to the large number of variables.

Recently, Funfschilling *et al.* concluded from velocity field measurements that the squeezing phenomenon is governed by the build-up of a pressure difference as a response to the partial and temporal blocking of the orifice by the advancing finger.[97] This mechanism is quite similar to the one that operates in a T-junction. Lee *et al.* stated that the squeezing and dripping regimes depend solely on the upstream geometry and the related flow field while the thread formation mode depends solely on the downstream channel and its associated flow field.[91] It is clear that unraveling the mechanism of droplet break-up in FFDs still needs further investigation.

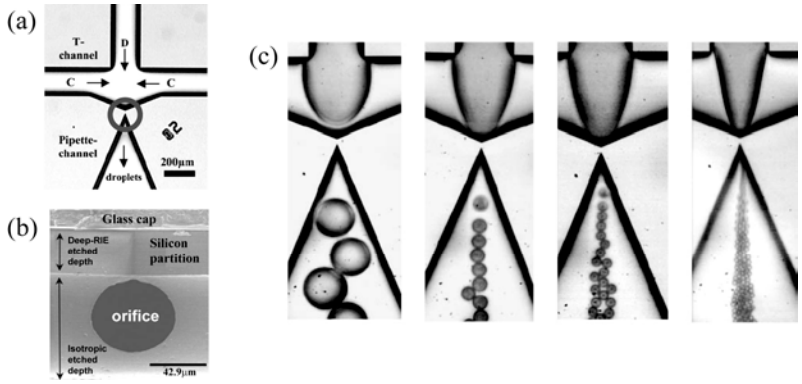

Figure 2.17 Axisymmetric flow focusing design: (a) Planar view; (b) SEM image of the circular orifice; (c) Water droplets formation at increasing oil flow rates and fixed water flow rate. Reprinted from [96] with permission from Royal Society of Chemistry (RSC).

To increase the flexibility of FFDs, also additional (active) elements have been incorporated into devices. Electrical means have been applied to obtain more control over droplet formation in FFDs.[98-101] Using such electric control, the size range in which droplets can be produced could be extended, and the generation frequency could be raised to very high values. Gu *et al.* integrated electrowetting into FFDs and demonstrated three different droplet break-up regimes: dripping, tip-streaming and conical spray.[99-100] The conical spray was found at high W/O flow rate ratios and electrowetting numbers $\eta > 1$ (which were reached at voltages of O(50 V)). This represents a specific regime of electrowetting. Similar droplet spray patterns were observed by Kim *et al.*[98] and He *et al.*[101] who integrated an electrospray functionality into FFDs. In such devices, shown in Fig. 2.19a, the droplet size can also be diminished by increasing the voltage. Yet for the

formation of very fine droplets, one needs to be in the Taylor cone regime, which requires voltages above ≈ 1500V.

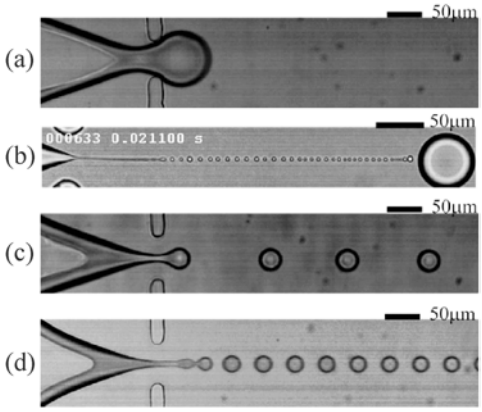

Figure 2.18 Different droplet breakup processes: (a) Squeezing, (b) Tip-streaming, (c) Dripping, and (d) Jetting. Reprinted from [91] with permission from the American Institute of Physics (AIP).

Also membrane valves have been introduced into FFDs to vary the width of the orifice.[102-105] Abate *et al.* demonstrated that the droplet size and formation frequency in the dripping regime can be controlled by such an adaptable orifice (Fig. 2.19b).[105] Other approaches based on (local) adjustment of the temperature have been reported: here use is made of the temperature dependence of the viscosity and interfacial tension.[106-108] This method allowed to control the droplet size and generation frequency independently.

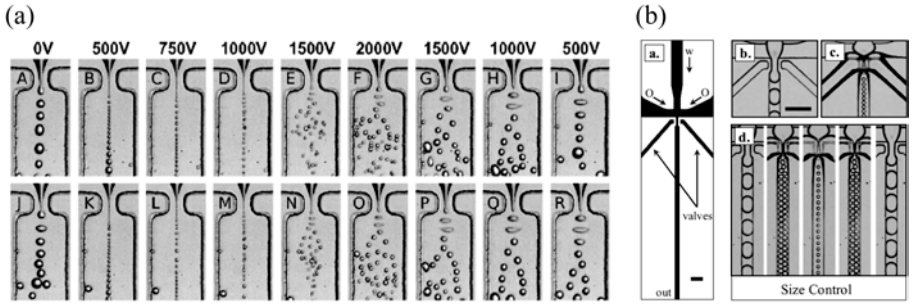

Figure 2.19 (a) Droplet formation in FFD using electrospray; (b) Droplet size control under actuation of the width of orifice. Reprinted from [101, 105] with permission from the American Institute of Physics (AIP).

To increase the droplet production rate, multiple FFDs could be used in parallel

in either linear[109-110] or circular circuits[76]. Li *et al*. demonstrated a quadruple droplet generator with a weak parametric coupling between the different parallel FFDs. By choosing different geometries for the individual FFDs, these authors were able to simultaneously produce several populations of droplets with distinct sizes, where each of the populations had a narrow size distribution (Fig. 2.20). Also Hashimoto *et al.*[110] studied the dynamic mechanism of droplet formation in parallel FFDs. They found a weak hydrodynamic coupling as well.

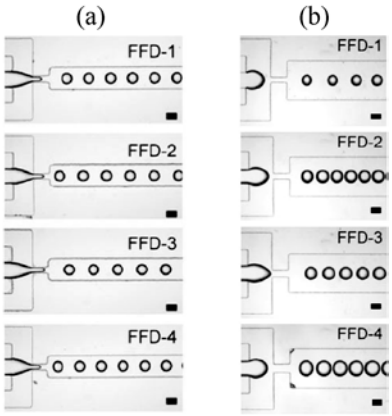

Figure 2.20 Illustration of quadruple droplet generator: (a) Same dimensions of the orifices from FFD-1 to FFD-4; (b) FFDs with different widths of the orifices. Reprinted from [109] with permission from Royal Society of Chemistry (RSC).

Droplet-on-demand

In a large majority of the existing continuous flow devices, droplets are produced incessantly; the flow can be switched on and off by mechanical or electrical means, and the conditions of droplet generation can be modified, but the droplets will always appear in trains. In cases where this scenario is undesirable, and droplets need to become available one-by-one upon request, DMF applications may come to mind first. However, also continuous flow systems can be adapted to deliver droplets on demand. Surprisingly, this possibility has hardly been explored, in spite of its potential for use in high throughput screening (HTS) in microtiter technology or in the programmed coalescence of droplets after synchronized formation of droplet pairs. Especially the combination of on demand formation of droplets and a subsequent processing at high speed makes it interesting.

One of the possibilities for on-demand droplet formation is the use of integrated microvalves.[111-113] For instance, Zeng *et al.* incorporated a pneumatic microvalve fabricated in polydimethylosiloxane (PDMS) into microfluidic devices (Fig. 2.21a). By intermittently switching the valve on/off, individual droplets can be produced on-demand.[113] Also piezoelectric actuators have been used for on-demand droplet formation.[114-115] In such systems the droplet size and frequency can be set with high accuracy through conversion of voltage supplied to the piezoelectric actuator into a mechanical displacement. Churski *et al.* reported a droplet-on-demand system that used external electromagnetic valves interconnected with the chip for scanning of reaction conditions.[116] Alternatively, also electric fields can be used to produce droplets on-demand. Malloggi *et al.*[117-118] used electrowetting as an active control mechanism to increase the wettability of the channel wall at the location of droplet formation. Combining pressure control over the two phases and electrical control over wetting, the size and/or generation rate of their droplets could be tuned within a certain range (Fig. 2.21b).

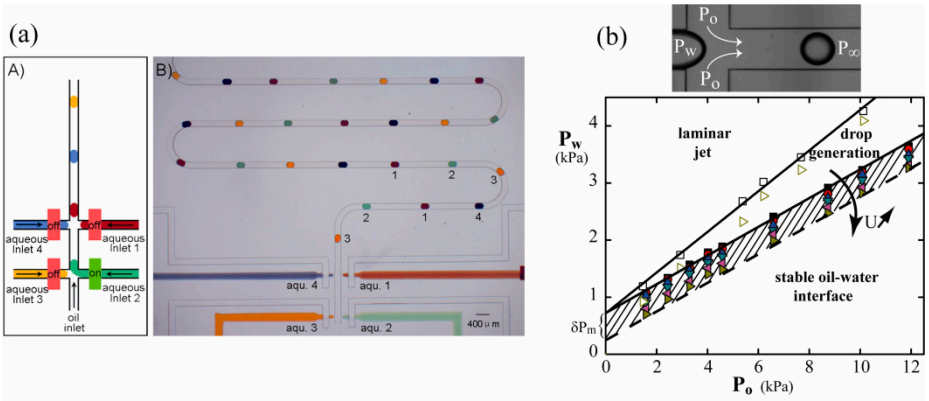

Figure 2.21 (a) On-demand formation of arrays of droplets with distinct composition by sequentially switching on/off microvalves. Reprinted from [113] with permission from Royal Society of Chemistry (RSC); (b) Phase diagram identifying electro- wetting induced droplet formation. Hatched area: EW tuning window for on-demand droplet formation. Reprinted from [117] with permission from IOP publishing.

2.3.3 Droplet merging

Droplets can be used as independent microreactors for a number of chemical and biological applications, *e.g.* chemical synthesis, kinetics studies, screening of

biological contents and biomedical diagnostics. Merging droplets is an essential approach to perform reactions within droplets. In practice, the prerequisites for merging are that the droplets (i) touch each other and (ii) overcome the stabilizing forces caused by surface tension and lubrication. Several designs have been used to bring droplets together.[119-127] To subsequently overcome the stabilizing forces, both the viscosity ratio of two-phase fluids,[74] and the presence of surfactant at the interface[128-130] have to be considered.

Surfactants are used to stabilize droplets in two-phase flow against coalescence. These molecules generally consist of a compact polar head and a long-chain hydrophobic tail. Surfactants reduce the interfacial tension between two liquids by adsorbing at the liquid-liquid interface where they often align perpendicular to the surface. Stabilization of droplets can be realized in different ways: (i) via repulsion between the interfaces due to electrostatic and/or steric effects; (ii) by slowing down the hydrodynamic flow along the interface via Marangoni effects or via enhanced surface viscosity.[131-132]

Basically, there are two main approaches, namely passive merging and active merging, to coalesce droplets. In the case of passive merging, droplets are normally not stabilized by surfactant. Then coalescence occurs spontaneously when the droplets meet; the occurrence of which can be organized with a suitably shaped channel geometry.[120] For droplets that are stabilized by surfactants, active merging is required. For this purpose, thermocapillary effect[106, 133] or electro-coalescence[134-139] can be used.

Passive merging

In passive droplet merging, the design of the channel geometry is a key to achieve proper merging, since droplet synchronization is required and active means to compensate for any synchronization errors are missing. In principle merging can occur simply at a channel junction, if the generation and transport of each pair of droplets is such that both drops arrive there at the same time. However in practice this can be difficult to achieve, and therefore special designs of geometries are often used.

A widely used geometry for droplet merging consists of a widening channel

follow by a narrower channel (Fig. 2.22).[119-122] In this geometry the droplet velocity decreases in the widening channel because of drainage of the continuous phase, after which it increases again upon entry in the narrow channel. Due to this changing flow field, two subsequent droplets are allowed to come close together and let the liquid that separates them drain away. Bremond *et al.* observed that the merging does not occur during the first encounter when two droplets enter the extended channel, but rather during the separation stage of two droplets when the first droplet begins to enter the narrow channel (Fig. 2.22c).[122] The separation induces the formation of two facing protrusions (Fig. 2.22d) which then bring the two interfaces close enough until they merge. Later Lai *et al.* reported a theoretical study based on this observation.[140] The created protrusions lead to a rapid increase of the surface area locally, and thus to destabilize the interface at certain locations. The conditions under which droplet merging occurs, can be predicted on the basis of their model. Alternatively in other channel geometries, droplets are merged by slowing down or stopping the leading droplet at a simple geometrical constriction,[126-127] or in a channel with an array of pillar elements.[123-124]

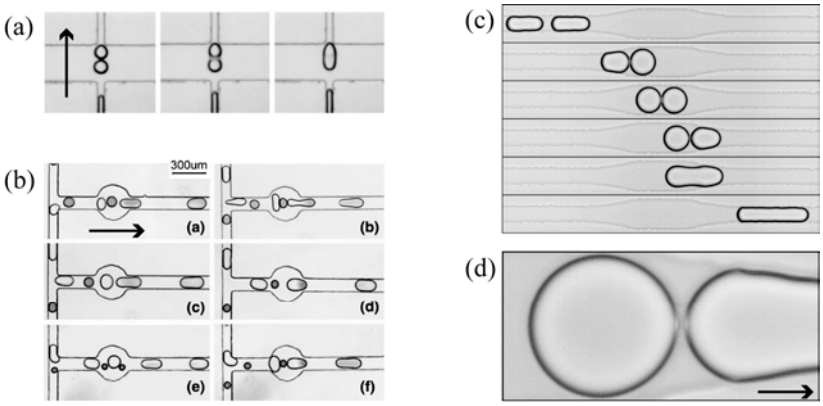

Figure 2.22 Passive droplet merging based on channel geometries. (a) and (b) give two examples to perform merging of two or more droplets. Reprinted from [120-121] with permission from Springer. (c) and (d) demonstrate last moment of droplet merging, called decompression merging. Reprinted from [122] with permission from the American Physical Society (APS). Note: the arrows indicate the traveling direction of the droplets.

It should be noted that typically no surfactant is used in these passive merging experiments. However, the absence of surfactant has its drawbacks: unintended

merging events can occur, and also the possibilities for further manipulation of the droplets after the merging can be limited. By exception, also a case of passive merging of surfactant-covered droplets has been reported. Mazutis *et al.* demonstrated a channel design for merging bidispersed droplets which were formed in the presence of surfactant and which had significant asymmetry in droplet size.[129] However undesired coalescence still occurred often. In many cases it is therefore preferred to use surfactant stabilized droplets, and achieve merging with the help of external forces.

Active merging

To achieve active and selective droplet merging, the most widely utilized method is to apply an electric field at the location where two droplets meet. Link *et al.* reported that droplets can be merged by applying voltages with opposite sign across the two droplets during their formation.[102] Chabert *et al.* performed merging of individual droplet pairs using electrocoalescence (EC).[141] The mechanistic aspects of EC are not yet fully understood, and are still under debate.[134,138,142-143] A complete description of EC is beyond the scope of this chapter. Fig. 2.23 depicts a general schematic of one pair of droplets in an electric field. Two droplets approach to each other and deform from a sphere to prolate spheroid induced by electrical (Maxwell) stress σ_E. This stress will balance with interface tension and viscous stresses.[144] In the case of Newtonian fluid behavior, neglected gravitational influences and low Reynolds numbers ($Re < 1$, reasonable in microfluidics), we can obtain:

$$\mu\nabla^2 U - \nabla P = \nabla \cdot T \tag{2.7}$$

Where the viscosity μ, the velocity U, pressure P and stress fields T in each Newtonian fluid phase of a two-phase system. The velocity is continuous across the interface, thus the total stress difference (electric plus viscous) between inside & outside the droplet is balanced by the interfacial tension:

$$n \cdot T = n \cdot T^N + n \cdot T^E = \sigma n \nabla_S \cdot n \tag{2.8}$$

Where n is the unit normal vector at the interface, σ is the interfacial tension, $\nabla_S \cdot n$ is the mean curvature of the interface, T^E is the Maxwell stress tensor

(proportional to the square of the applied electric field) and T^N is the tensor of viscous forces.[144]

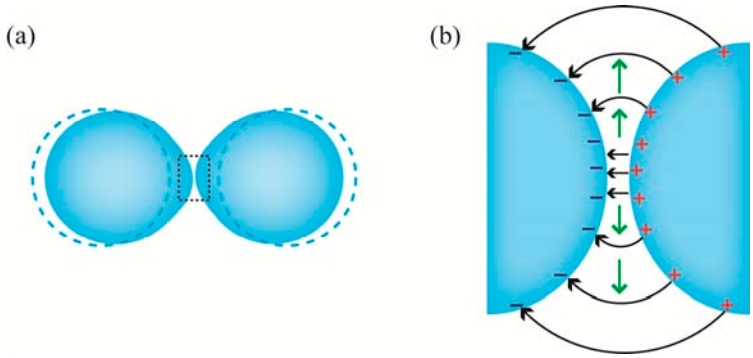

Figure 2.23 Schematic of two approaching liquid droplets in an electric field. (a) Droplets deformed from a sphere to a prolate spheroid induced by electrical stress; (b) The zoom-in edge of two droplets with opposite charges. The black arrows indicate the electric field. The green arrows indicate the squeezing of ambient oil.

Priest *et al.* argued that EC can cause an electric-field-induced dynamic instability of the oil/water interface, subsequently leading to the formation of a liquid bridge and coalescence (Fig. 2.24a).[134] Thiam *et al.* demonstrated the merging of separated droplet pairs and also explained their observations in terms of a competition between electrical stress and restoring capillary pressure. Also the importance of the separation distance between the two droplets in the electric field was highlighted (Fig. 2.24b).[138] Qualitatively speaking, it is clear that the electric field near the surface of droplets can be amplified by dipole-dipole interactions between the droplets, and hence become stronger as droplets approach each other more closely. It is conceivable that this will lead to destabilization of the surfaces.[145] Furthermore, also the surfactant molecules can be involved. In the case of surfactants with dipolar head-groups, a redistribution or re-alignment along the electric field lines can take place. Also this can destabilize the interface and lead to coalescence.[146]

One of the first applications of EC in two-phase flow microfluidics was presented by Tan *et al*.[147] Two droplets containing biological molecules were brought into an expanded channel and merged there due to an electric field generated by an embedded electrode. Later, several variations based on this geometry were

adopted to implement EC in microfluidic chips.[102,138,141] For each of these EC-based systems, droplet synchronization and precise electrode alignment are required.

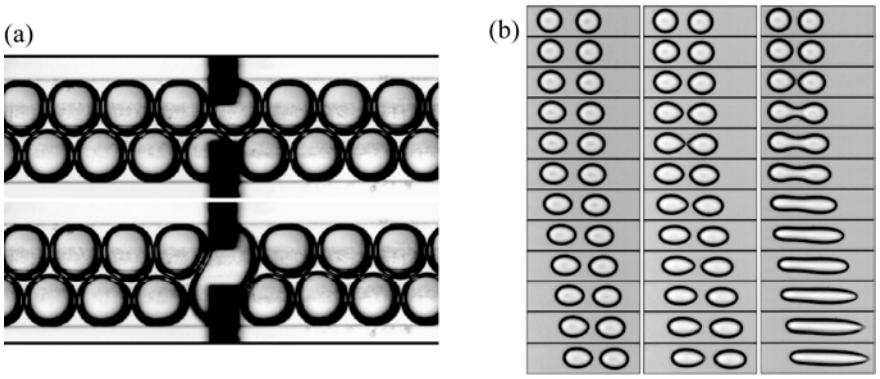

Figure 2.24 (a) Targeted EC of droplet pairs (electrodes are visible as shown black rectangles). Reprinted from [134] with permission from the American Institute of Physics (AIP). (b) Time sequences showing three different regimes: stable, partial merging and coalescence. The initial separation of two droplets is a key parameter. Reprinted from [138] with permission from the American Physical Society (APS).

To overcome these limitations, Zagnoni *et al.* designed an electrode pattern, where a single droplet is held until the second one arrives (Fig. 2.25a).[136] After coalescence, the merged droplet is automatically released due to an increased hydrodynamic force (now exceeding the electrostatic holding force). As illustrated in Fig. 2.25b, Niu *et al.* depicted an alternative method,[139] by combining a passive merging approach (a pillar array in the channel) with an active merging approach (built-in electrodes). In this scheme, the pillar array slows down and traps the droplet during the drainage of the oil phase. EC then occurs when droplets have reached close proximity.

Also double T-junction geometry with embedded electrodes has been reported in the context of active merging. In the system of Wang *et al.*, two series of droplets can be produced and merged at same time.[137] Yet another method for the active merging of droplets is dielectrophoresis (DEP). A drawback of this method is that it requires rather high voltages, up to several kV.[148-150]

Finally, also thermocapillary effects can be cited as a mechanism to perform active merging of droplets.[106, 133, 151-152] Heating two adjacent droplets with a focused laser

beam was reported to cause convective motions in the droplets, as well as depletion of surfactant molecules from the interface. Also this turned out to be effective for droplet merging.

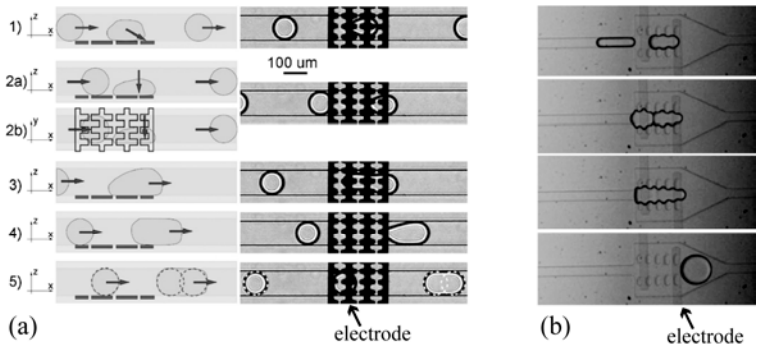

Figure 2.25 (a) droplet merging on squared-patterned electrodes. Reprinted from [136] with permission from Royal Society of Chemistry (RSC). (b) Droplet are stopped by pillar array and merged by EC. Reprinted from [139] with permission from American Chemical Society (ACS).

2.3.4 Microchannel fabrication

Microfabrication methods, which include film deposition, photolithography, isotropic or anisotropic etching steps and anionic bonding of a microchip, were first achieved with silicon (Si).[153] Thereafter, glass was used as a substrate while relying on similar fabrication procedures.[154] Nowadays, the most commonly used microfluidic chips are made of polymers, in particular polydimethylsiloxane (PDMS) due to its low expense and rapid prototyping.[155] The procedure for fabricating such microchips is based on soft lithography, involving photo-lithography steps for producing a mold, followed by casting of PDMS replicas from this mold, then bonding the PDMS slab to a glass slide to seal the micro-channels.[155-156] Whereas initially, molds were made from Si, later the "negative photoresist" SU-8 became more popular due to simplicity of production. SU-8 in fact stands for a series of commercial resists, each having a different viscosity. This allows to achieve a wide range of construction heights, from a few microns to several hundred microns in one step (more details in ref.157).

In the case of droplet formation in a microchip, controlling the wetting properties of the channel walls is essential. For instance, producing water droplets in oil

phase requires hydrophobic channels, whereas producing oil droplets in water phase needs hydrophilic channels. Some strategies can be used to alter the wettability of the channel walls with regard to the required droplet formation. For glass or Si-based microchips, treatments such as silanization and siliconization, can be implemented to modify the hydrophilic surface into hydrophobic.[82, 158-159] Oxygen plasma treatment can alter the naturally hydrophobic PDMS surface into hydrophilic temporarily.[155] If this is not sufficient to achieve the desired wetting properties, a permanent surface modification, such as acrylic acid polymer grafting[160] or sol-gel coating[161], can be used to make PDMS surface hydrophilic. Another motivation for surface modification of PDMS lies in its poor chemical compatibility, causing swelling and deformation in the presence of strong organic solvents. The polymer grafting, such as acrylic acid and poly(ethylene glycol) (PEG), are widely used to counteract this effect.[160,162]

Achieving a reliable surface modification of PDMS is still a challenging task. An interesting alternative class of polymers is fluoropolymer, which exhibit excellent chemical compatibility, in addition to similar properties of PDMS (transparency, flexibility and conformability).[163-164] However, the bonding of fluoropolymer and substrate is quite weak, which limits applications under high working pressures. Also this kind of devices cannot be used at high temperature.[165]

Another issue of PDMS is its low elastic modulus, which limits the production of microchannels with low aspect ratio or very small dimensions. Currently there is much attention on developing a rapid prototyping technique using ultraviolet (UV) curable polymers.[100,166-171] Bartolo *et al.* demonstrated the fabrication process based on the UV curable material of Norland Optical Adhesive (NOA). In general there are two steps: (i) producing a PDMS mold from a SU8 master. (ii) making a thiolene based NOA replica from the PDMS mold via soft imprint lithography. Such NOA-based microchips exhibit greater chemical compatibility and higher elastic modulus than PDMS. Thus NOA-based microchips can be used in various organic solvent environments. It is possible to fabricate the channel with sub-micron structure or low aspect ratio.

Hot embossing technique is an alternative soft lithographic method for fabrication of microchips using thermoplastic polymers. The number of available ther-

moplastic materials has strongly increased in the last few years.[172-175] Tsao *et al.* reviewed the bonding of thermoplastic polymer to substrates.[176] Moreover, This class of polymers is suitable for device fabrication on a large scale.

2.4 Conclusions

DMF using EW has shown a strong development in the past decade. It is now recognized as one of the most flexible and reliable methods to modulate surface tension and hence manipulate liquid droplets, in spite of some limitations like contact angle saturation and hysteresis. TPF with droplets has seen considerable progress in the past decade. The formation and merging of droplets, being the two key steps of many operations, have been optimized for a large variety of applications, ranging from emulsification at controlled droplet size to the use of droplets as microreactors. Besides purely hydrodynamic manipulation also electric signals transmitted via microelectrodes are increasingly used to enhance control. With the latter, the formation and merging of droplets can be achieved on-demand and with high precision.

References

1. G. Lippmann, *Ann Chim Phys*, 1875, **5**, 494.
2. B. Berge, *C. R. Acad. Sci.*, 1993, **II 317**, 157.
3. F. Mugele and J. C. Baret, *J Phys-Condens Mat*, 2005, **17**, R705-R774.
4. F. Mugele, A. Klingner, J. Buehrle, D. Steinhauser and S. Herminghaus, *J Phys-Condens Mat*, 2005, **17**, S559-S576.
5. J. C. Baret and F. Mugele, *Phys Rev Lett*, 2006, **96**, 016106.
6. D. Steinhauser, Diplomarbeit, University of Ulm, 2004.
7. H. J. J. Verheijen and M. W. J. Prins, *Langmuir*, 1999, **15**, 6616-6620.
8. B. Janocha, H. Bauser, C. Oehr, H. Brunner and W. Gopel, *Langmuir*, 2000, **16**, 3349-3354.
9. A. G. Papathanasiou and A. G. Boudouvis, *Appl Phys Lett*, 2005, **86**, 164102.
10. A. G. Papathanasiou, A. T. Papaioannou and A. G. Boudouvis, *J Appl Phys*, 2008, **103**, 034901.
11. A. I. Drygiannakis, A. G. Papathanasiou and A. G. Boudouvis, *Langmuir*, 2009, **25**, 147-152.
12. M. Vallet, M. Vallade and B. Berge, *Eur Phys J B*, 1999, **11**, 583-591.
13. F. Mugele and S. Herminghaus, *Appl Phys Lett*, 2002, **81**, 2303-2305.
14. F. Li and F. Mugele, *Appl Phys Lett*, 2008, **92**, 244108.
15. M. Maillard, J. Legrand and B. Berge, *Langmuir*, 2009, **25**, 6162-6167.
16. M. Paneru, C. Priest, R. Sedev and J. Ralston, *J Am Chem Soc*, 2010, **132**, 8301-8308.

17. C. Quilliet and B. Berge, *Europhys Lett*, 2002, **60**, 99-105.
18. J. S. Kuo, P. Spicar-Mihalic, I. Rodriguez and D. T. Chiu, *Langmuir*, 2003, **19**, 250-255.
19. M. Bienia, F. Mugele, C. Quilliet and P. Ballet, *Physica A*, 2004, **339**, 72-79.
20. A. Staicu and F. Mugele, *Phys Rev Lett*, 2006, **97**, 167801.
21. F. P. Bretherton, *J Fluid Mech*, 1961, **10**, 166-188.
22. M. G. Pollack, R. B. Fair and A. D. Shenderov, *Appl Phys Lett*, 2000, **77**, 1725-1726.
23. M. Abdelgawad and A. R. Wheeler, *Adv Mater*, 2009, **21**, 920-925.
24. A. R. Wheeler, *Science*, 2008, **322**, 539-540.
25. E. Seyrat and R. A. Hayes, *J Appl Phys*, 2001, **90**, 1383-1386.
26. H. Moon, A. R. Wheeler, R. L. Garrell, J. A. Loo and C. J. Kim, *Lab Chip*, 2006, **6**, 1213-1219.
27. M. G. Pollack, A. D. Shenderov and R. B. Fair, *Lab Chip*, 2002, **2**, 96-101.
28. A. G. Banpurkar, K. P. Nichols and F. Mugele, *Langmuir*, 2008, **24**, 10549-10551.
29. M. Gong and C. Kim, *18th IEEE international conference on micro electro mechanical systems*, 2005, 726-729.
30. V. Pamula, M. Pollack, P. Paik, H. Ren and R. Fair, *US Pat.*, 6,911,132, 2005.
31. C. G. Cooney, C. Y. Chen, M. R. Emerling, A. Nadim and J. D. Sterling, *Microfluid Nanofluid*, 2006, **2**, 435-446.
32. U. C. Yi and C. J. Kim, *J Micromech Microeng*, 2006, **16**, 2053-2059.
33. R. B. Fair, A. Khlystov, T. D. Tailor, V. Ivanov, R. D. Evans, P. B. Griffin, V. Srinivasan, V. K. Pamula, M. G. Pollack and J. Zhou, *Ieee Des Test Comput*, 2007, **24**, 10-24.
34. R. B. Fair, *Microfluid Nanofluid*, 2007, **3**, 245-281.
35. V. Srinivasan, V. K. Pamula and R. B. Fair, *Lab Chip*, 2004, **4**, 310-315.
36. P. Paik, V. K. Pamula and R. B. Fair, *Lab Chip*, 2003, **3**, 253-259.
37. P. Paik, V. K. Pamula, M. G. Pollack and R. B. Fair, *Lab Chip*, 2003, **3**, 28-33.
38. M. Jebrail and A. Wheeler, *Curr Opin Chem Biol*, 2010, **14**, 574-581.
39. E. M. Miller and A. R. Wheeler, *Anal Chem*, 2008, **80**, 1614-1619.
40. L. Malic, T. Veres and M. Tabrizian, *Biosens Bioelectron*, 2009, **24**, 2218-2224.
41. M. J. Jebrail and A. R. Wheeler, *Anal Chem*, 2009, **81**, 330-335.
42. I. Barbulovic-Nad, S. H. Au and A. R. Wheeler, *Lab Chip*, 2010, **10**, 1536-1542.
43. N. A. Mousa, M. J. Jebrail, H. Yang, M. Abdelgawad, P. Metalnikov, J. Chen, A. R. Wheeler and R. F. Casper, *Sci Transl Med*, 2009, **1**, 1ra2.
44. V. N. Luk and A. R. Wheeler, *Anal Chem*, 2009, **81**, 4524-4530.
45. D. Chatterjee, A. J. Ytterberg, S. U. Son, J. A. Loo and R. L. Garrell, *Anal Chem*, 2010, **82**, 2095-2101.
46. S.-K. Cho and C.-J. Kim, *Proc. IEEE Micro Electro Mech Syst (MEMS)*, 2003, 686-689.
47. A. R. Wheeler, H. Moon, C. J. Kim, J. A. Loo and R. L. Garrell, *Anal Chem*, 2004, **76**, 4833-4838.
48. Y. H. Chang, G. B. Lee, F. C. Huang, Y. Y. Chen and J. L. Lin, *Biomed Microdevices*, 2006, **8**, 215-225.
49. B. Zheng, L. S. Roach and R. F. Ismagilov, *J Am Chem Soc*, 2003, **125**, 11170-11171.
50. H. J. Oh, S. H. Kim, J. Y. Baek, G. H. Seong and S. H. Lee, *J Micromech Microeng*, 2006, **16**, 285-291.

51. Y. J. Song, J. Hormes and C. S. S. R. Kumar, *Small*, 2008, **4**, 698-711.
52. N. R. Beer, E. K. Wheeler, L. Lee-Houghton, N. Watkins, S. Nasarabadi, N. Hebert, P. Leung, D. W. Arnold, C. G. Bailey and B. W. Colston, *Anal Chem*, 2008, **80**, 1854-1858.
53. A. B. Theberge, F. Courtois, Y. Schaerli, M. Fischlechner, C. Abell, F. Hollfelder and W. T. S. Huck, *Angew Chem Int Edit*, 2010, **49**, 5846-5868.
54. D. T. Chiu, R. M. Lorenz and G. D. M. Jeffries, *Anal Chem*, 2009, **81**, 5111-5118.
55. L. Shui, J. C. T. Eijkel and A. van den Berg, *Adv Colloid Interfac*, 2007, **133**, 35-49.
56. T. M. Squires and S. R. Quake, *Rev Mod Phys*, 2005, **77**, 977-1026.
57. C. N. Baroud, F. Gallaire and R. Dangla, *Lab Chip*, 2010, **10**, 2032-2045.
58. H. A. Stone, *Annu Rev Fluid Mech*, 1994, **26**, 65-102.
59. S. T. Thoroddsen and Y. K. Tan, *Phys Fluids*, 2004, **16**, 13-16.
60. A. Serizawa, Z. P. Feng and Z. Kawara, *Exp Therm Fluid Sci*, 2002, **26**, 703-714.
61. H. Song, D. L. Chen and R. F. Ismagilov, *Angew Chem Int Edit*, 2006, **45**, 7336-7356.
62. G. F. Christopher and S. L. Anna, *J Phys D Appl Phys*, 2007, **40**, R319-R336.
63. T. Thorsen, R. W. Roberts, F. H. Arnold and S. R. Quake, *Phys Rev Lett*, 2001, **86**, 4163-4166.
64. P. Garstecki, M. J. Fuerstman, H. A. Stone and G. M. Whitesides, *Lab Chip*, 2006, **6**, 693-693.
65. G. F. Christopher, N. N. Noharuddin, J. A. Taylor and S. L. Anna, *Phys Rev E*, 2008, **78**, 036317.
66. M. C. Jullien, M. J. T. M. Ching, C. Cohen, L. Menetrier and P. Tabeling, *Phys Fluids*, 2009, **21**, 072001.
67. K. Wang, Y. C. Lu, J. Tan, B. D. Yang and G. S. Luo, *Microfluid Nanofluid*, 2010, **8**, 813-821.
68. A. R. Abate, A. Poitzsch, Y. Hwang, J. Lee, J. Czerwinska and D. A. Weitz, *Phys Rev E*, 2009, **80**, 026310.
69. M. L. J. Steegmans, K. G. P. H. Schroen and R. M. Boom, *Langmuir*, 2009, **25**, 3396-3401.
70. D. Malsch, N. Gleichmann, M. Kielpinski, G. Mayer, T. Henkel, D. Mueller, V. van Steijn, C. R. Kleijn and M. T. Kreutzer, *Microfluid Nanofluid*, 2010, **8**, 497-507.
71. L. L. Shui, A. van den Berg and J. C. T. Eijkel, *Lab Chip*, 2009, **9**, 795-801.
72. M. L. J. Steegmans, A. Warmerdam, K. G. P. H. Schroen and R. M. Boom, *Langmuir*, 2009, **25**, 9751-9758.
73. H. Song, J. D. Tice and R. F. Ismagilov, *Angew Chem Int Edit*, 2003, **42**, 768-772.
74. B. Zheng, J. D. Tice and R. F. Ismagilov, *Anal Chem*, 2004, **76**, 4977-4982.
75. K. L. Wang, T. B. Jones and A. Raisanen, *Lab Chip*, 2009, **9**, 901-909.
76. T. Nisisako and T. Torii, *Lab Chip*, 2008, **8**, 287-293.
77. Y. Zeng, R. Novak, J. Shuga, M. T. Smith and R. A. Mathies, *Anal Chem*, 2010, **82**, 3183-3190.
78. J. D. Tice, A. D. Lyon and R. F. Ismagilov, *Anal Chim Acta*, 2004, **507**, 73-77.
79. J. C. Baret, F. Kleinschmidt, A. El Harrak and A. D. Griffiths, *Langmuir*, 2009, **25**, 6088-6093.
80. M. De Menech, P. Garstecki, F. Jousse and H. A. Stone, *J Fluid Mech*, 2008, **595**, 141-161.

81. L. L. Shui, F. Mugele, A. van den Berg and J. C. T. Eijkel, *Appl Phys Lett*, 2008, **93**, 153113.
82. L. Shui, University of Twente, 2009.
83. L. H. Hung, K. M. Choi, W. Y. Tseng, Y. C. Tan, K. J. Shea and A. P. Lee, *Lab Chip*, 2006, **6**, 174-178.
84. V. Barbier, H. Willaime, P. Tabeling and F. Jousse, *Phys Rev E*, 2006, **74**, 046306.
85. L. Frenz, J. Blouwolff, A. D. Griffiths and J. C. Baret, *Langmuir*, 2008, **24**, 12073-12076.
86. J. Hong, M. Choi, J. B. Edel and A. J. deMello, *Lab Chip*, 2010, **10**, 2702-2709.
87. S. L. Anna, N. Bontoux and H. A. Stone, *Appl Phys Lett*, 2003, **82**, 364-366.
88. R. Dreyfus, P. Tabeling and H. Willaime, *Phys Rev Lett*, 2003, **90**, 144505.
89. T. Ward, M. Faivre, M. Abkarian and H. A. Stone, *Electrophoresis*, 2005, **26**, 3716-3724.
90. J. Collins and A. P. Lee, *Microfluid Nanofluid*, 2007, **3**, 19-25.
91. W. Lee, L. M. Walker and S. L. Anna, *Phys Fluids*, 2009, **21**, 032103.
92. T. Cubaud and T. G. Mason, *Phys Fluids*, 2008, **20**, 053302.
93. Z. H. Nie, M. S. Seo, S. Q. Xu, P. C. Lewis, M. Mok, E. Kumacheva, G. M. Whitesides, P. Garstecki and H. A. Stone, *Microfluid Nanofluid*, 2008, **5**, 585-594.
94. S. Takeuchi, P. Garstecki, D. B. Weibel and G. M. Whitesides, *Adv Mater*, 2005, **17**, 1067-1072.
95. S. H. Huang, W. H. Tan, F. G. Tseng and S. Takeuchi, *J Micromech Microeng*, 2006, **16**, 2336-2344.
96. L. Yobas, S. Martens, W. L. Ong and N. Ranganathan, *Lab Chip*, 2006, **6**, 1073-1079.
97. D. Funfschilling, H. Debas, H. Z. Li and T. G. Mason, *Phys Rev E*, 2009, **80**, 015301.
98. H. Kim, D. W. Luo, D. Link, D. A. Weitz, M. Marquez and Z. D. Cheng, *Appl Phys Lett*, 2007, **91**, 133106.
99. H. Gu, F. Malloggi, S. A. Vanapalli and F. Mugele, *Appl Phys Lett*, 2008, **93**, 183507.
100. H. Gu, M. H. G. Duits and F. Mugele, *Lab Chip*, 2010, **10**, 1550-1556.
101. P. He, H. Kim, D. W. Luo, M. Marquez and Z. D. Cheng, *Appl Phys Lett*, 2010, **96**, 174103.
102. D. R. Link, E. Grasland-Mongrain, A. Duri, F. Sarrazin, Z. D. Cheng, G. Cristobal, M. Marquez and D. A. Weitz, *Angew Chem Int Edit*, 2006, **45**, 2556-2560.
103. S. K. Hsiung, C. T. Chen and G. B. Lee, *J Micromech Microeng*, 2006, **16**, 2403-2410.
104. C. Y. Lee, Y. H. Lin and G. B. Lee, *Microfluid Nanofluid*, 2009, **6**, 599-610.
105. A. R. Abate, M. B. Romanowsky, J. J. Agresti and D. A. Weitz, *Appl Phys Lett*, 2009, **94**, 023503.
106. C. N. Baroud, J. P. Delville, F. Gallaire and R. Wunenburger, *Phys Rev E*, 2007, **75**, 046302.
107. N. T. Nguyen, T. H. Ting, Y. F. Yap, T. N. Wong, J. C. K. Chai, W. L. Ong, J. Zhou, S. H. Tan and L. Yobas, *Appl Phys Lett*, 2007, **91**, 084102.
108. C. A. Stan, S. K. Y. Tang and G. M. Whitesides, *Anal Chem*, 2009, **81**, 2399-2402.
109. W. Li, E. W. K. Young, M. Seo, Z. Nie, P. Garstecki, C. A. Simmons and E. Kumacheva, *Soft Matter*, 2008, **4**, 258-262.
110. M. Hashimoto, S. S. Shevkoplyas, B. Zasonska, T. Szymborski, P. Garstecki and G. M. Whitesides, *Small*, 2008, **4**, 1795-1805.
111. H. Willaime, V. Barbier, L. Kloul, S. Maine and P. Tabeling, *Phys Rev Lett*, 2006, **96**,

054501.
112. J. C. Galas, D. Bartolo and V. Studer, *New J Phys*, 2009, **11**, 075027.
113. S. J. Zeng, B. W. Li, X. O. Su, J. H. Qin and B. C. Lin, *Lab Chip*, 2009, **9**, 1340-1343.
114. J. Xu and D. Attinger, *J Micromech Microeng*, 2008, **18**, 065020.
115. A. Bransky, N. Korin, M. Khoury and S. Levenberg, *Lab Chip*, 2009, **9**, 516-520.
116. K. Churski, P. Korczyk and P. Garstecki, *Lab Chip*, 2010, **10**, 816-818.
117. F. Malloggi, S. A. Vanapalli, H. Gu, D. van den Ende and F. Mugele, *J Phys-Condens Mat*, 2007, **19**, 462101.
118. F. Malloggi, H. Gu, A. G. Banpurkar, S. A. Vanapalli and F. Mugele, *Eur Phys J E*, 2008, **26**, 91-96.
119. Y. C. Tan, J. S. Fisher, A. I. Lee, V. Cristini and A. P. Lee, *Lab Chip*, 2004, **4**, 292-298.
120. Y. C. Tan, Y. L. Ho and A. P. Lee, *Microfluid Nanofluid*, 2007, **3**, 495-499.
121. K. Liu, H. J. Ding, Y. Chen and X. Z. Zhao, *Microfluid Nanofluid*, 2007, **3**, 239-243.
122. N. Bremond, A. R. Thiam and J. Bibette, *Phys Rev Lett*, 2008, **100**, 024501.
123. B. C. Lin and Y. C. Su, *J Micromech Microeng*, 2008, **18**, 115005.
124. X. Niu, S. Gulati, J. B. Edel and A. J. deMello, *Lab Chip*, 2008, **8**, 1837-1841.
125. G. F. Christopher, J. Bergstein, N. B. End, M. Poon, C. Nguyen and S. L. Anna, *Lab Chip*, 2009, **9**, 1102-1109.
126. V. Chokkalingam, B. Weidenhof, M. Kramer, S. Herminghaus, R. Seemann and W. F. Maier, *Chemphyschem*, 2010, **11**, 2091-2095.
127. V. Chokkalingam, B. Weidenhof, M. Kramer, W. F. Maier, S. Herminghaus and R. Seemann, *Lab Chip*, 2010, **10**, 1700-1705.
128. S. D. Hudson, A. M. Jamieson and B. E. Burkhart, *J Colloid Interf Sci*, 2003, **265**, 409-421.
129. L. Mazutis, J. C. Baret and A. D. Griffiths, *Lab Chip*, 2009, **9**, 2665-2672.
130. J. Sivasamy, Y. C. Chim, T. N. Wong, N. T. Nguyen and L. Yobas, *Microfluid Nanofluid*, 2010, **8**, 409-416.
131. J. Bibette, D. C. Morse, T. A. Witten and D. A. Weitz, *Phys Rev Lett*, 1992, **69**, 2439-2442.
132. Y. Amarouchene, G. Cristobal and H. Kellay, *Phys Rev Lett*, 2001, **8720**, 206104.
133. M. L. Cordero, D. R. Burnham, C. N. Baroud and D. McGloin, *Appl Phys Lett*, 2008, **93**, 034107.
134. C. Priest, S. Herminghaus and R. Seemann, *Appl Phys Lett*, 2006, **89**, 134101.
135. M. Zagnoni, C. N. Baroud and J. M. Cooper, *Phys Rev E*, 2009, **80**, 046303.
136. M. Zagnoni and J. M. Cooper, *Lab Chip*, 2009, **9**, 2652-2658.
137. W. Wang, C. Yang and C. M. Li, *Small*, 2009, **5**, 1149-1152.
138. A. R. Thiam, N. Bremond and J. Bibette, *Phys Rev Lett*, 2009, **102**, 188304.
139. X. Z. Niu, F. Gielen, A. J. deMello and J. B. Edel, *Anal Chem*, 2009, **81**, 7321-7325.
140. A. Lai, N. Bremond and H. A. Stone, *J Fluid Mech*, 2009, **632**, 97-107.
141. M. Chabert, K. D. Dorfman and J. L. Viovy, *Electrophoresis*, 2005, **26**, 3706-3715.
142. S. Herminghaus, *Phys Rev Lett*, 1999, **83**, 2359-2361.
143. F. Mostowfi, K. Khristov, J. Czarnecki, J. Masliyah and S. Bhattacharjee, *Appl Phys Lett*, 2007, **90**, 184102.
144. J. C. Baygents, N. J. Rivette and H. A. Stone, *J Fluid Mech*, 1998, **368**, 359-375.

145. M. H. Davis, *Q. J. Mech. Appl. Math.*, 1964, **17**, 499.
146. T. J. Lewis, *IEEE trans. dielectr. electr. insul.*, 2003, **10**, 769-777.
147. W. H. Tan and S. Takeuchi, *Lab Chip*, 2006, **6**, 757-763.
148. J. A. Schwartz, J. V. Vykoukal and P. R. C. Gascoyne, *Lab Chip*, 2004, **4**, 11-17.
149. P. Singh and N. Aubry, *Electrophoresis*, 2007, **28**, 644-657.
150. W. Wang, C. Yang and C. M. Li, *Lab Chip*, 2009, **9**, 1504-1506.
151. R. M. Lorenz, J. S. Edgar, G. D. M. Jeffries, Y. Q. Zhao, D. McGloin and D. T. Chiu, *Anal Chem*, 2007, **79**, 224-228.
152. E. Verneuil, M. L. Cordero, F. Gallaire and C. N. Baroud, *Langmuir*, 2009, **25**, 5127-5134.
153. A. Manz, D. J. Harrison, E. M. J. Verpoorte, J. C. Fettinger, A. Paulus, H. Ludi and H. M. Widmer, *J Chromatogr*, 1992, **593**, 253-258.
154. Z. H. Fan and D. J. Harrison, *Anal Chem*, 1994, **66**, 177-184.
155. Y. N. Xia and G. M. Whitesides, *Annu Rev Mater Sci*, 1998, **28**, 153-184.
156. D. Qin, Y. N. Xia, J. A. Rogers, R. J. Jackman, X. M. Zhao and G. M. Whitesides, *Microsystem Technology in Chemistry and Life Science*, 1998, **194**, 1-20.
157. B. Bohl, R. Steger, R. Zengerle and P. Koltay, *J Micromech Microeng*, 2005, **15**, 1125-1130.
158. D. Belder and M. Ludwig, *Electrophoresis*, 2003, **24**, 3595-3606.
159. K. Handique, D. T. Burke, C. H. Mastrangelo and M. A. Burns, *Anal Chem*, 2000, **72**, 4100-4109.
160. T. Rohr, D. F. Ogletree, F. Svec and J. M. J. Frechet, *Adv Funct Mater*, 2003, **13**, 264-270.
161. A. R. Abate, D. Lee, T. Do, C. Holtze and D. A. Weitz, *Lab Chip*, 2008, **8**, 516-518.
162. S. W. Hu, X. Q. Ren, M. Bachman, C. E. Sims, G. P. Li and N. L. Allbritton, *Anal Chem*, 2004, **76**, 1865-1870.
163. P. A. Willis, B. D. Hunt, V. E. White, M. C. Lee, M. Ikeda, S. Bae, M. J. Pelletier and F. J. Grunthaner, *Lab Chip*, 2007, **7**, 1469-1474.
164. W. H. Grover, M. G. von Muhlen and S. R. Manalis, *Lab Chip*, 2008, **8**, 913-918.
165. Y. J. Song, C. S. S. R. Kumar and J. Hormes, *J Micromech Microeng*, 2004, **14**, 932-940.
166. Z. T. Cygan, J. T. Cabral, K. L. Beers and E. J. Amis, *Langmuir*, 2005, **21**, 3629-3634.
167. S. H. Kim, Y. Yang, M. Kim, S. W. Nam, K. M. Lee, N. Y. Lee, Y. S. Kim and S. Park, *Adv Funct Mater*, 2007, **17**, 3493-3498.
168. D. Bartolo, G. Degre, P. Nghe and V. Studer, *Lab Chip*, 2008, **8**, 274-279.
169. C. De Marco, S. Girardo, E. Mele, R. Cingolani and D. Pisignano, *Lab Chip*, 2008, **8**, 1394-1397.
170. L. H. Hung, R. Lin and A. P. Lee, *Lab Chip*, 2008, **8**, 983-987.
171. R. Simms, S. Dubinsky, A. Yudin and E. Kumacheva, *Lab Chip*, 2009, **9**, 2395-2397.
172. B. D. Gates, Q. B. Xu, J. C. Love, D. B. Wolfe and G. M. Whitesides, *Annu Rev Mater Res*, 2004, **34**, 339-372.
173. M. Heckele and W. K. Schomburg, *J Micromech Microeng*, 2004, **14**, R1-R14.
174. P. W. Leech, N. Wu and Y. Zhu, *J Micromech Microeng*, 2009, **19**, 065019.
175. J. Greener, W. Li, J. Ren, D. Voicu, V. Pakharenko, T. Tang and E. Kumacheva, *Lab Chip*, 2010, **10**, 522-524.
176. C. W. Tsao and D. L. DeVoe, *Microfluid Nanofluid*, 2009, **6**, 1-16.

Chapter 3

Electrowetting — A Versatile Tool for Controlling Droplet Generation in Microfluidic Channels*

Abstract

Integrating insulator-covered electrodes into a microfluidic flow focusing device, we demonstrate enhanced flexibility and control of the flow of two immiscible liquids based on electrowetting. In the parameter space, determined by the liquid inlet pressures, we identify a specific region where droplets can only be generated and addressed via electrowetting. In this regime we show that the size distribution and the frequency of droplet generation can be controlled by the applied voltage and the width of voltage pulses. Moreover it turns out that with electrowetting the droplet size and the frequency can be tuned independently. Finally we show that the same droplet generation phenomena can also be observed in the presence of surfactants.

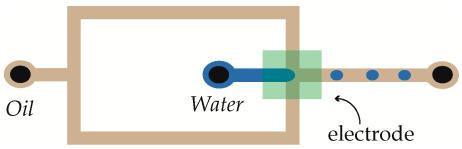

* This chapter has been published in Eur. Phys. J. E 2008, **26**, 91-96

3.1 Introduction

The growing trend towards miniaturization of experimental systems and the development of advanced functional materials have facilitated the expansion of droplet-based applications. Droplets of one fluid in a second immiscible fluid also known as emulsions, foams or aerosols are increasingly investigated in microfluidics.[1] The generation of a droplet is the result of two competing phenomena: viscous forces stretch the fluid along the flow and capillary forces try to minimize the total interface between the two phases. Aqueous droplets are commonly generated in a continuous oil phase in a microchannel format by using T-junction configurations[2] or with flow focusing geometries[3-4], where the droplet size is comparable to the channel diameter and can be tuned by varying the shear rates of the oil phase relative to the aqueous phase.[5] This process is nicely reproducible and high monodispersity is reached.[6] Each droplet represents an independent nanoliter volume. The resulting droplets are being used as microreactors[7] in chemical kinetics,[8] chemical and biological analysis,[9-10] material synthesis[11-13] and protein crystallization[14]. Due to the small quantity of reagent involved in such processes there is a particular interest when the droplet size and the size distribution can be prescribed on a micro- or nano- scale (nanoliter and less). Despite the significant advances made in the past few years, major challenges remain in the development of microchannel droplet control,[15] such as flexibility of the generation rate (droplet-on-demand or continuous formation), independent control of the droplet size and the droplet generation frequency. Whereas droplet generation is currently controlled by tuning the input flow rates, this affects simultaneously the frequency, size and speed of the droplets. One way to avoid that is to use an electrostatic actuation with integrated electrodes. The gain in control should increase but the danger is that such devices become too sophisticated and lose flexibility and versatility.

In this study we adopt a simple approach combining two existent technologies to create a soft microfluidic platform. We achieve this integration by incorporating an EW system into a flow focusing device (FFD). This novel combination offers high throughput capability (as has been demonstrated in pressure-driven FFD) and exquisite control over the individual droplet[16-17] and surface wettability[18-19] by

EW. Here, we identify experimentally the range of voltages and driving pressures that yield EW-induced droplet generation. We measure the size distribution and the frequency of droplet formation under EW. In the absence of surfactant droplets are thermodynamically metastable and coalesce when they come into contact. Typically, a surfactant is essential to stabilize the droplets against coalescence. At the same time surfactant affects the wetting properties of the fluid[20] which might compromise the efficiency of EW. Hence we test EW-induced droplet generation control in the presence of two different surfactants, one soluble in oil and one in water by repeating the same set of experiments performed with plain water.

This chapter is organized as follows. In Section 3.2 we introduce the experimental set-up (Sect. 3.2.2) and the phase diagram of EW-induced droplet generation (Sect. 3.2.3). In Section 3.3, we study the size distribution and the frequency of droplet generation as a function of both applied voltage and the width of voltage pulses. Section 3.4 is devoted to the effect of surfactants on the EW-controlled droplet generation. We close with conclusions and suggested perspectives.

3.2 Electrowetting-based Flow Focusing Device

In the following three subsections, we describe the EW principle, the experimental set-up and the phase diagram obtained with our set of control parameters.

3.2.1 Electrowetting principle

In electrowetting, one is generally dealing with droplets of partially wetting conductive liquids on planar solid substrates. The ambient medium can be either air or another immiscible electrically insulating liquid, frequently oil. For typical droplet sizes $R < 1$ mm, the Bond number $Bo = \Delta\rho g L^2/\sigma$, which measures the strength of gravity with respect to surface tension, is smaller than unity. Therefore we neglect gravity throughout the rest of this chapter. In the absence of external electric fields, the shape of a droplet deposited on a surface depends on the energies of the various interfaces; the resulting contact angle θ of the liquid with the surface is given by the well-known Young equation.[21] In recent years, the standard configuration for electrostatic actuation is to coat a thin dielectric on top

of the electrode in order to eliminate the problem of fluid electrolysis: this concept is known as electrowetting (on dielectric) (EW).[22] Under these conditions, applying a voltage between the conductive droplet and the electrode gives rise to electrostatic charging of the plate capacitor formed by the droplet, the dielectric and the electrode. In this case electrowetting leads to an effective reduction of the solid-liquid interfacial energy $\sigma'_{sl} = \sigma_{sl} - cU^2/2$, where $c = \varepsilon_0\varepsilon_r/d$ is the capacitance per unit area between the droplet and the substrate. $\varepsilon_0\varepsilon_r$ is the dielectric permittivity of the insulating layer and d the dielectric thickness. The apparent contact angle $\theta(U)$ depends on both Young's angle θ_Y and the applied voltage U [19]:

$$\cos\theta(U) = \cos\theta_Y + \frac{c}{2\sigma}U^2 \tag{3.1}$$

where σ is the interfacial tension between the droplet and the ambient medium. Note that Eq. 3.1 remains valid for *ac* voltage if one replaces U with its root mean square (rms) value U_{rms}. In the following we will drop the subscript rms for simplicity.

3.2.2 Experimental set-up

The geometry of the EW-based FFD is illustrated in Fig. 3.1a. The device was made in polydimethylsiloxane (PDMS) using standard soft lithography by replicating from photoresist (SU-8) molds.[23] The PDMS structure was clamped mechanically onto a planar electrode: an indium tin oxide (ITO)–covered glass substrate, which was dip-coated with a hydrophobic layer of Teflon AF (≈ 8 μm) that also acts as a dielectric (Fig. 3.1b). A thin electrical wire was plunged into the aqueous phase. The electrode was connected to an *ac* function generator (10 kHz) in combination with an amplifier. The fluid flow at the aqueous (deionized water + NaCl with a conductivity, 10 mS/cm) and oil (mineral oil μ_o = 0.03 Pa·s, ρ_o = 875 kg/m^3) inlets was driven using hydrostatic heads with a precision of 1 Pa (≡ 0.1 mm). Young's contact angles measured through the water phase on the top (PDMS) and bottom (Teflon AF) surface are θ_{top} = 160° and θ_{bot} = 170°, respectively. For the purpose of the study of Section 3.4 we also used non-ionic surfactants Triton X-100 in water and Span 80 in oil with a concentration c = 1 wt%. The oil-water interfacial tension was measured to be σ = 38 mN/m (3.1 mN/m with Triton X-100, 5 mN/m with Span 80) with a plate method from a tensiometer (Kruss K11,Germany).

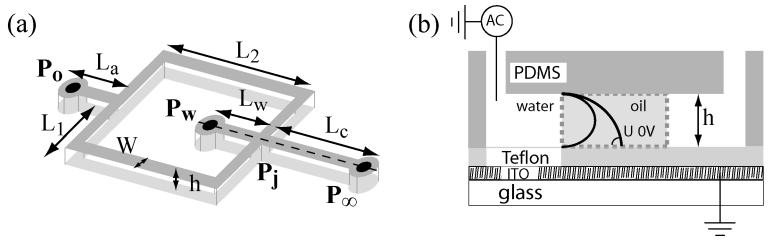

Figure 3.1 (a) Schematics of the electrowetting-based flow focusing device (EW-based FFD). Geometry and channels' dimensions: width (W = 390 μm), height h and lengths (L_a, $L_0 = L_1 + L_2$, L_w, L_c). (b) Cross-section along the dashed line (see a).

3.2.3 Phase diagram of electrowetting-induced droplet generation

We generate the phase diagram of EW-induced droplet generation by varying three control parameters — inlet water pressure (P_w), inlet oil pressure (P_o) and the voltage (U). Fig. 3.2a reports the resulting phase diagram. At low water pressure the water-oil interface remains stable, above a threshold droplets are generated (Fig. 3.2b) and finally continuous jets are formed for high water pressures (not reported here). Varying the oil pressure, we obtained a linear onset curve P^*_w (P_o) for the generation of droplets (filled squares and full line in Fig. 3.2a) under purely hydrodynamic conditions. Similar experiments were conducted, however, now under a series of applied voltages up to U_{max} = 150V. Again, the critical water pressure turned out to increase linearly with P_o — exactly with the same slope λ as in the purely hydrodynamic case. Denoting the voltage-dependent critical water pressure at $P_o = 0$ as $P_L(U)$, we thus find a family of onset curves described by

$$P^*_w(U) = P_L(U) + \lambda P_o \tag{3.2}$$

This family of curves signifies a region (hatched region in Fig. 3.2a), in which droplets can be formed by electrowetting but not by purely hydrodynamics forces. Thus, operating in this region allows EW-driven droplet-on-demand control. We find that the range of this window is limited by contact line instability induced by strong electrostatic fields.[22,24] Moreover, this family of curves is completely predictable and involves two different physical phenomena. First, the term $P_L(U)$ is an electrowetting modified Laplace pressure $P_L(U) \approx \gamma(2/W + 1/R_h(U))$ where $R_h(U)$ is the radius of curvature along the height h (see inset of Fig. 3.2a). While θ_{top} is constant, the contact angle on the bottom surface, $\theta(\eta)$, decreases with increasing voltage following the well-known electrowetting equation[19] :

$$\cos\theta(\eta) = \cos\theta_{bot} + \eta \tag{3.3}$$

Here $\eta = \varepsilon_0\varepsilon_r U^2/2d\sigma$ is the dimensionless EW number, which measures the relative strength of electrostatic and surface tension forces. ε_0 and ε_r (= 2) are the dielectric constant and the vacuum permittivity, and d is the thickness of dielectric layer. A geometric construction establishes a link between R_h and θ (inset of Fig. 3.2a)

$$\frac{1}{R_h(\eta)} = -\frac{2}{h}\cdot\cos\left(\frac{\theta(\eta)-\theta_{top}}{2}\right)\cdot\cos\left(\frac{\theta(\eta)+\theta_{top}}{2}\right) \tag{3.4}$$

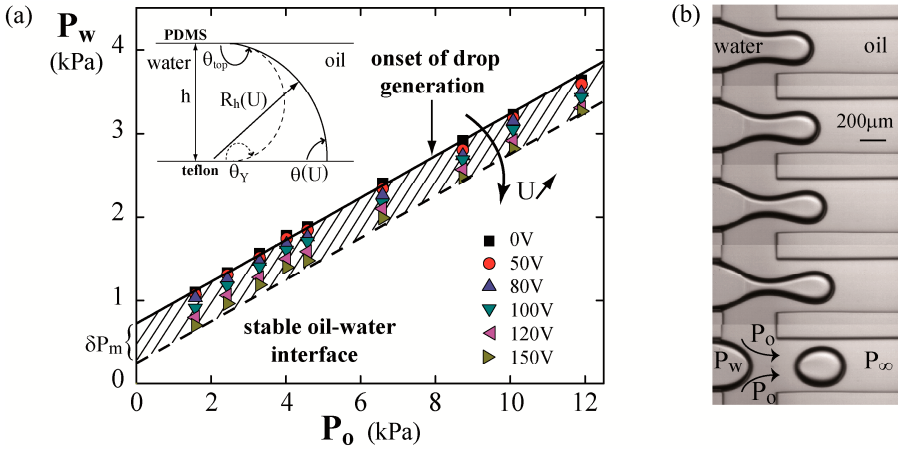

Figure 3.2 (a) Phase diagram identifying the regime of droplet formation in EW-based FFD (h = 190 μm, W = 390 μm, μ_o/μ_w = 30). Hatched area: EW-tuning window with width $\delta P_m = P_L(0) - P_L(U_{max})$. Inset: cross-sectional sketch of the interface inside the channel: without EW (dotted line), with EW (solid line). (b) Last 100 ms of a droplet formation, time step of 16 ms between successive pictures (U = 80 V).

Hence the expression of $P_L(\eta)$ is obtained by using Eq. 3.3 and 3.4, and agrees with our experimental data.[25] Second, λ is due to channel resistance. Considering the hydrodynamic circuit of our device,[26] one can write the local hydrostatic pressure at the junction P_j as a function of channel resistance Ω ($\approx \mu L/Wh^3$, where μ is the viscosity of the fluid in the corresponding channel segment of length L)

$$P_j = P_o\cdot\Omega_c/(\Omega_a + \Omega_o/2 + \Omega_c) \tag{3.5}$$

The subscripts denote the various channel segments as sketched in Fig. 3.1a. Inserting the values of the different resistances of the channels, we find λ = 0.26 in excellent agreement with the experimentally determined value λ = 0.25 ± 0.01.

Note that the onset of droplet generation is exclusively controlled by static argument and not affected (within experimental accuracy) by viscous shear forces. For the subsequent droplet formation process, however, viscous forces are important.

3.3 Droplet Size and Frequency Control

In this section we investigate how EW can control the droplet size and/or frequency of droplet generation. Two different ways are reported below, one consists of increasing the electrostatic force and the second of generating voltage pulses for a given electrostatic force.

3.3.1 Tuning the electrowetting strength

In addition to controlling whether droplets are being generated at all, EW also allows for controlling the size of the droplets, as shown in Fig. 3.3a. For four different points in the phase diagram just below the zero-voltage onset line, we produced droplets by increasing η in a series of steps from 0 to 1. The droplet size consistently increased with increasing voltage especially in the lowest P_o. The maximum ratio between the volume of the smallest and the largest droplets was ≈ 3.2 for the present system.

How can we intuitively explain the effect of EW on droplet size? Let us consider a configuration without EW where the water-oil interface is stable and located just at the entrance of cross junction. In this configuration the Laplace pressure P_L exactly balances the inlet water pressure P_w. However, when EW is applied this configuration becomes unstable. The water pressure P_w is now too high compared to the modified Laplace pressure $P_L(\eta)$ (since P_L decreases with η, see Eq. 3.4) hence the interface moves toward the cross junction. This new position (although dynamically evolving) defines the volume of the droplet and depends on the value of $P_L(\eta)$. If the interface exceeds the cross junction, the viscous stress destabilizes the water interface and generates a droplet. This simple picture explains how the droplet size is controlled by the strength of EW. The volume tuning range decreased with increasing oil pressure (*i.e.* flow rate), consistent with an increasing strength of the viscous forces with respect to electrostatic forces.

Interestingly, we also measured the rate of droplet formation f (see Fig. 3.3b). Plotting f as a function of the control parameter η shows, despite some scatter, an exponential behavior. In case of high P_o the droplet size does not change with EW but the droplet generation frequency is significantly modified, a variation of a decade is observed. This result is important since it allows to vary the frequency without changing the droplet size.

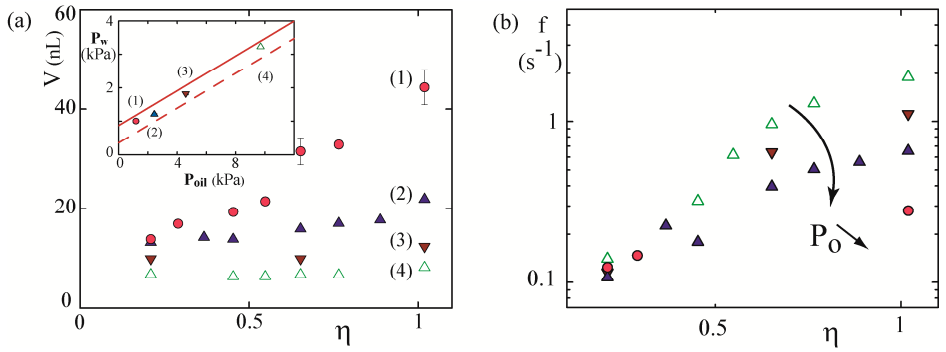

Figure 3.3 (a) Droplet volume evolution with an increasing EW effect for different points inside the EW droplet generation window (1) - (4). Inset: phase diagram of a channel 100 μm height obtained from the model. The EW droplet generation window corresponds to the region between the two curves $\eta = 0$ and $\eta = 1.3$. (b) Droplet generation frequency for different η.

3.3.2 Generating pulses

The electrostatic force is maximized ($\eta \approx 1$) and we modulated the amplitude of 10kHz driving voltage by making train of *ac* pulses with a periodicity T and a width τ (see inset of Fig. 3.4). We focused on the influence of the pulse width τ on the droplet properties using a periodicity T much larger than the time needed for creating a droplet. In practice we used $T = 5$ s and each pulse is decoupled from the previous one and generates only one droplet. Fig. 3.4 shows how the droplet volume changes with a pulse from finite to infinite width τ (in practice infinite means ≥ 10 s). Below a critical pulse width, the interface stays stable and no droplets are being generated. Above it, droplets are generated, the volume tuning range decreases with increasing oil pressure as seen in the previous section. The maximum ratio is around 2.2 and is obtained for the lowest inlet oil pressure. Interestingly, we see a distinct transition in the volume evolution. First, V is linear

with τ and then reaches a plateau whose value depends on the inlet oil pressure. Moreover, the higher the inlet oil pressure, the lower the droplet volume.

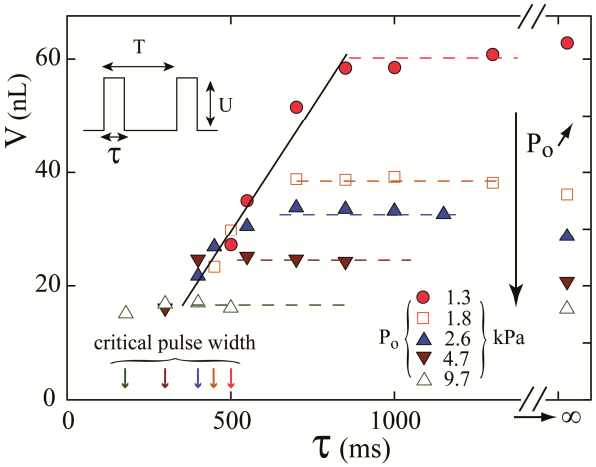

Figure 3.4 Droplet volume evolution with an increasing pulse width τ for different points inside the EW droplet generation window (h = 190 µm, P_o = 1.3, 1.8, 2.6, 4.7, 9.7 kPa). Inset: sketch of the pulse generation: *ac* frequency pulses of the rms voltage U are applied during the time τ with a periodicity T.

Looking at the interface configuration upon pinch-off gives a qualitative explanation for the transition. In the linear regime the droplet pinch-off occurs after the voltage pulse ended, whereas in the plateau region the pinch-off occurs during the pulse, *i.e.* with voltage on. When a voltage is imposed the interface moves due to the EW effect. If the time of the pulse is too short, the water interface is not brought into the cross-section and no droplet is generated. Above this minimum pulse time (or critical pulse width) the interface is brought up to the cross-junction, then viscous forces shear the water interface and droplets are generated. As long as τ stays lower than the timescale of the droplet generation (but above the critical pulse width), the volume of the droplet is proportional to τ (see linear regime in Fig. 3.4). When τ becomes larger than the timescale of the droplet generation, the volume trapped remains constant with a value depending on the viscous shear stress (see the different plateaus in Fig. 3.4). It is worth noting that even if EW is still actuated the pinch-off is induced and governed by viscous forces.

3.4 Electrowetting and Surfactant

In this section, we describe the effect of EW in the presence of surfactants. Two types of non-ionic surfactants, one soluble in water (Triton X-100) and the other one soluble in oil (Span 80), were utilized separately. The concentrations of surfactant are far above the critical micellar concentration.[4,6] In such case the interface is fully covered by surfactants (saturation) and micelles start to form within the solution, and the interfacial tension is almost constant. The main effect of the surfactant is to reduce the surface tension between the water-oil interface. The water-oil interfacial tension was measured to be σ = 3.1 mN/m with Triton X-100 and σ = 5 mN/m with Span 80. The contact angles are roughly identical to those with pure water: Triton X-100 gives θ_{top} = 152°, θ_{bot} = 140° and Span 80 in oil gives $\theta_{top} = \theta_{bot}$ = 156°.

3.4.1 EW-controlled tuning window

We produce the phase diagram in the same way as in Section 3.2. The similar families of onset curves are observed (Eq. 3.2). As expected, onset curves are shifted towards lower water pressure (see Fig. 3.5): due to the surfactant, the surface tension is one order of magnitude lower, thus the Laplace pressure is much smaller. For the same reason the EW-controlled tuning window, $\delta P_m = P_L(0) - P_L(U_{max})$, is also reduced compared to the pure liquid (see Fig. 3.5). δP_m is ten times smaller now (O(100)Pa). The slope of the transition curves is similar to the one obtained for plain water. The slope is linked to the geometry of the channel, which has not changed. Extrapolation of the transition curve for the hydrodynamic case (no voltage) gives an intercept $P_L \approx 0.048$ kPa for Triton X-100 and $P_L \approx 0.08$ kPa for Span 80 in good agreement with the expected reduction of the Laplace pressure (Triton X-100, P_L = 0.041 kPa; Span80, P_L = 0.078 kPa), see inset of Fig. 3.5b for experiment and model comparison. The inset of Fig. 3.5a shows the electrowetting curve with surfactants. As the electrowetting number η is inversely proportional to the surface tension σ, according to Eq. 3.3, lower voltages are required for reaching the same contact angles as for pure water. For instance, to reach θ = 80°, U = 50 V is needed instead of U = 150 V.

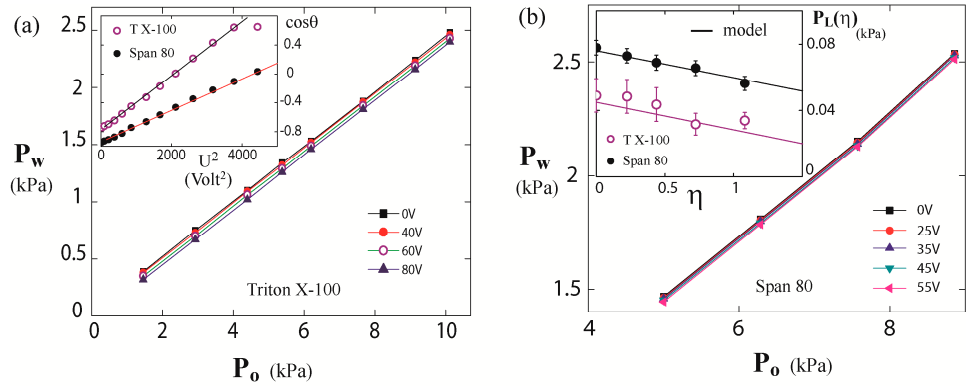

Figure 3.5 Phase diagram (similar to Fig. 3.2) in the presence of surfactants: (a) Triton X-100 in aqueous phase. (b) Span 80 in oil phase. Inset of (a): EW curves of these two situations. Inset of (b): EW modified Laplace pressure $P_L(U)$: experimental data (symbols) and model (solid lines) channel height: h = 190 μm.

3.4.2 Droplet generation: electrowetting strength and pulses

In the following section only Triton X-100 surfactant is studied. Experiments similar to that used to generate Fig. 3.3 and Fig. 3.4 are reproduced. The general behavior is similar to that seen without surfactant. However, the size of the droplets does not change when the strength of EW is increased (Fig. 3.6a). With pulses we also found a similar behavior (Fig. 3.6b). In these cases we directly see a plateau. This is due to the range of capillary number $Ca = \mu_o v/\sigma$ investigated (v is the average velocity of the oil flow). For the range of P_o used, we have in the presence of surfactant, $0.5 \leq Ca \leq 1.5$ whereas for pure water it was $0.02 \leq Ca \leq 0.1$. One can compare the viscous forces and the electrostatic ones by making the ratio $\eta/Ca = \varepsilon_0\varepsilon_r U^2/2d\mu_o v$. In the case of droplet generation experiments with pure water the smallest P_o gives $\eta/Ca \approx 50$ whereas, with surfactant, the smallest P_o gives $\eta/Ca \approx$ O(1). Hence, even with the lowest P_o, the viscous forces are already strong compared to the electrostatic forces. Therefore in the experimental parameter range investigated with surfactants, we directly observe a plateau behavior. The droplet volume remains mostly constant and independent of η. In contrast the frequency of droplet emission f varies with η by approximately one decade.

We extend the study of the EW strength by increasing the voltage above the

contact line instability ($\eta \geq 1$). A first observation shows two types of droplet formation. The standard one where the entire water-oil interface is sheared until a pinch-off which creates a droplet. A second one, due to high electric field, leads to polydisperse tiny droplets (≈ picoliter) generated along the contact line (see snapshots in Fig. 3.6a). In the present measurements we only report the droplet volume linked to pinch-off mechanism. The volume V reduces with η; this effect is more pronounced at low Ca as is visible in Fig. 3.6a for $\eta \geq 1$. The inset of Fig. 3.6a shows that the frequency f increases with the increase of η.

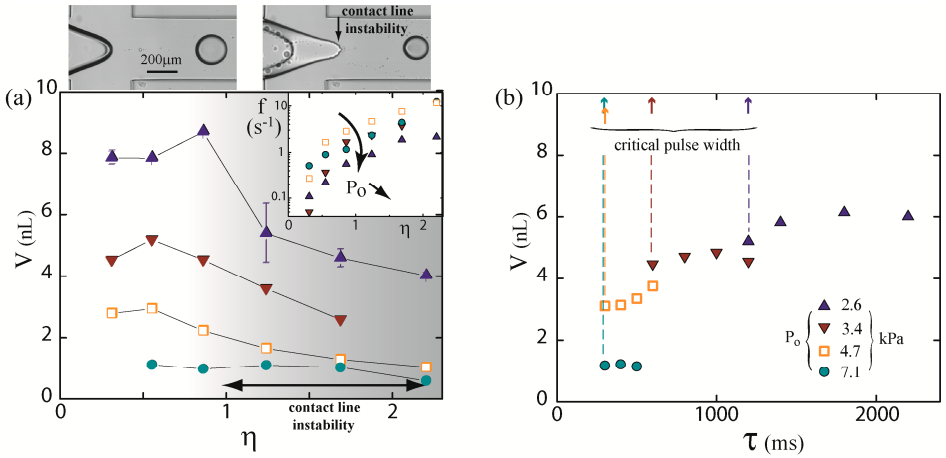

Figure 3.6 (a) Droplet volume evolution with an increasing EW effect for different points inside the EW droplet generation window (h = 190 µm, P_o = 2.6, 3.4, 4.7, 7.1 kPa). Inset: Droplet generation frequency as a function of η. Optical microscopy images: droplet generation in the absence / presence of the contact line instability. (b) Droplet volume evolution with an increasing pulse width τ (h = 190 µm, η = 0.86, P_o = 2.6, 3.4, 4.7, 7.1 kPa).

3.5 Conclusions

In conclusion, we have successfully integrated insulator-covered electrodes into a flow focusing device fabricated with soft lithography techniques. The operating diagram of droplet formation as a function of the oil pressure P_o, water pressure P_w and voltage U shows a new regime specifically based on EW actuation. When viscous forces are weak compared to electrostatic ones (*i.e.* at low P_o), the droplet size can be varied by a factor of three by using EW. When viscous forces become stronger, the droplet size remains constant but the frequency of droplet

generation is significantly changed; a variation of a decade is observed. This result represents an important step since it demonstrates the possibility to decouple the droplet size and the frequency of droplet generation. In addition, EW is still efficient in the presence of surfactants suggesting EW-controlled droplet generation as a possible route for producing stable emulsion.

Additional flexibility with respect to droplet size control is expected by combining the current strategy with suitable patterned electrodes. Furthermore, exploring the use of the contact line instability at high voltage may give access to extremely small droplets.

Acknowledgements

The author acknowledges MicroNed, the Microtechnology Research Programme of the Netherlands for financial support, as well as the research institutes IMPACT and MESA+ at Twente University.

References

1. H. A. Stone, A. D. Stroock and A. Ajdari, *Annu Rev Fluid Mech*, 2004, **36**, 381-411.
2. T. Thorsen, R. W. Roberts, F. H. Arnold and S. R. Quake, *Phys Rev Lett*, 2001, **86**, 4163-4166.
3. A. M. Ganan-Calvo, *Phys Rev Lett*, 1998, **80**, 285-288.
4. S. L. Anna, N. Bontoux and H. A. Stone, *Appl Phys Lett*, 2003, **82**, 364-366.
5. J. D. Tice, A. D. Lyon and R. F. Ismagilov, *Anal Chim Acta*, 2004, **507**, 73-77.
6. P. Garstecki, H. A. Stone and G. M. Whitesides, *Phys Rev Lett*, 2005, **94**, 164501.
7. H. Song, D. L. Chen and R. F. Ismagilov, *Angew Chem Int Edit*, 2006, **45**, 7336-7356.
8. H. Song, J. D. Tice and R. F. Ismagilov, *Angew Chem Int Edit*, 2003, **42**, 768-772.
9. M. Y. He, J. S. Edgar, G. D. M. Jeffries, R. M. Lorenz, J. P. Shelby and D. T. Chiu, *Anal Chem*, 2005, **77**, 1539-1544.
10. Y. C. Tan, K. Hettiarachchi, M. Siu and Y. P. Pan, *J Am Chem Soc*, 2006, **128**, 5656-5658.
11. S. Xu, Z. Nie, M. Seo, P. Lewis, E. Kumacheva, H. A. Stone, P. Garstecki, D. B. Weibel, I. Gitlin and G. M. Whitesides, *Angew Chem Int Edit*, 2005, **44**, 3799-3799.
12. A. Fernandez-Nieves, G. Cristobal, V. Garces-Chavez, G. C. Spalding, K. Dholakia and D. A. Weitz, *Adv Mater*, 2005, **17**, 680-684.
13. Z. H. Nie, S. Q. Xu, M. Seo, P. C. Lewis and E. Kumacheva, *J Am Chem Soc*, 2005, **127**, 8058-8063.
14. B. Zheng and R. F. Ismagilov, *Angew Chem Int Edit*, 2005, **44**, 2520-2523.
15. M. Joanicot and A. Ajdari, *Science*, 2005, **309**, 887-888.
16. S. K. Cho, H. J. Moon and C. J. Kim, *J Microelectromech S*, 2003, **12**, 70-80.
17. R. B. Fair, *Microfluid Nanofluid*, 2007, **3**, 245-281.

18. M. G. Pollack, R. B. Fair and A. D. Shenderov, *Appl Phys Lett*, 2000, **77**, 1725-1726.
19. F. Mugele and J. C. Baret, *J Phys-Condens Mat*, 2005, **17**, R705-R774.
20. R. Dreyfus, P. Tabeling and H. Willaime, *Phys Rev Lett*, 2003, **90**, 144505.
21. T. Young, *Philos. Trans. R. Soc. London*, 1805, **95**, 65.
22. M. Vallet, M. Vallade and B. Berge, *Eur Phys J B*, 1999, **11**, 583-591.
23. D. C. Duffy, J. C. McDonald, O. J. A. Schueller and G. M. Whitesides, *Anal Chem*, 1998, **70**, 4974-4984.
24. F. Mugele and S. Herminghaus, *Appl Phys Lett*, 2002, **81**, 2303-2305.
25. F. Malloggi, S. A. Vanapalli, H. Gu, D. van den Ende and F. Mugele, *J Phys-Condens Mat*, 2007, **19**, 462101.
26. J. B. Knight, A. Vishwanath, J. P. Brody and R. H. Austin, *Phys Rev Lett*, 1998, **80**, 3863-3866.

Chapter 4

Electrowetting-enhanced Microfluidic Device for Droplet Generation*

Abstract

We integrated electrowetting into a microfluidic flow focusing device to study droplet generation under the influence of electric fields. Using both the dispersed phase inlet pressure and the applied voltage as control parameters we find that the range of droplet sizes and the droplet generation rate can be controlled in a much finer way than with hydrodynamics alone. In particular a "conical spray" regime occurring at a voltage of O(50V) allows for continuous tuning of the (highly monodisperse) droplet diameter from ≈ 5 to 50 μm at a fixed continuous flow rate.

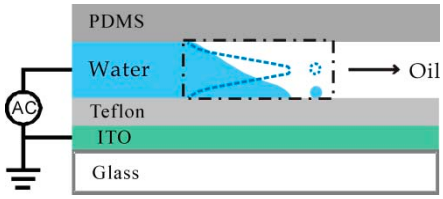

* This chapter has been published in Appl. Phys. Lett. 2008, **93**, 183507

4.1 Introduction

The generation of droplet with controlled size-distribution is a key prerequisite for various industrial fields such as pharmaceuticals[1] and food engineering[2]. In recent years, microfluidic devices have been developed as versatile tools to produce droplets.[3-7] The most common microchannel geometries for generating droplets are T-junctions[8-9] and flow focusing devices (FFDs)[10-11]. The droplet size is usually controlled by tuning the flow rates of the continuous and the dispersed phase. One limitation of this approach is, however, that the orifice size and the relative strength of interfacial tension and hydrodynamic shear forces limit the range of droplet size that can be generated. Alternatively, electrically assisted mechanisms, such as electrospraying[12] are a promising approach providing active and precise control of the droplet generation and the potential to access a wider range of droplet sizes.[13] Kim *et al*.[4] integrated electrodes into a microfluidic FFD to generate micrometer-sized droplets in an electrospraying-like process requiring voltages in excess of 1000 V. In our previous study, we introduced the concept of integrating electrowetting (EW)[14] into continuous flow microfluidic devices.[15-16] Chapter 3 focuses on the physical mechanism controlling the generation of relatively large droplets (tens of micrometers) at low flow rates.

In the present chapter, we demonstrate that flexible generation of micrometer-sized droplets can be achieved in a FFD with EW. Depending on the applied voltage and the dispersed phase pressure, we observed several distinct regimes of droplet generation, including a novel regime producing micrometer-sized charged droplets similar to conical sprays in electrospraying.[17] We also find that the droplet size can be tuned continuously upon varying the applied voltage bridging the gap between very small and rather large droplets generated in the purely hydrodynamic regimes of tip-streaming and dripping, respectively.

4.2 Experimental

The experimental setup is based on a FFD (Fig. 4.1a) enhanced by EW capability (Fig. 4.1b) with a channel geometry that incorporates an orifice at the outlet. The microchannel was fabricated by polydimethylsiloxane (PDMS) using standard soft lithography.[18] The molded PDMS structure was clamped mechanically onto an

indium-tin oxide (ITO) covered glass substrate that was dip-coated with a hydrophobic Teflon AF layer (≈ 6 μm) as a dielectric beforehand. Deionized water with dissolved NaCl (conductivity is 5 - 7 mS/cm) was used as dispersed phase. The continuous phase is mineral oil (viscosity, 0.03 Pa·s) with span 80 (5 wt%) added as a surfactant. The interfacial tension (σ) of water-oil with span 80 was measured to be 5 mN/m with a plate method using a commercial tensiometer (Kruss, Germany). The oil flow was driven using syringe pump (KDS200, KD Scientific, U.S.) and the pressure of the dispersed phase (P_w) was adjusted by a home-made hydrostatic head. A thin wire immersed into the aqueous phase was used to apply an *ac* voltage U (0 … 100 V_{rms} (root mean square)) with a frequency of 10 kHz. We monitored the generation of droplets as a function of P_w and U using a high speed camera (Photron FASTCAM-Ultima 512, Japan).

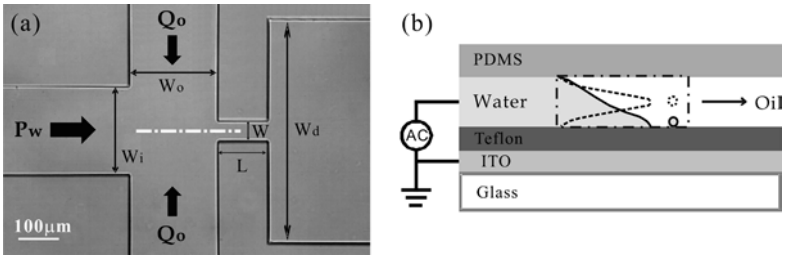

Figure 4.1 Flow focusing device integrated with electrowetting (a) Top view of the junction area. The dimensions of various sections are $W_i = W_o = 200$ μm, $W = 50$ μm, $L = 150$ μm and $W_d = 500$ μm. The height of channels h in the device is 50 μm. (b) Cross-sectional schematic of EW-based FFD. Dashed square indicates the junction area. Without voltage, the oil-water interface is in the middle of channel (dotted curves). With voltage, the oil-water interface is close down to the bottom.

The flow rate of the continuous oil phase was kept fixed at 108 μl/h throughout this study, corresponding to a capillary number $Ca = \mu_o v/\sigma$ of 0.072, where ν is the average velocity. Upon applying a voltage, the water contact angle (θ) in the device decreases following the EW equation $\cos\theta = \cos\theta_Y + \eta$ (see ref.19), where $\eta = CU^2/(2\sigma)$ is the dimensionless EW number that characterizes the relative strength of electrostatic and surface tension forces. (For the capacitance $C = 3.3$ μF/m² of the present device, the scales of surface tension and electrostatic forces are equal (*i.e.* $\eta = 1$) for $U \approx 55$ V.) $\theta_Y = 170°$ is Young's angle measured in the water phase.

4.3 Results and Discussion

Fig. 4.2 shows representative snapshots of droplets for variable P_w and U. We found four different regimes of operation of our device: if both P_w and U are low, no droplets are generated at all (a). For somewhat higher P_w and/or U, a thin water jet is ejected from the water-oil interface, (b), (f) and (g) (Note that there *is* a very fine jet in (b) and (f).) In this regime, which we denote as tip streaming, the droplets remain close to each other decorating the (somewhat asymmetric) flow field of the continuous phase. The droplet diameter is in the range of 1 - 2 μm, however it is difficult to determine whether coalescence occurs.

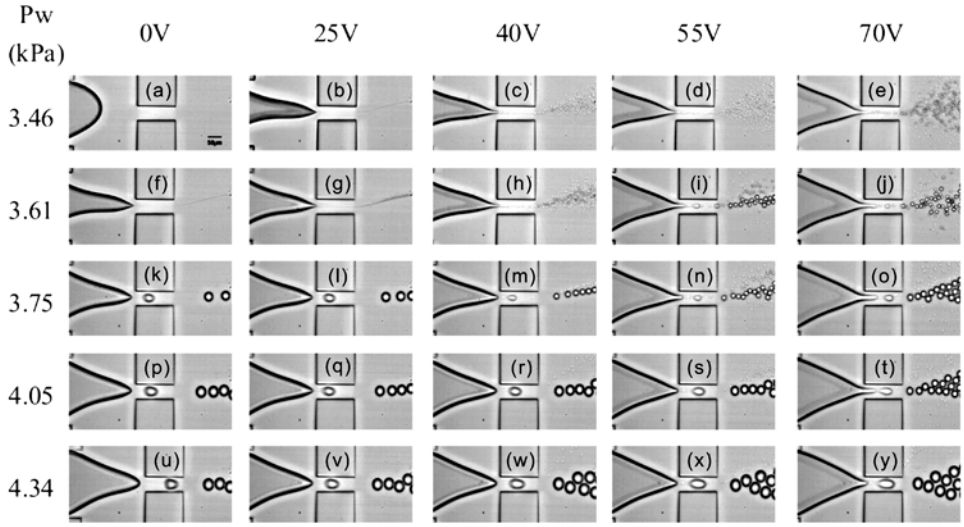

Figure 4.2 Representative images of droplet generation based on electrowetting. It depicts that droplet generation occurs at the specified value of P_w and voltage. The corresponding capillary number of the continuous phase is Ca = 0.072. (The contrast of images were increased in order to let tiny droplets become visible)

Upon increasing U further, the droplets spread out over much wider range in the outlet region, see (c) – (e) and (h). We interpret this as a sign of electrostatic repulsion and conclude therefore that the droplets in this regime must be charged. We denote this regime as "conical spray", as in the electrospraying literature.[20] Interestingly, the droplets seem to be rather monodisperse at intermediate voltage (c), (d), and (h), while bidispersity is clearly observed at higher voltage (e), (i), and (j). Upon increasing P_w further, the droplet generation mechanism switches to the

dripping regime ((k) – (y)). We find that dripping results in rather uniform primary droplets somewhat smaller than the orifice of the device accompanied by much smaller satellite droplets (see images (l) - (o), (q) - (t) and (v) – (y)). This behavior is similar to that observed by Anna *et al.*[21] in a purely hydrodynamic flow focusing system.

Here, we note another interesting aspect: at zero voltage, the tip of the water-oil interface from which the droplets and jets are emitted is located close to the centre plane of the device. Upon increasing the applied voltage, the location of this tip moves towards the bottom substrate where the electrode is located, as sketched in Fig. 4.1b and as evidenced by a shift of the focusing plane of the microscope (shown in Fig. 4.3). This shift is due to the EW-induced reduction of the contact angle θ on the bottom surface. As a consequence, the droplet generation process becomes more and more similar to the contact line instability, which is known to occur in EW at very high voltage.[19, 21]

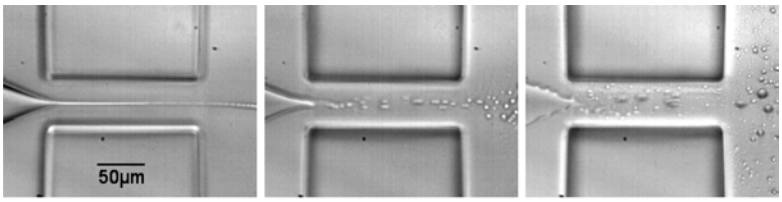

Figure 4.3 Focusing on the tip of dispersed phase. It is shown that the break-up positions are on the different planes with different voltages, if we take into account the focusing of the wall of channel. At 70 V, the tip touches the bottom surface.

In our study, when we applied higher voltages ~ 100 V and meanwhile lower P_w, we observed that droplets are ejected simultaneously from several locations along the contact line, which is one of the hallmarks of this instability (Fig. 4.4). The droplets generated in this case are very tiny, even smaller than 1 μm. The optical resolution of the microscope precludes a precise measurement of the droplet size.

In Fig. 4.5 we show a dynamic phase diagram indicating the boundaries between the various droplet generation regimes discussed above in the parameter space given by the normalized pressure P_w / P_L and the electrowetting number η (using the Laplace pressure $P_L = 2\sigma\,(1/W + 1/h)$ as a pressure scale). The negative slope of the onset curve for droplet generation with increasing η indicates the general

tendency of EW to stimulate droplet generation. This trend agrees with our observations in ref. 15 and 16, although the droplet generation mechanism is somewhat different here.

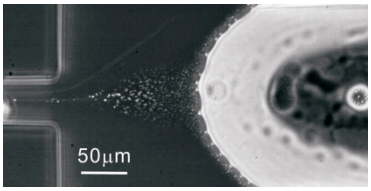

Figure 4.4 Contact line instability at 100V

At intermediate P_w, tip-streaming occurs at low η and gives way to the conical spray for higher η. The two regimes are clearly distinct from each other with a sharp onset of droplet mutual repulsion in the downstream region upon crossing the boundary. The conical spray regime seems particularly promising for producing droplets with a diameter below 10 μm. The size of these charged droplets can be smaller as small as 1 μm.

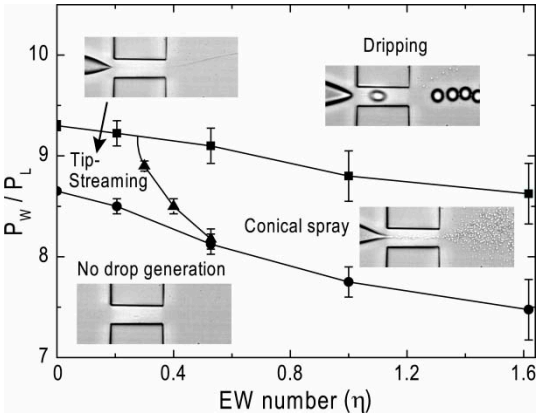

Figure 4.5 Phase diagram of droplet generation in the FFD with electrowetting as a function of normalized pressure (P_w / P_L) and electrowetting number (η). We demonstrate four regimes: no droplet generation, tip streaming, conical spray and dripping.

The dripping regime occurs when P_w is relatively high. The driving mechanism is dominated by hydrodynamic flow focusing. The droplet size is comparable to the orifice. At even higher P_w, a jet of the dispersed phase is formed, which decomposes into droplets in the outlet region following a Rayleigh-Plateau scenario (data not shown).

In Fig. 4.6 we show the droplet size and the droplet generation frequency as a function of voltage (and pressure), as obtained by quantitatively analyzing video data such as in Fig. 4.2. (Here we consider only primary droplets and ignore potential satellites.) At any voltage, the droplet size (Fig. 4.6a) increases with increasing P_w. For the lowest P_w, we indicate only estimated droplet sizes (in the range of 1 - 2 μm) in brackets since our optical system does not allow for an accurate analysis. In the conical spray regime droplet sizes of 3 - 8 μm were observed for applied voltages of 40 - 70 V. Particularly monodisperse droplets (polydispersity ~ 3%) with a diameter of 3 and 5 μm were found for 40 V ($\eta = 0.53$) or 55 V ($\eta = 1$), respectively. At high P_w in the dripping mode, the droplet size is of the same order as the orifice. The curves in Fig. 4.6a display a very interesting trend: while the typical droplet size increases with η for the tip-streaming/conical spray regime, it decreases in the dripping regime. At zero voltage, the droplet size jumps from ≈ 30 μm to ≈ 1 μm upon decreasing P_w from 3.75 kPa to 3.61 kPa. Intermediate droplet sizes are not accessible. At higher voltage, however, the droplet size varies much more continuously. Hence, EW provides the possibility to have a continuous control over the entire range of droplet sizes, in line with the results of ref.13.

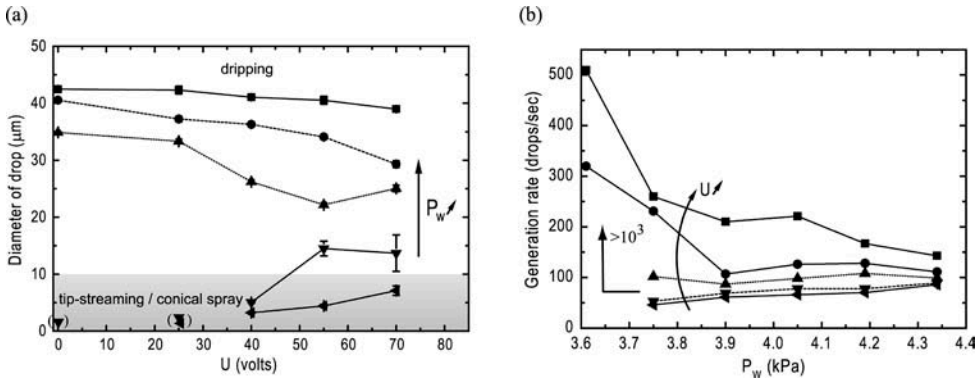

Figure 4.6 Quantitative characterizations correspond to Fig 2. (a) Droplet size evolution with an increasing electrowetting effect at different water pressure (◄ 3.46kPa, ▼ 3.61kPa, ▲ 3.75kPa, ● 4.05 kPa, ■ 4.34kPa). The values in the bracket are estimated because the droplet size is so small that it is out of the resolution of microscope/camera system. (b) Droplet generation rate versus water pressure at different applied voltages (◄ 0V, ▼ 25V, ▲ 40V, ● 55V, ■ 70V). The cornered arrow indicates the sharp increase in droplet generation rate for 0 V, 25 V and 40 V at 3.61 kPa.

Finally, we note that the droplet generation rate (Fig. 4.6b) in the dripping regime is typically of order 100 s^{-1} and globally follows a decreasing trend with increasing pressure. Only at the lowest pressure and the lowest voltages, *i.e.* in the tip streaming regime and conical spray, it increases to 10^3 – 10^4 s^{-1}. (The latter data points are not plotted because we could not analyze them quantitatively.) We find that the flow rate ratio between outer fluid and the inner fluid varies between from 10 - 100 in the case of dripping to a few thousand in the case of tip streaming and conical spray.

4.4 Conclusions

In summary, we demonstrated that the combination of microfluidic flow focusing and electrowetting yields a flexible method for microfluidic droplet generation. Compared to exclusively hydrodynamic devices, the EW-based approach offers a wide and continuous range of droplet sizes that can be tuned rapidly by varying the applied voltage in addition to the inlet pressure of the dispersed phase. Compared to other electric field based methods[4] electrowetting offers these capabilities at a much lower voltage (which could be reduced even further by using thinner dielectric layers and by patterning the EW-electrodes).

Acknowledgements

The author acknowledges MicroNed, the Microtechnology Research Programme of the Netherlands for financial support, as well as the research institutes IMPACT and MESA+ at Twente University.

References

1. S. Abraham, E. H. Jeong, T. Arakawa, S. Shoji, K. C. Kim, I. Kim and J. S. Go, *Lab Chip*, 2006, **6**, 752-756.
2. O. Skurtys and J. M. Aguilera, *Food Biophys*, 2008, **3**, 1-15.
3. A. S. Utada, E. Lorenceau, D. R. Link, P. D. Kaplan, H. A. Stone and D. A. Weitz, *Science*, 2005, **308**, 537-541.
4. H. Kim, D. Luo, D. Link, D. A. Weitz, M. Marquez and Z. Cheng, *Appl Phys Lett*, 2007, **91**, 133106.
5. N. J. Carroll, S. B. Rathod, E. Derbins, S. Mendez, D. A. Weitz and D. N. Petsev, *Langmuir*, 2008, **24**, 658-661.
6. T. Nisisako and T. Torii, *Lab Chip*, 2008, **8**, 287-293.

7. R. K. Shah, H. C. Shum, A. C. Rowat, D. Lee, J. J. Agresti, A. S. Utada, L. Chu, J. Kim, A. Fernandez-Nieves, C. J. Martinez and D. A. Weitz, *Material today*, 2008, **11**, 18-27.
8. T. Thorsen, R. W. Roberts, F. H. Arnold and S. R. Quake, *Phys Rev Lett*, 2001, **86**, 4163-4166.
9. H. Song and R. F. Ismagilov, *J Am Chem Soc*, 2003, **125**, 14613-14619.
10. S. L. Anna, N. Bontoux and H. A. Stone, *Appl Phys Lett*, 2003, **82**, 364-366.
11. S. L. Anna and H. C. Mayer, *Phys Fluids*, 2006, **18**, 121512.
12. I. Hayati, A. I. Baiey and T. F. Tadros, *Nature*, 1986, **319**, 41-43.
13. A. M. Ganan-Calvo, *Phys Rev Lett*, 2007, **98**, 134503.
14. F. Mugele and J. C. Baret, *J Phys-Condens Mat*, 2005, **17**, R705-R774.
15. F. Malloggi, S. A. Vanapalli, H. Gu, D. van den Ende and F. Mugele, *J Phys-Condens Mat*, 2007, **19**, 462101.
16. F. Malloggi, H. Gu, A. G. Banpurkar, S. A. Vanapalli and F. Mugele, *Eur Phys J E*, 2008, **26**, 91-96.
17. J. F. D. L. Mora, *J Fluid Mech*, 1992, **243**, 561-574.
18. J. C. McDonald, D. C. Duffy, J. R. Anderson, D. T. Chiu, H. K. Wu, O. J. A. Schueller and G. M. Whitesides, *Electrophoresis*, 2000, **21**, 27-40.
19. M. Vallet, M. Vallade and B. Berge, *Eur Phys J B*, 1999, **37**, 583-591.
20. J. F. D. L. Mora, *J Fluid Mech*, 1992, **243**, 561.
21. F. Mugele and S. Herminghaus, *Appl Phys Lett*, 2002, **81**, 2303-2305.

Chapter 5

A Hybrid Microfluidic Chip with Electrowetting Functionality using Ultraviolet-curable Polymer*

Abstract

Electrowetting (EW) is widely used in digital microfluidics for the manipulation of drops sandwiched between two parallel plates. In contrast, demonstrations of closed microfluidic channels enhanced with EW functionality are scarce. Here, we report a simple, low-cost method to construct such microchannels enclosed between two glass plates, each of which comprises electrodes and insulating layers. Our method uses soft imprint lithography with thiolene precursors to design the channel geometry. UV exposure is used to seal the chips permanently and a silanization treatment renders all inner channel surfaces hydrophobic. Compared to earlier polydimethylsiloxane-based designs, this method allows us to make microchannels with smaller dimensions (down to 10 microns), lower aspect ratios (down to height/length = 1/10), and symmetric electrodes both on the top and the bottom of the channel. We demonstrate the new capabilities with two examples: (i) EW-enhanced drop generation in a flow focusing geometry allows precise and continuous control on drop diameter in the range of ≈ 1 - 15 microns while maintaining monodispersity; (ii) EW allows tuning of the excess water pressure needed to displace oil in a microchannel, leading to spontaneous imbibition at EW number $\eta > 0.89$.

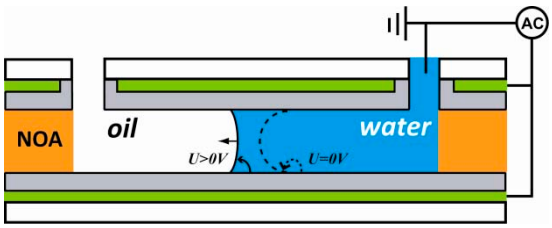

* This chapter has been published in Lab on a Chip, 2010, **10**, 1550-1556

5.1 Introduction

In the past decade, microfluidic systems have been increasingly applied to study, prepare and control two-phase fluids in various fields such as biology, medicine and food science.[1-4] Two-phase fluids in microfluidic chips also provide many possibilities in engineering, such as the controlled generation of emulsion drops serving as microreactors, controlled displacement of oil and water in micro-channels, and logic operations with both bubbles and drops.[5-7] In all these cases, interfacial tensions and wetting phenomena play a prominent role in determining the flow behavior. This is due to the small length scales addressed in micro-fluidics, which introduce large surface-to-volume ratios, as well as strongly curved (*e.g.* water-oil) interfaces which in turn cause large Laplace pressures. These circumstances make it attractive to modulate the apparent interfacial tensions[8-11] rather than to apply (high) mechanical pressure for microfluidic actuation.

One of the promising methods for modulating the apparent solid-liquid interfacial tension is ElectroWetting (EW). This technique is attractive because of the simplicity of the device architecture, ease of electronic control and low energy consumption.[11-13] EW refers to an electrically induced reduction in contact angle of a conductive liquid on top of a dielectric-coated electrode in an insulating ambient medium. At present, most applications of EW are found in digital microfluidics in an open structure, where discrete operations on individual drops are carried out on the surface of a planar plate,[14-15] or in a sandwich geometry involving two parallel plates.[16-20] In both cases, EW allows for various manipulations with individual drops such as transporting, splitting and merging. Obviously, these open structures also have their limitations: in the first place, the drop manipulation rates and thereby the throughput of such EW devices is low compared to channel-based devices, because the maximum driving forces are limited by surface tension and contact angle saturation. Moreover, air, as an ambient medium, offers little protection for the drops against evaporation or contamination.

In chapter 3 and 4, we extended the scope of EW to control two-phase flow in microchannels. To do so, we integrated insulator-covered electrodes into a flow

focusing device (FFD) leading to droplet generation with electrical control, depending on the device geometry and operation mode. For those prototype devices, microchannels were produced using soft lithography with thick slabs of PDMS and mechanically clamped onto EW surfaces consisting of ITO-glass slides covered by thin films of Teflon AF. These devices were easy to manufacture, but presented clear limitations: the softness and deformability of the PDMS allowed only for low clamping pressures, which limited both the possibilities for downscaling and the maximum flow rates. Moreover, the thickness of the PDMS slab precluded the integration of EW functionality on the top surface, which makes the device asymmetric and reduces the maximum electrical forces by a factor of two. As with other PDMS based devices there are also restrictions regarding the choice of oil due to swelling. More sophisticated approaches not suffering from these drawbacks were recently presented by Heikenfeld *et al.*[21] and Kedzierski *et al*.[22]. However, their devices were made using standard photo-lithography and wet chemical etching, which requires clean room facilities and advanced microfabrication skills.

In this chapter we present a simple, rapid and inexpensive method to fabricate closed microchannels with integrated insulator-covered electrodes (EW), which does not require cleanroom technology except for the initial fabrication of frequently reusable molds. Soft imprint lithography is applied to a liquid that is curable in ultraviolet (UV) light.[23] This approach has three advantages. First, the much higher stiffness of the final material (as compared to PDMS) allows to reduce the channel dimensions down to a few micrometers, even for rather small aspect ratios (height/width < 1/10). Second, our new approach allows to manufacture symmetric devices with EW electrodes embedded into both the top and bottom surface of the microchannel. And third, the channel material is compatible with a broad selection of oils.

To demonstrate the capabilities of the new device, we fabricate two types of microfluidic devices with integrated EW functionality: (i) an FFD involving an orifice with much smaller dimensions than in our previous PDMS-based device and (ii) a straight microchannel, in which we can measure the imbibition pressure required to replace oil with water from a reservoir at controlled inlet pressure. (For practical reasons, the latter device also contains a T-junction.)

5.2 Experimental

Our chip designs are based on the UV curable material of Norland Optical Adhesive (NOA), which has recently found applications in various other microfluidic devices.[24-26] For our specific EW application, two additional issues had to be addressed: First, the bonding between NOA and Teflon AF coated surfaces had to be ensured. We found that a tight bonding could be achieved in spite of the known chemical inertness of Teflon AF. Second, NOA surfaces are prone to show poorly controllable wetting properties: both hydrophilic[25] and oleophilic[26] behaviors have been reported, and temporal changes in these properties cannot be excluded. Such variations pose a serious obstacle for controlling two-phase flow, which can be sensitive to small changes in wettability.[27-28] To overcome this problem, we applied a surface modification inside the assembled chip, which renders the NOA surfaces permanently hydrophobic, with contact angles that are comparable to those for Teflon AF.

5.2.1 Chip design and fabrication

To implement EW in microchannels, we started with commercial indium tin oxide (ITO)-coated glass (Prazisions Glas & Optik, Germany) as a substrate. Microchannels were fabricated using NOA 81 (Norland products). The general procedure for the soft imprint lithography part was adapted from Bartolo *et al*.[25] The specific fabrication steps are shown in Fig. 5.1. First a layer of Teflon AF 1600 (Dupont, USA) with a thickness of 3.2 μm was prepared by dip-coating (Fig. 5.1a and Fig. 5.1f).[29] To promote adhesion between NOA 81 and Teflon AF[30] surfaces, the Teflon AF was pretreated with oxygen plasma for 40 s at 100 W (PDC-32G, Harrick, USA) (Fig. 5.1b). Subsequently, liquid NOA 81 was applied on Teflon AF-coated ITO glass, imprinted with the structured PDMS mold (RTV615, Bayer Silicones) and then cured by UV irradiation (UV crosslinker XL1500, Spectronics) for 38 s (Fig. 5.1c). After peeling the PDMS mold from the crosslinked NOA 81, microchannels were replicated on the bottom substrate (Fig. 5.1d). A very thin layer of NOA 81 under the PDMS stamp remained incompletely cured because PDMS facilitates the delivery of oxygen to the interface. This inhibits the free radical polymerization locally. With a properly controlled exposure time, complete curing of NOA in the boundary layer can be prevented.[31] The top surface

was created from the same type of ITO-glass. After drilling holes for the inlet and outlet connections (Fig. 5.1e), the surface was coated with Teflon AF and an oxygen plasma treatment was applied to improve bonding with the bottom part (Fig. 5.1g). Upon bringing the surfaces into contact, bonding was achieved by UV curing for 180 s of the previously mentioned thin layer of uncured NOA 81 on the bottom surface, leading to a permanently sealed microchannel (Fig. 5.1h). The last step (Fig. 5.1i) was a surface modification to make the NOA 81 channel surfaces hydrophobic (see below).

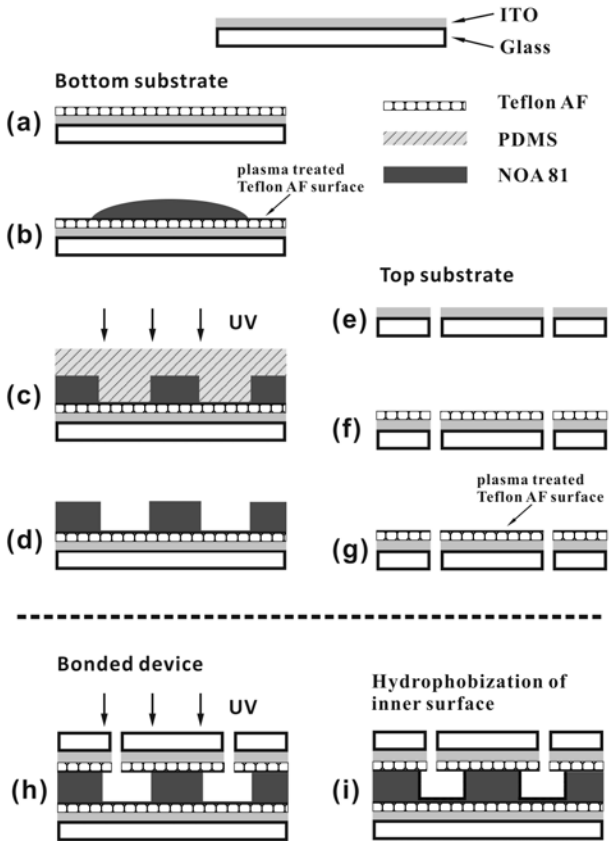

Figure 5.1 Schematic of the fabrication process of our EW-based microchannel. (a)-(d) imprinting the channel structure on a Teflon AF-coated bottom substrate; (e)-(g) drilling holes for inlet and outlet connections and then coating Teflon AF on the top substrate; (h) bonding the top and bottom substrates under UV exposure; (i) chemical modification of the inner channel.

5.2.2 Chemical surface modification

Except for the Teflon AF top surface, the inner walls of the microchannels are made of NOA 81. NOA 81 is hydrophilic (Young angle $\theta_Y < 90°$), which is not suitable for the application of EW, since a thin hydrophobic surface on the top of the dielectric layer and electrode is needed to optimize EW effect in a standard EW configuration.[32] Hence a silanization treatment was applied, making the wettability of the NOA 81 comparable to that of the Teflon AF, via the deposition of a molecular monolayer. Based on the previous procedure used for silicon surfaces,[33-35] a 1.5% (v/v) solution of 1H,1H,2H,2H-Perfluorodecyltrichlorosilane (FDTS) in isooctane was prepared under nitrogen, and pumped into the microchannel. After 15 min of incubation, excess FDTS was removed by flushing the channel with respectively isooctane and isopropanol, each for 20 min. The device was dried overnight at room temperature.

To examine the effects of the surface modification, we also coated glass slides with NOA 81 and exposed it to UV irradiation and FDTS as for the channel and measured the contact angles of aqueous drops on them using an optical contact angle goniometer (OCA-15+, Data Physics, Germany) with built-in image analysis software.

5.2.3 Electrowetting experiments

Both the (EW enhanced) drop generation and imbibition experiments are performed using an aqueous dispersed phase (W) consisting of deionized water plus NaCl (conductivity: 5-7 mS/cm) and a continuous oil phase (O) of mineral oil (Sigma Aldrich M5904, viscosity: μ_O = 0.03 Pa·s) containing 5 wt% Span 80 as surfactant. The W/O interfacial tension (σ) was measured to be 5 mN/m with a plate method using a tensiometer (Kruss, Germany). In the drop generation experiments, the flow rates Q_w and Q_o were controlled using syringe pumps (Harvard PHD 2000, Harvard Apparatus). In the imbibition experiments, hydrostatic heads were used to control the pressures P_w and P_o.

EW was applied by connecting the top and bottom electrodes to an *ac* voltage source operating at a frequency of 10 kHz, and variable root-mean-square (rms) voltages U from 0 to 100 V_{rms}. (Similar results can also be achieved for frequencies down to ≈ 100 Hz.) The aqueous phase reservoir was connected to ground. The

slope of the EW response of sessile drops on the flat surfaces prior to bonding yielded a capacitance of 5.4 μF/m², corresponding to an insulator thickness of 3.2 μm. The final chips containing the microchannels were mounted on the stage of an inverted microscope (TE 2000U, Nikon, Japan), equipped with a high-speed camera (Photron FASTCAM-Ultima 512, Japan). A 20X/air objective was used and images were captured at a frame rate of 2000 fps. ImageJ software (version 1.43n) was used to measure drop diameters.

5.3 Results and Discussion

5.3.1 Characterization of surface hydrophobicity

To examine the effects of the surface modification, contact angles were measured for aqueous drops that were surrounded by either air or oil phase, while resting on flat substrates of NOA 81 and FDTS-coated NOA 81. The results summarized in Table 5.1 show that treatment with FDTS causes a contact angle (CA) increase from 70° to 112° in air, and from 96° to 156° in oil. For comparison: the respective CA values on Teflon AF are 110° and 156°. Clearly, the FDTS coating was successful, and an identical wettability was obtained for the Teflon AF and FDTS coated walls. Moreover, the long-term stability of the FDTS layer turned out to be very good, as evidenced by the minor variations in CA that were observed after 3 and 10 days of exposure to both air and oil phase (see Table 5.1).

Treatment with silanes is a well-known method for chemical modification of silicon and glass surfaces.[36-37] In many cases the silicon or glass surfaces are pre-treated by plasma or H_2O_2 to enhance the exposure of hydroxyl (*i.e.* silanol) groups. These –OH groups then react with the Si-Cl bonds of the fluorinated organosilane molecules to form Si-O-Si (*i.e.* siloxane) bonds. What happens chemically during the surface modification of UV-cured NOA 81 is less clear. In the uncured state, NOA 81 is a mixture containing trimethylol-propane tristhiol, isophorone diisocyanate ester, trimethylol-propane diallyl ether and benzo-phenone photo initiator. After the UV-induced crosslinking reaction, the –OH groups in trimethylolpropane diallyl ether are supposed to have remained.[38-39] A possible explanation for the good stability of the silanized NOA 81 surface could be that the allyl ether –OH groups reacted with Si-Cl bonds of the FDTS.

Table 5.1 Contact angles for aqueous drops on NOA 81 surfaces with/without FDTS coating.

Contact angle	NOA 81	FDTS-coated NOA 81		
		(right after treatment)	(3 days later)	(10 days later)
In air	70° ± 1°	112° ± 2°	110° ± 1°	111° ± 2°
In oil*	96° ± 2°	156° ± 2°	155° ± 2°	155° ± 2°

*: mineral oil with 5 wt % span 80

A clear difference between the silanization of NOA 81 as compared to glass or silicon is that NOA 81 does not require any pretreatment with oxygen plasma. On the contrary, we even find that such a pre-treatment has detrimental effects for the reliability of the resulting coating. Presumably, polymer chains break down and hydroxyl groups are eliminated from the NOA 81 surface during this treatment.

5.3.2 EW-controlled drop generation

For drop generation, a flow focusing geometry is used with an overall layout as in chapter 4. In the present version, the channel height H is 10 μm. The width of the orifice is W = 20 μm and the main channels have a width W_m = 100 μm. For drops that are formed via hydrodynamic breakup in a standard FFD, the size can be controlled via the flow rates of the inner and outer fluids. This produces drops of the order of the orifice size in the squeezing and in the dripping regime, and substantially smaller drops in the jetting and tip-streaming regimes. For devices comprising one side wall with EW functionality, it is possible to tune drop size and make smaller drops, as described in chapter 4 with a minimum orifice size of $W \times H$ = 50 × 50 μm. In the current work, we demonstrate that even smaller drops can be generated in the 'conical spray' regime, with more precise control, using as parameters the flow rates and applied voltages.

In the current experiments, the flow rate of the continuous oil phase, Q_o, was kept fixed at 60 μl/h, corresponding to a capillary number $Ca = \mu_o v/\sigma$ of 0.5, where v and μ_o are the average velocity and the viscosity of the oil phase, respectively.

Drops were generated at three volumetric flow rates Q_w of the aqueous dispersed phase, corresponding to flow rate ratios of $\Phi = Q_w/Q_o$ = 1/6, 1/60 and 1/600. For each Φ, the *ac* voltage (U) was varied between 0 and 100 V_{rms}. The images shown in Fig. 5.2 clearly indicate that different regimes of drop generation are found for various combinations of U and Φ.

At the highest Φ (1/6), the generated drops are comparable to the dimensions of the orifice of the FFD (Fig. 5.2 a-f). The size distribution is monodisperse for voltages up to 40 V (Fig. 5.2 a-c) but for U > 60 V a coexistence of drops with very different sizes is found in the downstream part (Fig. 5.2 d-f). High speed video recordings reveal that coalescence events prevent the production of monodisperse drops with D < 10 μm under these operating conditions.

The second column of Fig. 5.2 shows the results for Φ = 1/60, *i.e.* a 10 times smaller Q_w. Again monodisperse drops are obtained for $U \leq$ 40 V (Fig. 5.2 g-i), but now the drops are clearly smaller due to the stronger shear forces that promote the neck formation and breakup. For U = 60 V and higher voltages the drops are again polydisperse.

Upon reducing Q_w by another decade, *i.e.* to Φ = 1/600, strings of uniform-sized drops are observed for $U \leq$ 40 V (Fig. 5.2 m-o). These drops are again smaller than the ones created at a ten times higher Q_w substantially. For U > 60 V, we now observe a conical spray, in which the drops spread out over a much wider range in the expanded downstream (Fig. 5.2 p-r). Interestingly, the tiny drops in this regime are rather monodisperse, which could be interesting for applications. This applies in particular to the case of U = 100 V, where also the generation rate of the drops is quite high (10^5 s^{-1}).

The resulting distribution of drop sizes is summarized in Fig. 5.3. It clearly indicates that at a constant *ac* frequency, the variation of Φ and U gives various ways for creating aqueous drops in the size range of ≈ 1 ~ 15 μm (diameter). At voltages up to 40 V, fairly monodisperse size distributions were found (polydispersity $\sigma_D \approx$ 1 - 4 %) in all cases, while for Φ = 1/600, σ_D was found to be ≤ 5 % even up to U = 80 V. At U = 100 V, the smallest drops appear to be smaller than 1 μm, but the size could not be more precisely measured due to limitations on the spatial resolution with the optical microscope. Knowing Q_w and (estimates

of) D, also the drop generation rate can be calculated. Especially high rates (10^4 - 10^5 s^{-1}) are found in the conical spray regime with $D < 5$ μm.

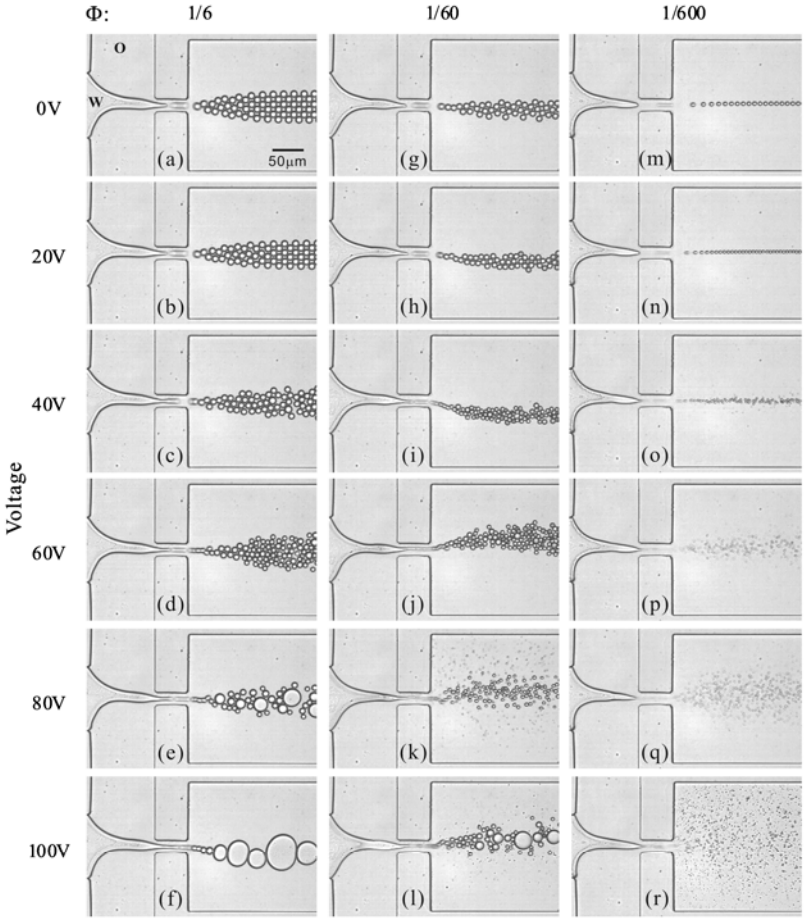

Figure 5.2 Phase diagram for drop generation in an FFD, using three different flow rate ratios Φ of dispersed aqueous phase (W) to continuous oil phase (O). EW is used for additional control over drop generation. Here the voltage is applied to both top and bottom electrodes, while the aqueous reservoir is grounded. Q_o is 60 μl/h.

What is the role of EW in the drop generation process? At low to moderate voltage (up to 40 – 60 V) the operation of the device is primarily controlled by hydrodynamic forces (pressure gradient, viscosity, interfacial tensions) and the general trends *e.g.* in drop size vs. Φ follow the observations from conventional (non-EW) microfluidic devices.[40] In this range, EW primarily changes the global

shape of the oil-water interface by reducing the water CA on the channel walls.[41-42] Thereby EW provides different 'boundary conditions' within which the hydrodynamic forces act. This leads to a rather efficient fine control over the drop sizes.

At voltages of order 60 V and higher, the role of EW become more dominant, leading amongst others to the onset of a completely different drop generation mechanism for small Φ, the conical spray formation. The wide lateral spreading of the small drops in the outlet region suggests that the drops in this conical spray regime carry electrical charge. This may be rationalized assuming that the drops are formed by a mechanism involving the electrical Maxwell stress as a primary driving force, similar to the generation of satellite drops during the instability of contact lines at high voltage in EW.[43-46]

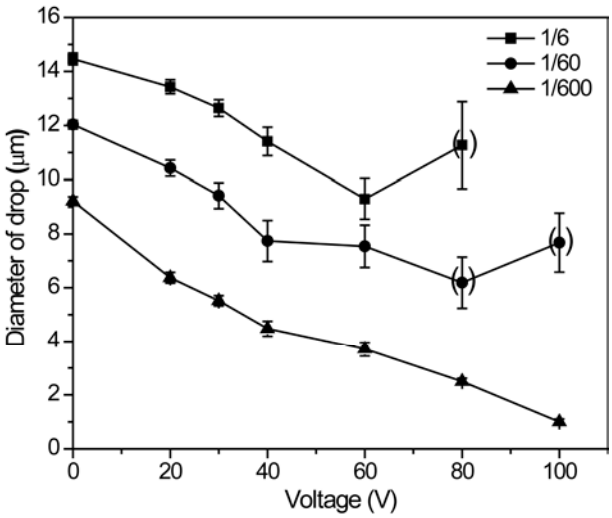

Figure 5.3 Quantitative characterization of the drop size as a function of the EW voltage and the flow rate ratio Φ. Error bars indicate the standard deviation of the size distribution. Bracketed data points indicate cases where significant polydispersity was encountered; here only the primary drops were incorporated in the analysis.

Compared to the earlier PDMS-based devices with a single electrode on one channel wall, the new approach thus offers better and more continuous control over a wider range of drop sizes. Moreover, we note that, despite the small channel thickness and constriction the devices could be easily and stably operated at total flow rates of several thousand microliters per hour, which is not possible

with comparable PDMS devices due to elastic deformation. Apart from the well-known higher stiffness of NOA 81, this observation specifically highlights the strength of the bonding achieved between Teflon AF and NOA 81.

5.3.3 EW-driven imbibition of water in a 2-D channel

In the second application of the new design, we demonstrate directly the EW-induced variation of the pressure jump across W/O interfaces. To do so, we measure the critical hydrostatic pressure P_w^* on a water inlet, the 'imbibition pressure', required to displace oil from an initially completely oil-filled channel. Here the oil pressure is controlled by another hydrostatic head at the oil inlet. For practical reasons, the microfluidic device also features an outlet channel, such that there is a continuous oil stream (see Fig. 5.4a).

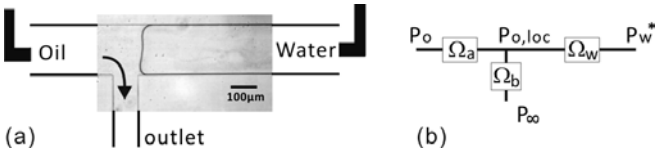

Figure 5.4 (a) Magnified view of our setup for imbibition pressure measurements. Depending on the oil and water pressures at the W/O interface, either oil or water will flow through the channel. Use of EW electrodes allows favoring wetting of the hydrophobic walls in a quantitatively controllable manner. The width of the main channel and side channel are 200 μm and 100 μm respectively. The channel height is 15 μm. (b) Hydraulic resistance circuit of the device

Similar to the experiments on the EW-controlled onset of drop generation described in chapter 3, the critical water pressure – here: for imbibition – is determined by the requirement that P_w must overcome the sum of the voltage-dependent Laplace pressure $\Delta P_L(\eta)$ of the W/O interface and local hydrostatic oil pressure $P_{o,loc}$:

$$P_w^*(\eta) = \Delta P_L(\eta) + P_{o,loc} \tag{5.1}$$

Fig. 5.5 shows the critical water pressure for a series of different oil pressures as a function of the applied voltage, which is expressed as the non-dimensional electrowetting number $\eta = CU^2/(2\sigma)$. (The electrowetting number expresses the electrical force per unit length pulling on the contact line in units of the W/O

interfacial tension σ.[11]) Two trends are immediately observed: i) P_w^* decreases linearly with η and ii) $P_{o,loc}$ increases (linearly) with the oil inlet pressure P_o.

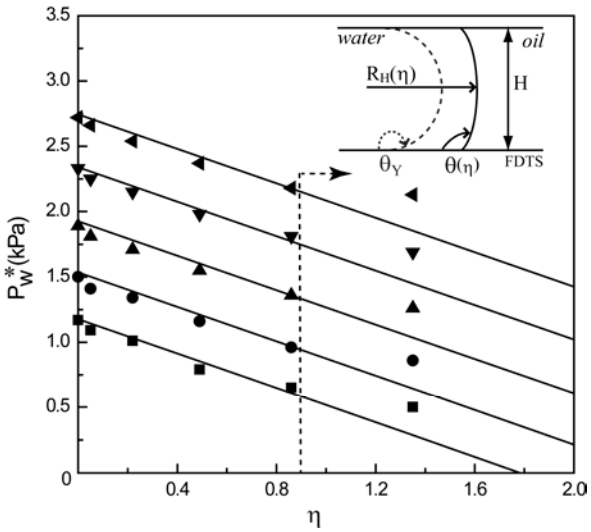

Figure 5.5 Imbibition of the critical water pressure required for displacing the W/O interface, as a function of EW number (η) for different oil pressures (■: 1.47 kPa, ●: 2.45 kPa, ▲: 3.43 kPa, ▼: 4.41 kPa, ◄: 5.39 kPa). The vertical dashed line indicates the critical EW number (*i.e.* voltage), beyond which ΔP_L is negative. Inset: cross-sectional sketch of the W/O interface inside the channel.

This voltage-dependence of P_w^* can be understood by considering the Laplace pressure of the W/O interface. It can be written as $\Delta P_L(\eta) \approx \sigma\,(1/R_W + 1/R_H)$, where R_W and R_H are the radii of curvature along the width and height of the channel, respectively. While R_W is constant, R_H varies with the contact angle $\theta = \theta(\eta)$ of the aqueous phase as $R_H = -H/(2\cos\theta(\eta))$ (see inset of Fig. 5.5). (This expression is simpler than the corresponding one in ref.47 because the contact angle is the same on both surfaces and decreases in a symmetric way rather than only on one surface.) $\theta(\eta)$ is given by the EW equation $\cos\theta(\eta) = \cos\theta_Y + \eta$, as usual. This leads to the following expression for the voltage-dependent Laplace pressure:

$$\Delta P_L(\eta) = -\frac{2\sigma}{H}\eta - \frac{2\sigma}{H}\cos\theta_Y + \frac{2\sigma}{W} \qquad (5.2)$$

in agreement with the linear decrease shown in Fig. 5.5. The slope of the solid

lines in Fig. 5.5 is thus given by $-2\sigma/H$ = -0.66 kPa, as determined from independent measurements. The dashed vertical line indicates the critical EW number $\eta^* = 0.89$, at which ΔP_L of the W/O interface is zero. For all larger voltages, the W/O interface has a negative mean curvature. (The data points for the highest voltage in Fig. 5.5 lie above this linear slope because contact angle saturation limits the contact angle reduction at high voltage (for a recent review on contact angle saturation, see ref.48).

The relative vertical offset of the curves in Fig. 5.5 is due to the variation of $P_{o,loc}$ in Eq. 5.1 with increasing oil inlet pressure. In analogy with Ohm's law, we find $P_{o,loc} = \Omega_b/(\Omega_a+\Omega_b)\cdot P_o = \lambda P_o$, where Ω_a and Ω_b are the hydraulic resistances of the oil channel before and after the junction, respectively (see Fig. 5.4b). Ω is related to the dimensions of the various channel segments by $\Omega \approx 12\mu_o L/WH^3$, where L is the length of the channel segment. (For the present geometry, we calculate $\lambda = 0.43$ in excellent agreement with the experimental result $\lambda = 0.41 \pm 0.01$ obtained from the vertical offset of the solid lines in Fig. 5.5.)

These results illustrate several advantages compared to our earlier approach using PDMS-based devices: (i) due to the enhanced stiffness of NOA 81 compared to PDMS, it is possible to produce not only overall smaller microchannels but also microchannels with a very small aspect ratio. In this case, the influence of the side walls on the mean curvature of the W/O interface is reduced, leading to a wider tunability of the pressure. Moreover, the flow geometry is almost two-dimensional. (ii) For the PDMS-devices, the contact angle on the top surface remains constant at a rather large value of ≈ 160°. As a consequence, ΔP_L is always positive, even at the highest accessible values of η. With the present symmetric device, this limitation can be overcome and truly negative mean curvatures of the W/O interface can be achieved. As a consequence, these symmetric devices allow sucking water into an initially oil-filled microchannel from a larger reservoir at zero pressure. This may be useful for the loading of microfluidic chips, which usually requires sealing micropipettes to inject liquid at an overpressure.

5.4 Conclusions

In summary, we developed a simple and inexpensive fabrication technique for

microfluidic chips, which combine the functionalities of channel flow and EW. The imprinting lithography based on NOA 81 offers the opportunity to build devices with micron size features. Reliable hydrophobization of the NOA 81 surface is achieved using a silanization treatment. The new chip design allows for a more precise and continuous control over the formation of monodisperse small drops with diameters from 1 to 15 μm in flow focusing devices. Moreover, it allows for controlling the pressure (and thus the actuation force) in the aqueous phase over a much wider range (including negative Laplace pressures) than asymmetric devices. Amongst other aspects, this enables spontaneous filling (imbibition) of water into microchannels from macroscopic reservoirs at zero pressure.

Acknowledgements

The author thanks Patrick Tabeling and Philippe Nghe for their hospitality and support in learning the microfluidic sticker technology, and also acknowledges MicroNed for financial support, as well as the research institutes IMPACT and MESA+ at Twente University.

References

1. H. A. Stone, A. D. Stroock and A. Ajdari, *Annu Rev Fluid Mech*, 2004, **36**, 381-411.
2. H. Song, D. L. Chen and R. F. Ismagilov, *Angew Chem Int Edit*, 2006, **45**, 7336-7356.
3. G. M. Whitesides, *Nature*, 2006, **442**, 368-373.
4. R. B. Fair, A. Khlystov, T. D. Tailor, V. Ivanov, R. D. Evans, P. B. Griffin, V. Srinivasan, V. K. Pamula, M. G. Pollack and J. Zhou, *Ieee Des Test Comput*, 2007, **24**, 10-24.
5. M. J. Fuerstman, P. Garstecki and G. M. Whitesides, *Science*, 2007, **315**, 828-832.
6. M. Prakash and N. Gershenfeld, *Science*, 2007, **315**, 832-835.
7. M. Schindler and A. Ajdari, *Phys Rev Lett*, 2008, **100**, 044501.
8. T. S. Sammarco and M. A. Burns, *Aiche J*, 1999, **45**, 350-366.
9. A. A. Darhuber and S. M. Troian, *Annu Rev Fluid Mech*, 2005, **37**, 425-455.
10. R. B. Fair, *Microfluid Nanofluid*, 2007, **3**, 245-281.
11. F. Mugele and J. C. Baret, *J Phys-Condens Mat*, 2005, **17**, R705-R774.
12. C. Quilliet and B. Berge, *Curr Opin Colloid In*, 2001, **6**, 34-39.
13. M. G. Pollack, A. D. Shenderov and R. B. Fair, *Lab Chip*, 2002, **2**, 96-101.
14. C. G. Cooney, C. Y. Chen, M. R. Emerling, A. Nadim and J. D. Sterling, *Microfluid Nanofluid*, 2006, **2**, 435-446.
15. S. Berry, J. Kedzierski and B. Abedian, *J Colloid Interf Sci*, 2006, **303**, 517-524.
16. J. Lee and C. J. Kim, *J Microelectromech S*, 2000, **9**, 171-180.
17. S. K. Fan, P. W. Huang, T. T. Wang and Y. H. Peng, *Lab Chip*, 2008, **8**, 1325-1331.

18. J. Gong and C. J. Kim, *Lab Chip*, 2008, **8**, 898-906.
19. M. J. Jebrail and A. R. Wheeler, *Anal Chem*, 2009, **81**, 330-335.
20. D. Brassard, L. Malic, F. Normandin, M. Tabrizian and T. Veres, *Lab Chip*, 2008, **8**, 1342-1349.
21. J. Heikenfeld, K. Zhou, E. Kreit, B. Raj, S. Yang, B. Sun, A. Milarcik, L. Clapp and R. Schwartz, *Nat Photonics*, 2009, **3**, 292-296.
22. J. Kedzierski, S. Berry and B. Abedian, *J Microelectromech S*, 2009, **18**, 845-851.
23. Y. N. Xia and G. M. Whitesides, *Annu Rev Mater Sci*, 1998, **28**, 153-184.
24. Z. T. Cygan, J. T. Cabral, K. L. Beers and E. J. Amis, *Langmuir*, 2005, **21**, 3629-3634.
25. D. Bartolo, G. Degre, P. Nghe and V. Studer, *Lab Chip*, 2008, **8**, 274-279.
26. L. H. Hung, R. Lin and A. P. Lee, *Lab Chip*, 2008, **8**, 983-987.
27. B. Zhao, J. S. Moore and D. J. Beebe, *Science*, 2001, **291**, 1023-1026.
28. W. Li, Z. H. Nie, H. Zhang, C. Paquet, M. Seo, P. Garstecki and E. Kumacheva, *Langmuir*, 2007, **23**, 8010-8014.
29. E. Seyrat and R. A. Hayes, *J Appl Phys*, 2001, **90**, 1383-1386.
30. Scheirs, *J. Modern Fluoropolymer*, John Wiley & Sons, Ltd., New York, 1997.
31. J. P. Rolland, E. C. Hagberg, G. M. Denison, K. R. Carter and J. M. De Simone, *Angew Chem Int Edit*, 2004, **43**, 5796-5799.
32. A. Quinn, R. Sedev and J. Ralston, *J Phys Chem B*, 2005, **109**, 6268-6275.
33. K. Handique, D. T. Burke, C. H. Mastrangelo and M. A. Burns, *Anal Chem*, 2000, **72**, 4100-4109.
34. B. J. Adzima and S. S. Velankar, *J Micromech Microeng*, 2006, **16**, 1504-1510.
35. L. L. Shui, A. van den Berg and J. C. T. Eijkel, *Lab Chip*, 2009, **9**, 795-801.
36. J. Sagiv, *J Am Chem Soc*, 1980, **102**, 92-98.
37. A. del Campo and I. J. Bruce, *Top Curr Chem*, 2005, **260**, 77-111.
38. B. S. Chiou, R. J. English and S. A. Khan, *Macromolecules*, 1996, **29**, 5368-5374.
39. X. Q. Gong, W. J. Wen and P. Sheng, *Langmuir*, 2009, **25**, 7072-7077.
40. P. Garstecki, H. A. Stone and G. M. Whitesides, *Phys Rev Lett*, 2005, **94**, 164501.
41. J. Buehrle, S. Herminghaus and F. Mugele, *Phys Rev Lett*, 2003, **91**, 086101.
42. *NOTE: If the channel thickness H approach the insulator thickness d, additional aspects may become relevant: Since the electrical stresses in EW are distributed over a region of order d, the additional distortions of the oil-water interface arise (rather than a simple reduction of the contact angle) that will affect the drop generation. see 44. For the current device with d=3.2μm and H=10μm, it is currently not clear to what extent these effects already matter.*
43. M. Vallet, M. Vallade and B. Berge, *Eur Phys J B*, 1999, **11**, 583-591.
44. F. Mugele and S. Herminghaus, *Appl Phys Lett*, 2002, **81**, 2303-2305.
45. *NOTE: Since the capacitance between the small drops to be formed and the electrodes on the substrate is small, it is natural that the drops aquire some charges during the breakup process that they do not dischardge. see 48*.
46. J. C. Baret and F. Mugele, *Phys Rev Lett*, 2006, **96**, 016106.
47. F. Malloggi, S. A. Vanapalli, H. Gu, D. van den Ende and F. Mugele, *J Phys-Condens Mat*, 2007, **19**, 462101.
48. F. Mugele, *Soft Matter*, 2009, **5**, 3377-3384.

Chapter 6

A Microfluidic Platform for On-Demand Formation and Merging of Droplets using Electric Control*

Abstract

We demonstrate a microfluidic system in which (programmable) local electric fields originating from embedded and protected electrodes are used to control the formation and merging of droplets in a microchannel. The creation of droplets on demand (DOD) is implemented using the principle of electrowetting. Combined with hydrodynamic control, the droplet size and formation frequency can be varied independently. Using two synchronized DOD injectors, merging on demand (MOD) is achieved via electrocoalescence. The efficiency of MOD is 98 % based on hundreds of observations. These two functionalities can be activated independently.

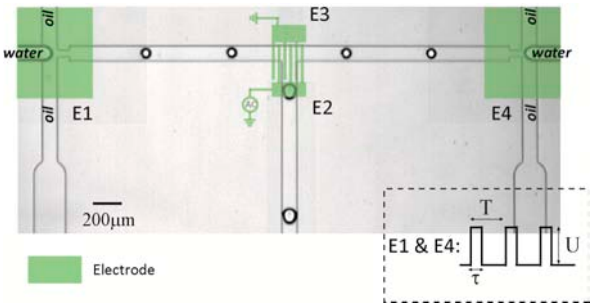

* This chapter has been published in *Biomicrofluidics*, in press

6.1 Introduction

Droplet-based microfluidics have found an increasing number of applications in the past decade, in areas like biomedical diagnostics, drug screening, and chemical synthesis on chip.[1-4] This technology offers several advantages like sample volume reduction, fast reaction and analysis, low energy consumption and increased automation. Current trends are that microfluidic chips are becoming more multifunctional and more dedicated to specific operations. The recent developments of drop on-demand (DOD) and merging on-demand (MOD) functionalities connect very well to this trend. DOD is needed in applications where either the number of drops needs to be controlled, or where different droplet manipulations need to be synchronized to each other. MOD can either facilitate 2D matrix screening tests, or applications where the decision to merge (or not) depends on a prior diagnosis of the droplet contents. In this case, the presence of the two candidate droplets at the same time and place as required by MOD could be facilitated by DOD.

One prominent research area where DOD and MOD have strong potential, is the on-chip screening of biological cells that have been encapsulated in droplets. Here the cells may be rare and/or the reagents costly, making it necessary to generate (and merge) droplets only when needed. Alternatively the number of cells may also be very large, while only a few are of interest. In this case, a high throughput screening is needed in which each droplet is first analyzed for a cellular response, and then given a fate (as in ref. 5). One way to determine this fate is to merge it with another drop (or not).

Two different platforms are available for achieving DOD or MOD. In so-called digital microfluidics (DMF), all droplet manipulations are carried out as discrete steps by switching individually addressable electrodes. Since droplet creation, transport and merging essentially involve the same operation (activating a local electrode), the DMF platform is very well suited for both DOD and MOD. However for applications that require high throughput or involve downstream operations that are incompatible with DMF, continuous flow microfluidics is preferred. In that case, DOD and MOD require the integration of active elements with the layout of the flow channels.

In this chapter we consider DOD and MOD in continuous flow geometries. Different ways of realizing DOD have been reported. Lin and Su[6] and Zeng *et al.*[7] described a system using pneumatic microvalves fabricated in polydimethylsiloxane (PDMS), while Churski *et al.*[8] used external valves interconnected with a microchip. Alternatively, also electric signals can be used to create droplets on demand. As demonstrated in chapter 3, electrowetting (EW) is used to increase the wettability of the channel wall at the location of drop formation. With both the mechanical and electrical methods, a certain control over droplet volume (V) and/or generation rate (k) could be achieved. However there is still lack of an efficient on-demand platform to produce droplets using electric control.

The merging of droplets in a flow channel geometry has been widely studied for passive methods,[9-11] which do not require intervention and always result in fusion. In contrast, MOD has been studied only a few times. Link *et al.* reported that droplets can be merged by applying *dc* voltages with opposite sign across the two droplets during their formation.[12] Priest *et al.*[13] and Wang *et al.*[14] demonstrated MOD applications based on electrocoalescence (EC) using *dc* or *ac* voltages. However each method required a precise droplet synchronization and precise electrode alignment. A different EC-based MOD method was reported by Zagnoni and Cooper.[15-17] They used a pattern of electrodes to hold a single droplet at the channel surface until the second one arrived. This worked successfully after a careful tuning of the flow strength. However in these EC applications where electrodes were in direct contact with the fluid, the occurrence of electrochemical reactions seems hard to exclude. This could be disadvantageous especially in bioanalytical applications where, depending on the biological content, redox reactions could occur.

While the results of these initial studies are certainly promising, it is also clear that the demand for new DOD/MOD systems is expected to remain for some time. First of all, the diversity of potential applications is rather large; which means that certain types of implementation (electric, mechanical) will go well with certain types of microfluidic chip. And secondly, also aspects like the ease of manufacturing or the robustness of the device will drive the development of new designs.

In this chapter we present a DOD & MOD device that is easy to manufacture, requiring merely a patterning of electrodes, dip-coating and soft lithography. DOD and MOD electrodes are integrated in the same layer and can be activated independently. The footprint is small, which facilitates parallelization of multiple DOD injectors and MOD mergers, thus allowing also more complex operations (*e.g.* multiple mixing or dilution steps). Since our chip contains no moving parts, and its electrode surfaces are protected against electrolysis by an insulator layer, it has the potency to become a robust chip.

6.2 Experimental

As shown in Fig. 6.1, our system is based on the combination of microchannels and insulator-covered electrodes. The channels are fabricated in PDMS using single-layer soft lithography by replicating from SU8 (photoresist) mold. Electrodes are obtained by depositing indium tin oxide (ITO) on a glass substrate, and etching part of the ITO away with 18% HCl via the standard wet etching method.[18] Then the patterned ITO-glass is covered by a (d =) 3.2 μm thick Teflon AF insulator layer via dip-coating.[19] The chip is assembled by clamping the PDMS structure onto the Teflon covered substrate. The channel geometry for droplet generation is flow-focusing device (FFD). The dimensions are a channel height of 50 μm, and a width of 100 μm for the main channel and 50 μm for the orifice. The chip is mounted on the stage of an inverted microscope (TE 2000U, Nikon, Japan), equipped with a high speed camera (Photron FASTCAM SA3, Japan).

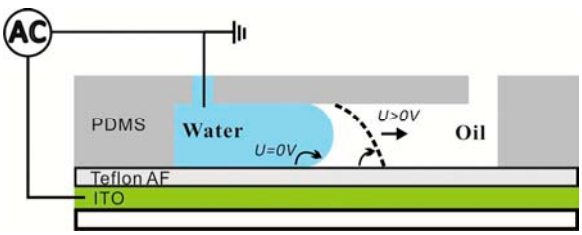

Figure 6.1 Schematic side-view illustration of EW-based FFD. When a voltage is applied, the water-oil interface is pulled to the downstream.

Our dispersed phase (W) consists of deionized water plus NaCl (conductivity: 5 mS/cm), while our continuous phase (O) is mineral oil plus 3 wt% (nonionic) Span 80 surfactant. The inlet pressures P_W and P_O can be tuned using hydrostatic

heads, and are kept at 4.8 and 7.5 kPa respectively. Electric fields are applied by connecting ITO electrodes to *ac* voltage sources (10 kHz), while the aqueous phase reservoir is connected to ground.

6.3 Results and Discussion

Droplet on Demand capabilities are first explored using continuous *ac* voltage. Results are shown in Fig. 6.2 a and b. Below a root-mean-square voltage (U_{rms}) of ≈ 30 V, no droplets are formed. Increasing U_{rms} up to 70 V, the droplet formation frequency k grows from 1.5 to 10 Hz (voltages in excess of 70 V lead to contact line instabilities and polydisperse droplets). Remarkably, the droplet diameter (D) remains fairly constant at ≈ 50 μm. This trend differs from the purely hydrodynamic case, where D and formation rate change simultaneously.[20] It suggests that our electrically induced droplet formation offers separate control over the two quantities. In this scheme D could be tuned by varying hydrodynamic condition P_W and P_O as demonstrated in chapter 3.

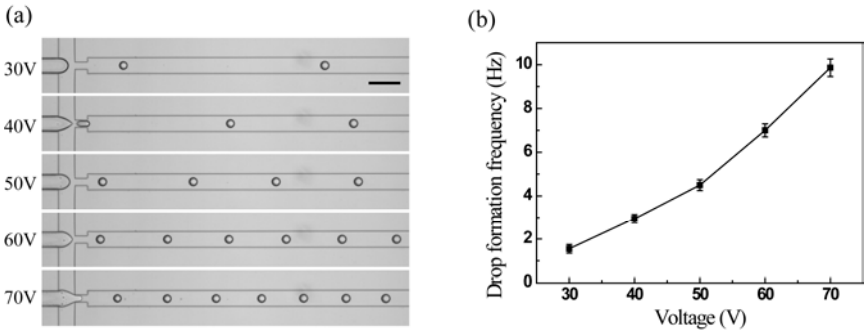

Figure 6.2 (a) Drop formation occurs only above a threshold voltage. Increasing U_{rms} further, the drop formation frequency (k) increases while the drop size remains constant. The scale bar is 200 μm. (b) k as a function of U_{rms}.

Building on these results, we also explore another DOD mode by fixing U_{rms} at 55 V and using a programmable voltage source to create pulses of width τ and periodicity T. As shown in Fig. 6.3, it is possible to create individual droplets (on demand) by choosing $\tau \approx 120$ ms. The minimum waiting time that allows formation of a similar droplet is $T = 125$ ms, indicating that any arbitrary pulse sequence with intervals longer than this time will generate a correspondingly

timed droplet sequence. The smaller τ and T should be obtainable by increasing the hydrostatic pressures.

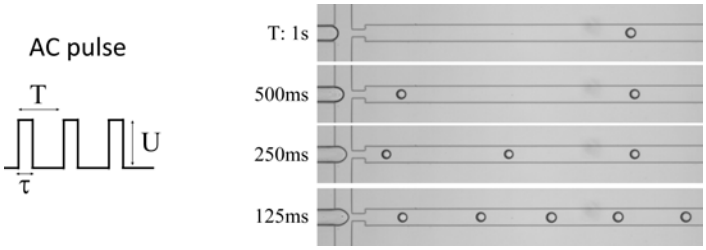

Figure 6.3 Control over drop formation frequency at fixed U_{rms} by using *ac* pulses with variable intervals. The scale bar is 200 μm.

Mechanistically, the DOD control can be attributed to electrowetting[21] (EW). Applying a voltage U_{rms} over the insulator layer causes the wetting angle θ of the aqueous phase to decrease according to EW equation $\cos\theta = \cos\theta_Y + \eta$, with θ_Y the Young's angle, and $\eta = CU^2/(2\sigma)$ the EW number.[21] The increased water wettability of the substrate facilitates the formation (and subsequent breakup) of a liquid neck. For the current device with capacitance C = 3.3 μF/m^2, and interfacial tension σ = 5 mN/m, the electric stress and surface tension are equal (*i.e.* η = 1) for $U \approx 55$ V. Clearly, the EW principle allows to adjust the voltage accordingly for droplets with a different σ.

Merging-on-demand is implemented on the same chip, using interdigitated electrodes (IDE) at a T-junction where the droplets from two DOD injectors meet (see Fig. 6.4). The IDE stripes have a width of 10 μm and a pitch of 20 μm. To avoid the risk of electrolysis (and possibly also fouling by (bio)molecules inside the droplets), we prefer to use isolated electrodes. Since Teflon AF is already used as an insulator for the EW assisted droplet formation, we can simply make use of the same layer to make MOD more reliable. Challenges in the realization of this method are i) the two droplets should arrive simultaneously, and ii) the local electric fields at the IDE should be strong enough to destabilize the droplet pair.

Due to the symmetric design, synchronization is simply obtained by applying the same voltage signal to the DOD electrodes E1 and E4. In applications involving asymmetry in the travel time to the junction, compensation could be made by activating E1 and E4 with an appropriate delay time. Merging of droplets is

achieved by loading the IDE (E2 and E3 in Fig. 6.4a) with an appropriate (rms) voltage difference ΔU_{rms}. For $\Delta U_{rms} < 20$ V, the electric forces that drive fusion are not strong enough to overcome the resistance of the stabilizing surfactant layers, whereas for $\Delta U_{rms} >> 70$ V electric breakdown of the insulating Teflon layer occurs. One snapshot of two droplets produced simultaneously from opposing FFDs is shown in Fig. 6.4b.

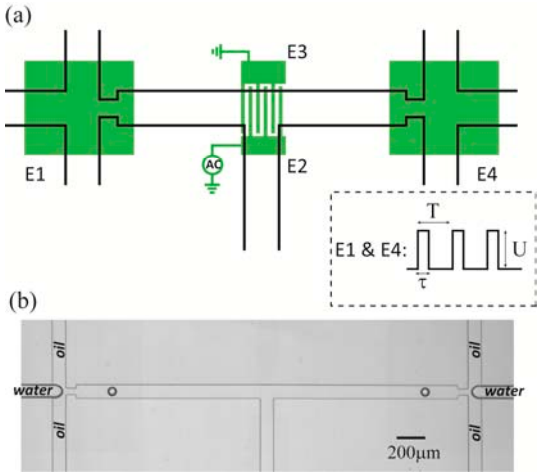

Figure 6.4 (a) Schematic of the microfluidic platform for DOD and MOD. Electrodes E1 and E4 are used for triggering drop formation, using *ac* pulses. The IDEs (E2 and E3) are used for merging of droplets. (b) Two droplets are produced simultaneously by switching E1 and E4 at same time.

If the IDE is switched off, the two droplets do not merge even though they squeeze each other at T junction (see Fig. 6.5 a-f). This is due to the surfactant stabilization. When merging is chosen, switching on the voltage (*i.e.* 40 V in the case of Fig. 6.5 g-l) destabilizes the surfaces of droplets, resulting in merging.

To further examine the mechanism of this MOD, we capture images of the critical moments of droplet merging, using a high speed camera with a frame rate of 10K fps. We analyze MOD for two devices with the IDE mounted in different orientations relative to the T-junction (see Fig. 6.6). In Fig. 6.6a, two droplets initially approach and touch each other. However instead of merging, the droplet pair rotates and moves downstream. Then after an initial increase in separation, suddenly coalescence occurs. The orientation angle at which this happens shows slight variability; this is ascribed to small differences in the arrival time of the two

droplets at the junction, which affect the subsequent hydrodynamics of the tumbling and approaching droplets. Alternatively in Fig. 6.6b, droplets coming from opposite directions touch each other and merge immediately. For both geometries, the qualitative scenarios are highly reproducible and merging occurs with ≈ 98% efficiency (based on hundreds of observations). Interestingly, this indicates that even without a very precisely alignment between IDE and channels, merging should occur with ≈ 98% efficiency when the voltage is switched on.

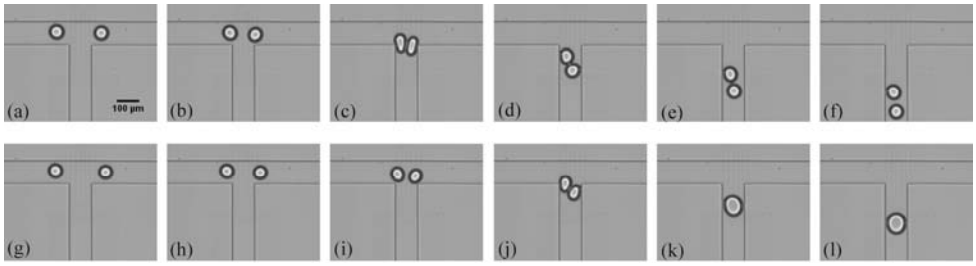

Figure 6.5 Sequential images (a) - (f) E2 and E3 are switched off. The droplets meet at the junction and move to downstream without merging; (g) - (l) E2 and E3 are switched on. Two droplets merge at the junction.

The merging in our MOD device occurs essentially via ElectroCoalescence[22] (contributions due to EW and DEP can be rationalized to be weak). In EC, the electric stress $\sigma_E \sim \varepsilon_c \varepsilon_0 E^2$ competes with the capillary pressure $p_c \sim \gamma/R$.[23] σ_E tends to deform (and ultimately disintegrate) the droplet whereas p_c tends to minimize the interface at constant mean curvature. Significant advances have been made in the understanding of EC.[13, 24-26] However the mechanistic aspects of EC are not yet completely understood, even for simple configurations of electrodes and droplets. In our device the situation is more complex, since the electric field due to the IDE is non-uniform at length scales smaller than the droplet diameter. Locally induced droplet deformations are then expected to play a role. This is also suggested by the coalescence events in Fig. 6.6, which appear to have a preferred alignment with the electrode stripes. In EC, it is generally the case that the surfactant layers become unstable once the most nearby surfaces of the two droplets have reached a minimum distance. The role of the external electric field is then to enhance the dynamics of approach and to enlarge the critical distance. This should also apply in our case.

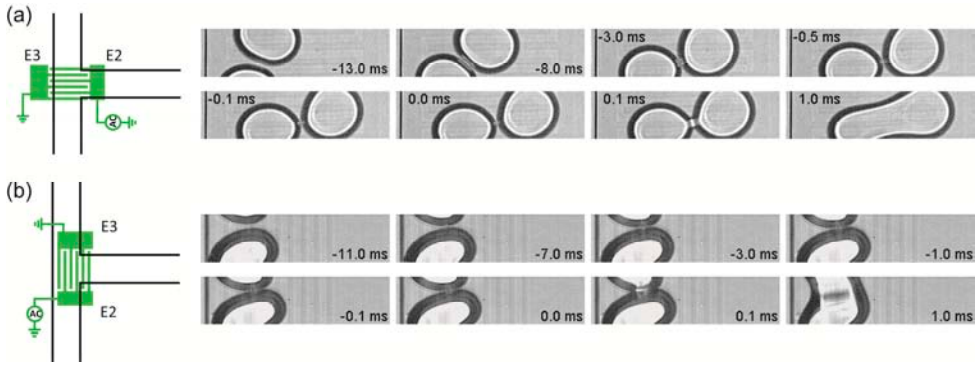

Figure 6.6 Sequential images recorded at 10k fps showing how two droplets merge for different orientations of the IDE stripes. In (a), prior to merging, two droplets contact each other and then rotate till the contact line and electrode stripes have an angle close to 90°. In (b), two droplets merge immediately upon contact. Also in this case the contact line has an angle close to 90° with the electrode stripes.

From an application perspective, the physics of electrocoalescence (*i.e.* the dependence on E, γ, R) implies that our MOD device can also be made to perform reliably under different conditions (*e.g.* droplet size, interfacial tension) by an up- or downscaling of the geometry or simply by adjusting the voltage.

6.4 Conclusions

In conclusion, we demonstrated a microfluidic platform that implements voltage programmable on-demand droplet formation and on-demand droplet merging. DOD is based on electrowetting while MOD involves electrocoalescence. Our device is easy to fabricate, since the number of steps is small and alignment of the IDE is not critical. The device can be operated at relatively low voltages, and shows robustness under these conditions. The droplet throughput rate is comparable to other devices. This platform offers a way of miniaturized automated microfluidic chip for screening in various areas of chemistry and biochemistry.

Acknowledgements

The author acknowledges the MicroNed programme, part of the Decree on subsidies for investments in the knowledge infrastructure (Bsik) from Dutch

government for financial support, as well as the research institutes IMPACT and MESA+ at Twente University.

References

1. H. A. Stone, A. D. Stroock and A. Ajdari, *Annu Rev Fluid Mech*, 2004, **36**, 381-411.
2. H. Song, D. L. Chen and R. F. Ismagilov, *Angew Chem Int Edit*, 2006, **45**, 7336-7356.
3. Y. C. Tan, K. Hettiarachchi, M. Siu and Y. P. Pan, *J Am Chem Soc*, 2006, **128**, 5656-5658.
4. S. Y. Teh, R. Lin, L. H. Hung and A. P. Lee, *Lab Chip*, 2008, **8**, 198-220.
5. M. Y. He, J. S. Edgar, G. D. M. Jeffries, R. M. Lorenz, J. P. Shelby and D. T. Chiu, *Anal Chem*, 2005, **77**, 1539-1544.
6. B. C. Lin and Y. C. Su, *J Micromech Microeng*, 2008, **18**, 115005.
7. S. J. Zeng, B. W. Li, X. O. Su, J. H. Qin and B. C. Lin, *Lab Chip*, 2009, **9**, 1340-1343.
8. K. Churski, P. Korczyk and P. Garstecki, *Lab Chip*, 2010, **10**, 816-818.
9. H. Song, J. D. Tice and R. F. Ismagilov, *Angew Chem Int Edit*, 2003, **42**, 768-772.
10. L. Mazutis, J. C. Baret and A. D. Griffiths, *Lab Chip*, 2009, **9**, 2665-2672.
11. X. Niu, S. Gulati, J. B. Edel and A. J. deMello, *Lab Chip*, 2008, **8**, 1837-1841.
12. D. R. Link, E. Grasland-Mongrain, A. Duri, F. Sarrazin, Z. D. Cheng, G. Cristobal, M. Marquez and D. A. Weitz, *Angew Chem Int Edit*, 2006, **45**, 2556-2560.
13. C. Priest, S. Herminghaus and R. Seemann, *Appl Phys Lett*, 2006, **89**, 134101.
14. W. Wang, C. Yang and C. M. Li, *Small*, 2009, **5**, 1149-1152.
15. M. Zagnoni, C. N. Baroud and J. M. Cooper, *Phys Rev E*, 2009, **80**, 046303.
16. M. Zagnoni and J. M. Cooper, *Lab Chip*, 2009, **9**, 2652-2658.
17. M. Zagnoni, G. Le Lain and J. M. Cooper, *Langmuir*, 2010, **26**, 14443-14449.
18. http://www.betelco.com/sb/phd/ch5/c52.html.
19. E. Seyrat and R. A. Hayes, *J Appl Phys*, 2001, **90**, 1383-1386.
20. P. Garstecki, H. A. Stone and G. M. Whitesides, *Phys Rev Lett*, 2005, **94**, 164501.
21. F. Mugele and J. C. Baret, *Journal of Physics-Condensed Matter*, 2005, **17**, R705-R774.
22. M. Chabert, K. D. Dorfman and J. L. Viovy, *Electrophoresis*, 2005, **26**, 3706-3715.
23. A. R. Thiam, N. Bremond and J. Bibette, *Phys Rev Lett*, 2009, **102**, 188304.
24. D. H. Michael and M. E. Oneill, *J Fluid Mech*, 1970, **41**, 571-&.
25. S. Herminghaus, *Phys Rev Lett*, 1999, **83**, 2359-2361.
26. X. Z. Niu, F. Gielen, A. J. deMello and J. B. Edel, *Anal Chem*, 2009, **81**, 7321-7325.

Chapter 7

Interfacial Tension Measurements with Microfluidic Tapered Channels

Abstract

We developed a microfluidic chip that is capable of measuring interfacial tensions between two liquids, directly from a force balance. This functionality is obtained by using a tapered microchannel, which offers a range of possible interface curvatures. The position along the channel where mechanical equilibrium is reached, depends on the interfacial tension, the contact angles with the channel walls, and externally controllable pressures. Using a device of PDMS with a channel height of 50 μm and a width tapering from 300 to 20 μm, equilibrium interfacial tensions (IFTs) could be measured for various systems with / without surfactant, having IFTs between 3 and 38 mN/m. Quantitative agreement with macroscopic measurements was obtained, albeit that in the absence of surfactant, the location of the receding interface was influenced by additional pinning forces. We demonstrate the utility of our device for measuring IFTs that change over time, due to a slow adsorption at the interface. Our device should be especially suitable for studying the formation of interfacial layers for different compositions of the continuous phase.

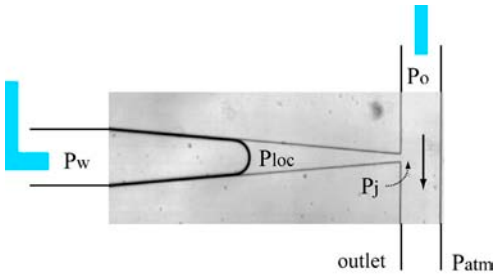

7.1 Introduction

It is well-known that the interfacial tension (IFT) is an important physical property for governing the structure, dynamics and stability of multiphase systems in various scientific and industrial applications, like emulsification, pharmaceuticals, cosmetics and food, the (enhanced) recovery of oil, and so forth.[1-4] Conventional methods for measuring IFT are Wilhelmy plate, Du Noüy ring, sessile drop and pendant drop.[5] These methods offer convenience, accuracy and suitability for liquid/liquid or liquid/gas interfaces. However they also need a spotless environment to prevent exposure to contaminants, since these species generally have a tendency to end up at interfaces. Also the scale of the measurement requires a relatively large amount of sample.

In the past decade, there has been growing interest in microscale measurements of IFTs. For example, Lee *et al*. reported a micropipette technique, in which the IFT is determined from the radius of curvature of the interface in the pipette for a given pipette pressure.[6-7] While this method does not suffer from the limitations mentioned above, the measurements are not easily performed. One liquid, with an interface formed in a micropipette, needs to be exposed rapidly to a solution of another liquid in order to minimize contamination.

Perhaps the strongest potential for measuring IFTs at the microscale lies in the use of microfluidic devices. This would connect very well to the increased use of such devices for emulsification-related processes, and moreover it would provide the information where it matters the most: *in situ*. One of the first microfluidic methods was developed by Hudson *et al.*,[8-9] who obtained IFTs from a precise analysis of the shape distortion of suspended droplets. To induce the droplet deformations, they used a flow field gradient that was generated by constrictions in the microchannel. This method has the advantages of high speed, low sample consumption and good repeatability. One inconvenient aspect is that measuring dynamic (*i.e.* time dependent) IFT requires multiple constriction points which means a relatively large microfluidic device.

Other researchers have studied so-called apparent dynamic IFTs in relation to (kinetics of) surfactant adsorption in emulsions. Using T-junction,[10-11] Y-junction[12] or coaxial geometries[13] the IFT of produced droplets could be inferred from the

size and generation rate of the droplets. The measurement of such transient IFTs is very important for tuning emulsification processes.

Despite the achievements of the recently presented methods of microfluidic (*i.e.* on-chip) tensiometry, there is still much to be desired. For example, also interfaces where water and oil meet without forming droplets are interesting: which phase will wet the channel wall(s), and how to modify this by external forces are very relevant questions for applications ranging from the filling of microchannels, to water imbibition in oil recovery. In particular surfactant ad- or desorption, leading to changes in interfacial tension are important aspects. To study these phenomena *in situ*, a tensiometric method based on (quasi) static interfaces would be needed. However, such a method is missing at present.

In this chapter, we will present a "first generation" microfluidic device for measuring the IFT between two (quasi-) stationary liquids. Key element of the design is a tapered channel leading to a T-junction. The varying width of the channel provides the fluid interface with a degree of freedom, as to where to settle. The axial location where this occurs is determined by the applied pressure difference, the wetting angles at the walls and the IFT. Then by controlling the first two, the latter can be measured.

In this work we will consider the geometric design aspects, and assess to what extent our new technique is able to reproduce IFTs as measured with traditional (macroscopic) measurements. Besides measurements of equilibrium IFTs, also the case of a time-dependent IFT will be addressed. Finally, we will also explore the possibilities obtained after extending the device with electrowetting (EW) functionality.[14]

7.2 Experimental

7.2.1 Materials

The oil phase (O) is a mineral oil (Sigma Aldrich, viscosity: μ_O = 0.03 Pa·s), while milli-Q water was used for the aqueous phase (W). Sodium chloride (NaCl) was added to the aqueous phase up to a conductivity of 5-7 mS/cm, to allow for EW applications. For the purpose of varying interfacial tension, two non-ionic surfactants were used (one at the time). Triton X-100 (Acros) with 0.5 wt%

concentration was prepared in an aqueous phase. Span 80 (Fluka) with 1 wt% and 0.5 wt% concentrations were applied in an oil phase. The concentrations of Triton X-100 and Span 80 are much higher than their critical micelle concentrations (CMCs).[15-16] Equilibrium O/W IFTs were measured with a tensiometer (Kruss K11, Germany) using a Wilhelmy plate, and were found to be: 38 mN/m without surfactants, 3.1 mN/m with Triton X-100 and 5 mN/m with Span 80.

7.2.2 Experimental Setup

Our device consists of a microchannel mounted on a glass slide. The glass was coated with an indium-tin oxide (ITO) conductor plus a Teflon AF 1600 insulator with a thickness of 3.2 μm prepared by dip-coating.[17] The channel was fabricated in polydimethylsiloxane (PDMS) using standard soft lithography.[18] The molded PDMS channel was clamped mechanically onto the glass substrate. Fig. 7.1 illustrates the geometry which includes a tapered channel and T-junction. The inlet pressures of oil (P_O) and water (P_W) were controlled using hydrostatic heads with a precision of 1 Pa (≡ 0.1 mm).

The microfluidic chip was placed on an inverted microscope (TE 2000U, Nikon, Japan), equipped with a 10X/air objective and a high-speed camera (FASTCAM SA3, Photron, Japan). ImageJ software (version 1.43n) was used to measure the position of the W/O interfaces from recorded images. When applying EW, the bottom ITO electrode was connected to a voltage source to apply an *ac* voltage U (0 … 100V_{rms} (root mean square)) with a frequency of 10 kHz, while the aqueous phase reservoir was connected to ground.

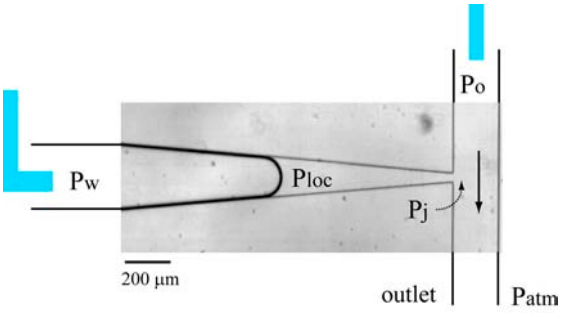

Figure 7.1 Schematic of our setup. The W/O interface is formed in the tapered channel. The pressures at different locations are indicated for further discussions.

7.2.3 Methodology for IFT measurement

Our method is based on the Young-Laplace equation (Eq. 7.1), where R_w and R_h are the radii of curvature in the horizontal and vertical planes (corresponding to the channel width w and height h respectively). P_L is the Laplace pressure difference across the W/O interface. By measuring the curvature and calculating P_L from the inlet water and oil pressures, the IFT can be obtained from Eq. 7.1.

$$P_L = \sigma \cdot (\frac{1}{R_w} + \frac{1}{R_h}) \tag{7.1}$$

First we consider the calculation of the curvature of the interface. In our tapered geometry, R_h is constant while R_w can be adjusted to meet the imposed pressure boundary conditions. $R_w \approx -w/2\cos\theta$, where θ is the contact angle between interface and channel walls while w is the (variable) channel width. R_h is determined in a similar way as $R_h \approx -h/2\cos\theta$ as shown in Fig. 7.2a. Taking into account that in our case $\cos\theta$ is practically the same for all surfaces, Eq. 7.1 can in good approximation be rewritten as:

$$P_L = \sigma \cdot (-2\cos\theta) \cdot (\frac{1}{w} + \frac{1}{h}) \tag{7.2}$$

The pressure difference across the interface P_L is equal to $P_W - P_{loc}$, where P_{loc} is the local oil pressure near the interface (see Fig. 7.1). In the absence of flow between the interface and the T-junction, P_{loc} should be equal to the pressure at the junction P_j. The latter pressure is determined by the reservoir pressure P_0 and the pressure drop due to the flowing oil. Considering the equivalent hydrodynamic circuit of the microchannel system and applying Ohm's law, we find that P_j is given by:

$$P_j = \frac{\Omega_b}{\Omega_a + \Omega_b} \cdot P_O = \lambda \cdot P_O \tag{7.3}$$

where $\Omega \approx \mu L/wh^3$ is the fluidic resistance, with μ the oil viscosity, L the length of the channel segment (a or b, see Fig. 7.2.) and w and h as before. Eq. 7.3 has been confirmed for several channel geometries and liquid combinations in previous studies.[19-20]

Substituting Eq. 7.3 in Eq. 7.2 then results in:

$$P_L = P_W - \lambda \cdot P_O = \sigma \cdot (-2\cos\theta) \cdot (\frac{1}{w} + \frac{1}{h}) \quad (7.4)$$

which shows that given P_O, P_W, h and θ, σ follows from the measurement of w.

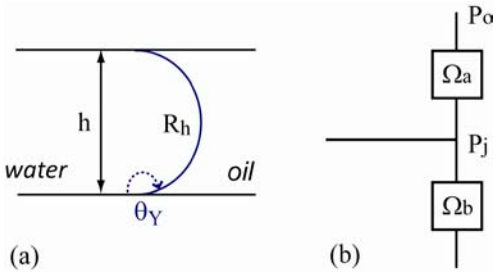

Figure 7.2 (a) Cross-sectional sketch of the W/O interface inside the channel; (b) Hydrodynamic circuit of the device for oil phase.

To allow measurement of σ in the typical range of 5 - 50 mN/m using (hydrostatically controlled) Laplace pressures in the range of 1 - 1000 Pa, the dimensions of the tapered channel had to be tuned carefully. The length of the tapered section should be long enough to allow an accurate measurement of the width at which the W/O interface touches the sidewalls. On the other hand, the channel should be short enough to fit in the field of view of the microscope (10X). A length of 1500 μm fitted these requirements. The height of all channels was chosen the same, being 50 μm.

As shown by Eq. 7.4, the Laplace pressure is dominated by the smallest of w and h. For this reason the largest w (at x = 1500 μm) was set at 300 μm, while the smallest w (at x = 0) was designed to be 20 μm. Given these dimensions, $1/h+1/w$ varies between (~ 0.023) and (~ 0.071) μm^{-1}. We remark here that w < 20 μm might also have given problems due to possible deformations of the PDMS channel. This means that for the current device, the relation between w and x is given by:

$$w = 0.187x + 20 \quad (7.5)$$

with w and x in μm. Inserting this result in Eq. 7.4 gives an explicit dependence of the Laplace pressure on the axial position x. This dependence is illustrated for two representative cases in Fig. 7.3a.

An inherent aspect of our design is that the equilibrium (w-) position of the W/O interface depends not only on the IFT but also on the chosen P_w and P_o (as a

consequence, in different experiments the same σ will correspond to a different w, since P_w and P_o cannot be set with very high precision). To allow measuring IFTs that change (slowly) over time, both the initial and the (expected) final IFT should correspond to a width w that lies within the boundaries of 20 and 300 μm. This condition is generally met if the highest IFT corresponds to a w that is found at $x \approx$ 1200 μm. To illustrate how this works, we show in Fig. 7.3b the relation between σ and x for a W/O interface that has an initial σ of 50 mN/m corresponding to an initial x of 1200 μm. As σ decreases (*e.g.* due to slow surfactant adsorption), x also becomes smaller. For σ smaller than 12 mN/m, no equilibrium x-position can be found anymore and the aqueous phase will enter the oil-filled channel. This means that a dynamic range (in σ) of about 4 can be accommodated by the device. IFTs below 12 mN/m could still be measured, but this would require adaptation of the hydrostatic pressures.

Finally we consider the straight channel. This has a width of 200 μm, and is intersected by the tapered channel halfway, so in Eq. 7.4., λ is equal to 0.5.

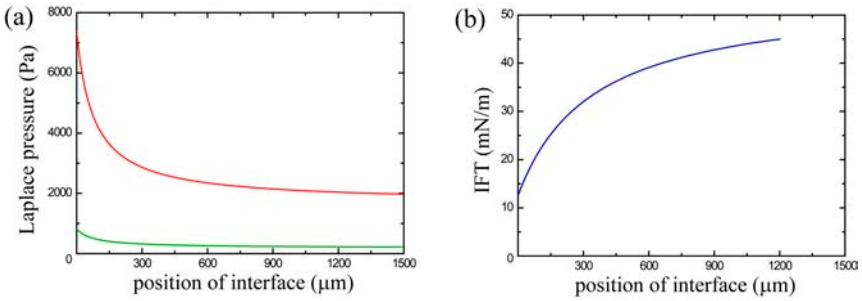

Figure 7.3 Theoretical performance of or device. (a) Laplace pressure as a function of x at a constant IFT (red: 50 mN/m, green: 5 mN/m); (b) Interfacial tension versus the position of the interface (x) in a tapered channel, where $x = 0$ indicates the position of the T-junction at a constant Laplace pressure. The height of the channel is 50 μm.

7.3 Results and Discussion

7.3.1 Static interfacial tension

We first used the setup to measure the IFT between milli-Q water and mineral oil without surfactant. As demonstrated in Fig. 7.4a, the location of the W/O interface in the tapered channel responds to an increase of the water pressure P_w while the contact angle appears to remain the same. This suggests indeed the occurrence of

equilibrium according to Eq. 7.1.

To examine the correspondence quantitatively, we increased the water pressure in steps, and measured the corresponding widths of the channel where the W/O interface settled. Also the contact angle θ (157° ± 3°) was measured from a series of images. Then inserting all the known into Eq. 7.4, we extracted the value of σ. Fig. 7.4b shows the result as a plot of P_L *vs.* -2cosθ·(1/w+1/h). Values of the IFT can be obtained from individual points as well as from a linear fit to the data set. From the latter we found an IFT of 37.2 ± 1.2 mN/m, which is in good agreement with the value of 38 mN/m measured with the Wilhelmy plate. Also the individual data points were close to this value: 36 ± 2.0 mN/m. Hence not only the slope but also the offset of the line are in good agreement with the model. This also indicates that the error in calculated pressure difference is small.

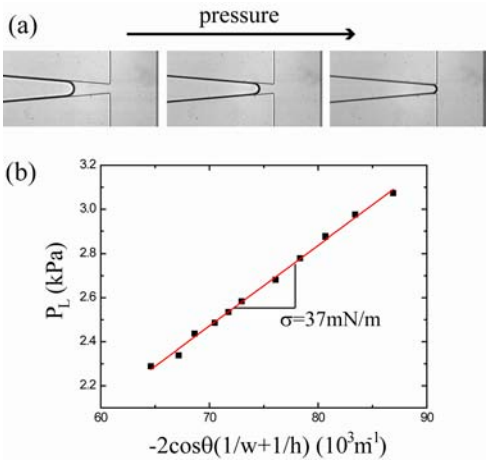

Figure 7.4 (a) Displacement of the W/O interface towards the junction upon increasing P_W; (b) Plot of the applied P_L versus the measured interface curvature. The IFT is determined from the slope based on Eq. 7.4.

However, upon progressively decreasing the water pressure, the location of the interface did not respond in the same reliable manner as for the advancing contact angle. These points at the occurrence of pinning forces, which lower the contact angle to an extent that depends on the local heterogeneities of the wall(s). Due to this behavior, the IFT could not be obtained in a reliable way from the slope of P_L *vs.* -2cosθ·(1/w+1/h).

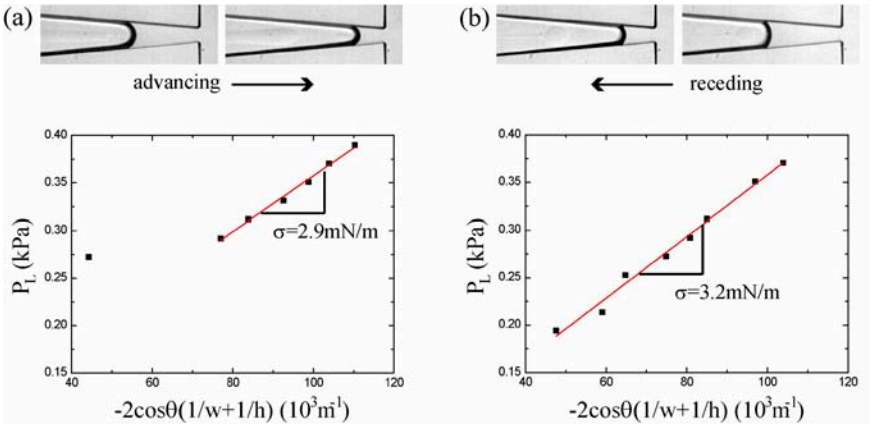

Figure 7.5 IFT of (water+Triton X-100) and mineral oil: (a) P_L versus curvature for advancing contact angles; (b) same but now for receding contact angles. The IFTs are determined from the slope based on Eq. 7.4.

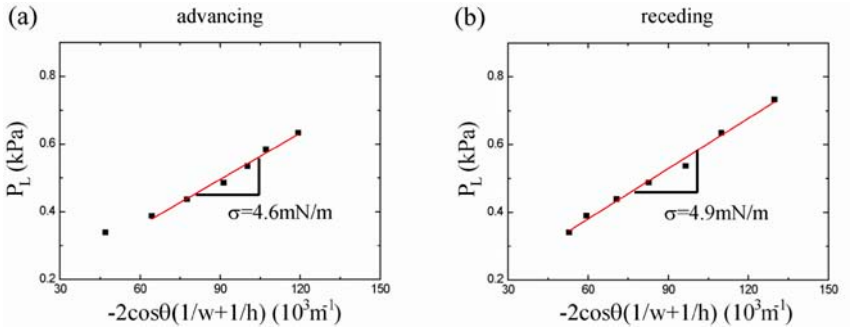

Figure 7.6 IFT of water and (mineral oil + 1 wt% Span 80): (a) P_L versus curvature for advancing contact angles; (b) same but now for receding contact angles. The IFTs are determined from the slope based on Eq. 7.4.

In the presence of the used surfactants, the IFT could be measured by either increasing or decreasing the water pressure. However the observed contact angles in the two directions still showed some differences (see Table 7.1). These findings are also illustrated in Fig. 7.5 and Fig. 7.6. For 0.5 wt% Triton X-100 in aqueous phase, we obtained IFTs of 2.9 and 3.2 ± 0.1 mN/m from the advancing and receding curves. Both results compare well to the 3.1 mN/m measured with the plate method. For 1 wt% Span 80 in oil, we obtained IFTs of 4.6 and 4.9 ± 0.2 mN/m for the advancing and receding cases. Also for these rather low IFTs a good agreement was found with the macroscopic measurement of 5.0 mN/m.

7.3.2 Time-dependent interfacial tension

One aspect that makes our device especially interesting is that it might be capable of monitoring gradual changes in IFT *in situ* while working with fluids on-chip. Such a monitoring could serve either as a quality control, or as a means to systematically study the effect of compositional variations in the phase (here: oil) that flows past the T-junction. To explore this capability, we did an experiment in which the interface was initially formed from pure water and oil, but subsequently the oil was replaced by a solution of Span 80. This was realized by connecting two reservoirs with the different oil phases via a Y-junction valve to the inlet tubing for oil. Care was taken to ensure that the liquid levels (*i.e.* the hydrostatic heads) were precisely the same for both reservoirs. Closing the stream of pure oil and allowing the Span 80 solution to flow, then results in a gradual change of the surfactant concentration at the W/O interface: due to the low oil flow rate and the large length of the inlet tubing, the transport of Span 80 through the tubing occurs via a combination of convective displacement and diffusion. As a result, the IFT should show a gradual decrease. While in this case the time-dependence of σ would merely reflect the kinetics of convection and diffusion, it can be a model for slow adsorption processes of a different nature.[21]

The outcome of this experiment is shown in Fig. 7.7. Replacing the pure oil with a 0.5 wt% Span 80 solution, the axial position (x) of the W/O interface and hence the calculated interfacial tension starts to decrease from the moment that the first surfactant molecules arrive. While the initial IFT of 37.5 ± 1.1 mN/m is in good agreement with the presence of pure oil, the value of 18.5 ± 0.8 mN/m as reached after ~ 3×10^3 s does not correspond to the earlier observed equilibrium value of ~ 5 mN/m. This suggests that the Span 80 concentration near the interface has not yet reached the CMC. This is certainly conceivable: the average convective displacement of the fluid (~ 0.4 m) in the tubing during the (~ 1 h) course of the experiment was calculated to be less than the (~ 1 m) length of the tubing. This indicates that the oil phase that was flowing past the T-junction of the device, was still in the transition zone between pure oil and the oil with 0.5 wt% Span 80.

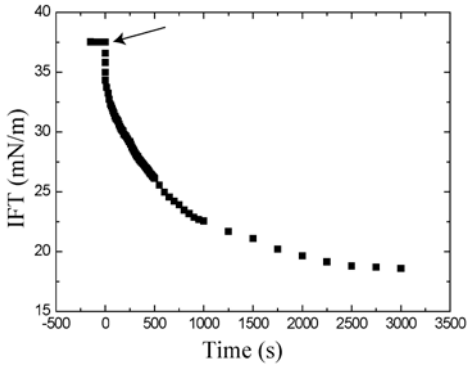

Figure 7.7 Dynamic IFT measurement: the adsorption of Span 80 at the W/O interface is tracked by changes in the IFT. The arrow indicates the starting point of adsorption.

7.3.3 Contact angle hysteresis

As mentioned previously and as illustrated in Fig. 7.5, the advancing contact angles were generally larger than the receding angles. This contact angle hysteresis (CAH) finds its microscopic origin in surface roughness and/or chemical heterogeneities, which give rise to so-called pinning forces. To quantify the effect, advancing and receding angles were measured from the images, in a similar way as in a contact angle goniometer. The results shown in Table 7.1 indicate that while CAH occurs in all systems, the effect is much weaker in the presence of surfactant (in case of Span 80, the difference between advancing and receding angles is even less than 10°). Also the spread between the contact angles measured in the same regime (*i.e.* advancing or receding) appears to be smaller in the presence of surfactant (we attribute the mentioned irregular displacements of the receding contact line in the absence of surfactant to these variations).

Table 7.1 Contact angles hysteresis for aqueous phase moving in a channel filled with an oil phase in the cases of with/without surfactants

Contact angle	Advancing angle	Receding angle
no surfactant	157° ± 3°	118° ± 5°
Triton X-100	155° ± 2°	138° ± 3°
Span 80	158° ± 3°	149° ± 2°

Finally we note also that the advancing contact angle is practically the same for all

three cases. This facilitated the analysis of the dynamic experiment shown in Fig. 7.7, since there was no need to measure also θ as a function of time. $\cos\theta$ could just be inserted as a constant in Eq. 7.4.

To explore the practical implications hereof somewhat further, we analyzed the measurements in the presence of Span 80 also for the receding case, thereby inserting the mean receding contact angle into Eq. 7.4. This produces a curve that can be compared to that of the advancing case. The data in Fig. 7.8 indicate that the Laplace pressures (that are proportional to the IFT) correspond to each other within ~15%.

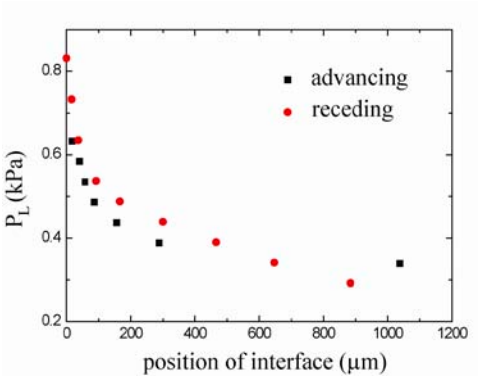

Figure 7.8 P_L versus the position of the interface in a tapered channel for the advancing and receding cases. This measurement was done in a water / (mineral oil + Span 80) system.

7.3.4 Electrowetting and tapered channel

We also explored to what extent the capabilities of our device could be enhanced using EW as an extra functionality. The fabrication of this extension is fairly easy, since it requires little more than the placement of an electrode plus insulator underneath the tapered channel. Then the contact angle at the electrically actuated surface can be modified according to the EW equation [14] (Fig. 7.9a):

$$\cos\theta(\eta) = \cos\theta_Y + \eta \qquad (7.6)$$

Here $\eta = CU^2/2\sigma$ is the dimensionless EW number which indicates the relative strength of electrostatic and interfacial tension forces, while C is the capacitance of the dielectric layer. Variation of the voltage U (or equivalently η) can then be used to change the mean curvature of the interface and hence the Laplace pressure.

Activating the electrode from a starting point in which mechanical equilibrium (in Eq. 7.4) is already attained, should then lead to displacement of the interface.

In Fig. 7.9b we show the results of our exploratory experiment in the presence of surfactant (1 wt% Span 80). For $\eta > 0.2$ ($U > 25$ V) the (x-position of the) interface was observed to respond instantaneously to a change in voltage; moving closer to the T-junction (at $x = 0$) when the voltage was increased, and moving further away upon decreasing U. However, the advancing and receding curves clearly did not overlap (except at $\eta \approx 1$). Remarkably, after switching off the voltage, the interface did move back to its original position (from which the experiment was started). This suggests that an additional electric effect must play a role too.

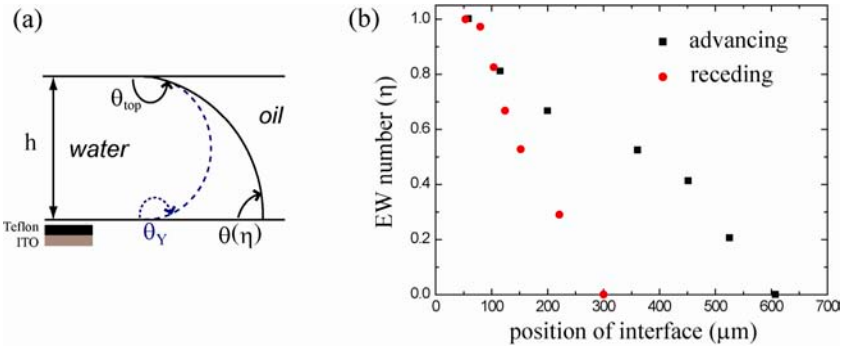

Figure 7.9 (a) Cross-sectional sketch of the W/O interface inside the channel. The contact angle alters when the voltage is applied. (b) EW number versus position of interface. The interface moves towards the junction with increasing voltage (black squares), and withdraws with decreasing voltage (red circles).

7.4 Conclusions and Outlook

In summary, we demonstrated a "first generation" device that is capable of measuring interfacial tensions reliably and in a straightforward way, using a microfluidic tapered channel. Several equilibrium IFTs in the range of ~ 3 to 38 mN/m could be measured. The results are in very good agreement with values obtained using a Wilhelmy plate. Also an example of the measurement of a time dependent IFT was given. Finally also electrowetting was explored as means to enhance the capabilities of the device. Here it was possible to actuate the liquid, but also an unexpected hysteresis effect was found.

The work presented in this chapter is only the first study. The reliability of the device could be further enhanced if the contact angle hysteresis could be further reduced.

Acknowledgements

The author acknowledges MicroNed, the Microtechnology Research Programme of the Netherlands for financial support, as well as the research institutes IMPACT and MESA+ at Twente University.

References

1. H. A. Stone, A. D. Stroock and A. Ajdari, *Annu Rev Fluid Mech*, 2004, **36**, 381-411.
2. H. Song, D. L. Chen and R. F. Ismagilov, *Angew Chem Int Edit*, 2006, **45**, 7336-7356.
3. R. B. Fair, *Microfluid Nanofluid*, 2007, **3**, 245-281.
4. S. Y. Teh, R. Lin, L. H. Hung and A. P. Lee, *Lab Chip*, 2008, **8**, 198-220.
5. J. Lyklema, *Fundamentals of Interface and Colloid Science, Vol. III: Liquid fluid interfaces; Academic Press*, San Diego, 2000.
6. S. Lee, D. H. Kim and D. Needham, *Langmuir*, 2001, **17**, 5537-5543.
7. S. Lee, D. H. Kim and D. Needham, *Langmuir*, 2001, **17**, 5544-5550.
8. S. D. Hudson, J. T. Cabral, W. J. Goodrum, K. L. Beers and E. J. Amis, *Appl Phys Lett*, 2005, **87**, -.
9. J. T. Cabral and S. D. Hudson, *Lab Chip*, 2006, **6**, 427-436.
10. N. T. Nguyen, S. Lassemono, F. A. Chollet and C. Yang, *Iee Proc-Nanobiotech*, 2006, **153**, 102-106.
11. K. Wang, Y. C. Lu, J. H. Xu and G. S. Luo, *Langmuir*, 2009, **25**, 2153-2158.
12. M. L. J. Steegmans, A. Warmerdam, K. G. P. H. Schroen and R. M. Boom, *Langmuir*, 2009, **25**, 9751-9758.
13. J. H. Xu, S. W. Li, W. J. Lan and G. S. Luo, *Langmuir*, 2008, **24**, 11287-11292.
14. F. Mugele and J. C. Baret, *J Phys-Condens Mat*, 2005, **17**, R705-R774.
15. S. C. Goheen and R. S. Matson, *J Am Oil Chem Soc*, 1989, **66**, 994-997.
16. L. Peltonen, J. Hirvonen and J. Yliruusi, *J Colloid Interf Sci*, 2001, **240**, 272-276.
17. E. Seyrat and R. A. Hayes, *J Appl Phys*, 2001, **90**, 1383-1386.
18. D. C. Duffy, J. C. McDonald, O. J. A. Schueller and G. M. Whitesides, *Anal Chem*, 1998, **70**, 4974-4984.
19. F. Malloggi, S. A. Vanapalli, H. Gu, D. van den Ende and F. Mugele, *J Phys-Condens Mat*, 2007, **19**, 462101.
20. H. Gu, M. H. G. Duits and F. Mugele, *Lab Chip*, 2010, **10**, 1550-1556.
21. O. Brandal, J. Sjoblom and G. Oye, *J Disper Sci Technol*, 2004, **25**, 367-374.

Chapter 8

Summary and Outlook

Electrowetting (EW)-based digital microfluidic systems (DMF) and droplet-based two-phase flow microfluidic systems (TPF) with closed channels are the most widely used microfluidic platforms. In general, these two approaches have been considered independently. However, integrating the two technologies into one allows to combine the advantages of both worlds: (i) high throughput (from TPF) and (ii) precise control over each individual drop (from EW). Thus the aim of this thesis was to investigate the combination of EW technology and the droplet-based TPF platform. Hence we designed and developed several of such hybrid microfluidic chips, using different approaches and microfabrication technologies. We demonstrated the new functionalities of the developed devices and explored the physics ingredients based on our observations.

In **Chapter 2** we give an overview of the state of the art in EW and digital microfluidics. We introduce the principle of EW, and the main physical aspects like the conductivity of aqueous phase, contact angle saturation and hysteresis, and contact line motion. Each of these aspects is relevant for the application of microfluidics. EW-based DMF is also presented in terms of its operations, consisting of droplet formation, transportation, splitting, merging and mixing. In the second part of this chapter, we review the most recent developments in droplet-based TPF, especially focusing on two practical aspects: droplet formation and droplet merging under both hydrodynamic and electric control conditions. Furthermore, several common microfabrication methods for TPF are also discussed.

We chose to study the droplet formation in a flow focusing device (FFD) because such devices allow for a very reproducible formation of monodisperse droplets. In **Chapter 3**, we report our first FFD device having a polydimethylsiloxane (PDMS) channel structure, bonded onto a Teflon AF-coated indium tin oxide (ITO) glass

substrate. Based on the experimental observations, an operating diagram of water droplet formation as a function of the water and oil pressures and the applied (EW) voltage was obtained. In a specific region of the diagram, the formation of droplets occurs only upon EW actuation. The conditions under which this enhanced control over the droplet formation is obtained, are in quantitative agreement with a theoretical model that compares the electrostatic stress generated with EW to the local hydrostatic pressures at the orifice. In this regime, the droplet size and droplet generation frequency are independently controllable via the amplitude and the width of voltage pulses. Furthermore, we also report similar droplet formation phenomena in the presence of surfactants.

A different capacity of EW in droplet formation (for emulsification related applications) is presented in **Chapter 4**. In this study a downscaled channel with a much smaller orifice (width (w) × height (h): 50 × 50 μm) was utilized. In addition to either the pressures or the flow rates of the dispersed (water) and continuous (oil) phases, the EW voltage was used as a third control parameter for droplet formation. Compared to exclusively hydrodynamic devices, the EW-based devices were found to offer a wider and more continuous range for the size of droplets that can be formed. Of particular interest was a regime in which droplets are formed in a 'conical spray '. This occurs at voltages of O(50V) and allows for continuous tuning of the droplet diameter from ≈ 5 to 50 μm at a fixed flow rate of the continuous phase.

To enhance EW effects and extend the functionalities of EW, we also designed and developed a simple, rapid and inexpensive method to fabricate an EW-based FFD based on the ultraviolet (UV) curable polymer NOA 81. This is described in **Chapter 5**. Using NOA 81 allows defining the channel geometry via soft imprint lithography, in addition to sealing of the device via exposure to UV light. This method allowed us to make microchannels with a better compatibility with oils, smaller dimensions, lower aspect ratios, and with electrodes on both the bottom and top surfaces of the channel. Furthermore, a reliable hydrophobization of the NOA 81 surface was achieved using a silanization treatment. We fabricated a FFD with an orifice of w × h (20 × 10 μm) to achieve more control and produce even smaller droplets (in the range ≈ 1 ~ 15 μm) as compared to chapter 4. We also fabricated a straight channel with a small aspect ratio (w × h: 200 × 15 μm). Using

EW to control the contact angles, this device allows imbibition of water into an initially oil-filled hydrophobic microchannel, from a water reservoir at zero excess pressure. This may be useful for the loading of microfluidic chips, which usually requires an overpressure on the injected liquid.

In **Chapter 6**, we demonstrate a microfluidic platform that can implement voltage programmable on-demand droplet formation and on-demand droplet merging. Two droplet injectors are integrated in close proximity on the same chip. EW-induced on-demand formation of droplets offers a means of synchronization of two streams of produced droplets. These two streams then meet at a T-junction, where interdigitated electrodes are embedded. Merging on demand (MOD) is achieved there via electrocoalescence (EC). The efficiency of MOD is 98 % based on hundreds of observations. Our device can be operated at relatively low voltages, for instance the minimum voltage required for merging is 20V. These capabilities could eventually be used in automated microfluidic chips for screening in various chemical or biology related applications.

One of the key parameters in the formation and stabilization of droplets is the interfacial tension of the oil (O) / water (W) interface. In **Chapter 7** we describe how this quantity can also be measured in microfluidic devices. Our new tensiometric device makes use of a tapered channel and control over the hydrostatic pressures of O and W. Since in such a channel the mean curvature of the interface depends on the axial position, mechanical equilibrium is achieved only at a certain axial location. This approach allowed to measure equilibrium IFTs between 3 and 38 mN/m. The measurements were found to correspond very well to those with other methods. Also a time dependent IFT varying from 37.5 mN/m to 18.5 mN/m could be measured using current device. Effects of contact angle hysteresis were studied by characterizing the advancing and receding angles. Also, the integration of EW into the system was explored.

To conclude, versatile microfluidic chips which combine EW technology and the droplet-based TPF platform have been successfully designed and developed using different approaches and microfabrication technologies. For several applications, the combination of the advantages of both EW and droplet-based TPF platform could indeed be realized. However, also some challenges still remain:

(i) One challenge is the fabrication of EW-based TPF devices for applications that require emulsification at an industrial scale. This is still complicated, because these devices must include not only microchannels, but also electrodes and insulators, each of these in large numbers because of the necessary parallelization. Even if all the individual modules work, their close proximity may still cause coupling effects. Also the sealing of large scale device could pose a main problem that needs to be solved.

(ii) EW-based droplet formation currently still suffers from a lack of quantitative insight, which is why droplet production phase diagrams are still being measured instead of predicted whenever a new device has been designed.

(iii) For EW-based TPF device, a conductive dispersed phase is needed. This is why only the W/O system and not the O/W system was studied in this thesis. A promising development however is that ionic liquids are finding more applications, also in the area of EW. This might offer a route to use EW-based TPF device in O/W or O/O systems.

Notwithstanding these challenges, it is already possible to perform real applications like cell screening, biochemical diagnosis, particles synthesis etc. using our EW-based TPF platform. These aspects indicate a way to extend this thesis work in the future.

Samenvatting

Electrowetting (EW)-gestuurde digitale microfluïdische systemen (DMF) en microfluïdische systemen met een op druppels gebaseerde twee-fasen stroming (TPF) door gesloten kanalen zijn de meest gangbare microfluïdische platformen. Over het algemeen worden deze systemen apart van elkaar gebruikt. Integratie van de twee technologieën zou echter de voordelen van beiden kunnen combineren: (i) een hoog debiet (van TPF) en (ii) nauwkeurige controle over elke afzonderlijke druppel (gebruikmakend van EW). Het doel van dit proefschrift was om de combinatie van EW technologie en een op druppels gebaseerd TPF platform te bestuderen. Hiertoe hebben we verschillende van zulke hybride microfluidische chips ontworpen en ontwikkeld, met gebruik van verschillende strategieën en microfabricatie technologieën. We hebben de nieuwe functionaliteiten van de ontwikkelde platforms aangetoond en hebben de fysische verschijnselen die hieraan ten gronslag liggen verkend.

In **Hoofdstuk 2** geven we een overzicht van de huidige inzichten in EW en digitale microfluïdica. We introduceren het principe van EW en de belangrijkste fysische aspecten die een rol spelen zoals de geleidbaarheid van de waterfase, contacthoekverzadiging en hysterese, en contactlijndynamica. Elk van deze aspecten is relevant voor de toepassing van microfluïdica. Vervolgens bespreken we de verschillende manipulaties van EW-gestuurde DMF, bestaande uit de vorming en het transport, opsplitsen, samenvoegen en mengen van druppels. In het tweede gedeelte van dit hoofdstuk bespreken we de recente ontwikkelingen op het gebied van op druppels gebaseerde TPF, waarbij we voornamelijk twee praktische aspecten benadrukken: vorming en samenvoeging van druppels door middel van zowel hydrodynamische als elektrische aansturing. Verder bediscussiëren we enkele veel gebruikte microfabricatie technieken voor TPF.

We hebben ervoor gekozen druppelvorming in een *flow focusing device* (FFD) te bestuderen omdat deze een erg reproduceerbare vorming van monodisperse druppels mogelijk maken. In **Hoofdstuk 3** bespreken we onze eerste FFD bestaande uit een polydimethylsiloxaan (PDMS) kanaalstructuur, die aan een met Teflon-AF bedekt indium tin oxide (ITO) glas substraat is gehecht. Gebaseerd op

onze experimentele bevindingen verkrijgen we een procesdiagram dat de vorming van waterdruppels beschrijft als functie van de water- en oliedrukken en de opgelegde (EW) spanning. In een specifiek gebied van het diagram worden druppels enkel gevormd ten gevolge van EW aansturing. De voorwaarden waaronder deze vergrootte controle over druppelvorming mogelijk is, zijn kwantitatief in overeenstemming met een theoretisch model dat de door EW opgewekte elektrostatische druk vergelijkt met de plaatselijke hydrostatische druk bij de stroomopening. In dit regime zijn de druppelgrootte en de druppelvormingsfrequentie onafhankelijk aan te passen door de amplitude en breedte van het spanningssignaal aan te passen. Verder beschrijven we gelijksoortige druppelvormingsfenomenen onder invloed van oppervlakteactieve stoffen.

Een andere mogelijke toepassing van EW in druppelvorming (voor toepassingen gerelateerd aan emulsificatie) wordt beschreven in **Hoofdstuk 4**. In dit onderzoek werd een geminiaturiseerd kanaal met een veel kleinere stroomopening (breedte × hoogte: 50 × 50 μm) gebruikt. In aanvulling op de drukken of de debieten van de gedispergeerde (water) en continue (olie) fasen wordt de EW spanning gebruikt als derde stuurparameter voor druppelvorming. Vergeleken met volledig hydrodynamische systemen blijken de EW-gestuurde systemen een breder en meer continu bereik van druppelgroottes mogelijk te maken. Bijzonder interessant was het regime waarin druppels gevormd worden in een "kegelvormige spray". Dit gebeurt bij O(50V) en maakt het mogelijk om de druppel diameter gecontroleerd te variëren tussen 5 en 50 μm bij een gegeven debiet van de continue fase.

Om de invloed van EW te vergroten en de functionaliteiten van EW uit te breiden, hebben we ook een eenvoudige, snelle, en goedkope methode ontworpen en uitgevoerd om een op EW gebaseerde FFD te maken uit het ultraviolet (UV) hardende polymeer NOA 81. Dit wordt beschreven in **Hoofdstuk 5**. Het gebruik van NOA 81 staat toe dat de kanaalgeometrie wordt gemaakt met zachte *imprint* lithografie waarna het systeem wordt afgesloten via blootstelling aan UV straling. Met deze methode kunnen we microkanalen maken die een betere compatibiliteit met oliën hebben, kleinere afmetingen, kleinere h/w verhoudingen, en elektroden aan zowel de onder- als bovenzijden van het kanaal. Een betrouwbare hydrofobisatie van het NOA81 oppervlak is verkregen door middel van een silanisatie behandeling. We hebben een FFD met een stroomopening met w × h (20

× 10 μm) gemaakt om meer controle te hebben over de druppelgrootte en kleinere druppels te kunnen maken (tussen≈ 1 ~ 15 μm) in vergelijking met Hoofdstuk 4. We hebben ook een recht kanaal gemaakt met een kleine h/w verhouding (w × h: 200 × 15 μm). Met gebruik van EW om de contacthoek te manipuleren, maakt dit systeem het mogelijk om de olie in een gevuld hydrofoob kanaal te vervangen door water dat zich in een reservoir zonder overdruk bevindt. Dit zou toegepast kunnen worden om microfluidische chips te vullen, die normaal gesproken een overdruk op de geïnjecteerde vloeistof nodig hebben.

In **Hoofdstuk 6** laten we een microfluïdisch platform zien welke spannings-gestuurde druppelvorming en druppelfusie op commando implementeert. Voor de vorming betekent dit dat er op een goed gedefinieerd moment een gecontroleerd aantal druppels wordt gegenereerd. Twee druppelinjectie systemen zijn dicht bij elkaar geïntegreerd in dezelfde chip. EW-gestuurde druppelvorming op commando geeft de mogelijkheid om twee druppel treinen te synchroniseren. Druppels uit de twee stromen komen dan samen bij een T-splitsing, waar in elkaar grijpende elektroden in de chip aangebracht zijn. Druppelfusie op commando (MOD) wordt hier geïnduceerd via electrocoalescentie (EC). De efficiëntie bereikt met MOD is 98%, gebaseerd op honderden observaties. Ons systeem werkt met relatief lage spanningen; de minimum spanning nodig voor druppelfusie is bijvoorbeeld 20V. Deze capaciteiten zouden uiteindelijk gebruikt kunnen worden in geautomatiseerde microfluïdische chips voor detectiedoeleinden in verschillende chemische en biologische toepassingen.

Eén van de bepalende parameters in de vorming en stabilisatie van druppels is de oppervlaktespanning (IFT) van het olie (O)/ water (W) scheidingsvlak. In **Hoofdstuk 7** beschrijven we hoe deze grootheid gemeten kan worden met behulp van microfluïdische systemen. Ons nieuwe tensiometrische platform maakt gebruik van een taps toelopend kanaal en sturing van de hydrostatische olie- en waterdrukken. Aangezien de gemiddelde kromtestraal van het scheidingsvlak in een dergelijk kanaal afhangt van de axiale positie, wordt mechanisch evenwicht pas bereikt op een zekere axiale locatie. Met deze aanpak waren we in staat evenwicht IFTs tussen 3 en 38 mN/m te meten. De metingen kwamen zeer goed overeen met die volgens andere methoden. Verder kon ook een tijdsafhankelijke IFT, afnemend van 37.5 mN/m tot 18.5 mN/m, gemeten worden met hetzelfde

platform. De effecten van contacthoekhysterese werden bestudeerd door de voortschrijdende en terugtrekkende hoeken te karakteriseren. Tot slot werd de integratie van EW in het systeem verkend.

We concluderen dat we met succes veelzijdige microfluïdische chips hebben ontworpen en ontwikkeld die EW technologie en een op druppels gebaseerde TPF combineren, met gebruik van verschillende strategieën en microfabricatie technologieën. Voor verschillende toepassingen kon inderdaad de combinatie van voordelen van zowel EW en een op druppels gebaseerd TPF platform worden gerealiseerd. Er blijven echter een aantal uitdagingen over:

(i) Een uitdaging is de productie van EW-gestuurde TPF platformen voor toepassing van emulsificatie op industriële schaal. Dit is nog steeds ingewikkeld omdat deze platformen niet alleen microkanalen moeten bevatten, maar ook elektroden en isolatoren, waarbij elk van hen in een groot aantal aanwezig moet zijn om de benodigde opschaling (parallellisatie) te verkrijgen. Zelfs als alle losse modules naar behoren werken, kan hun onderlinge nabijheid nog steeds tot gekoppelde effecten leiden. De afdichting van opgeschaalde platformen zou ook een belangrijk op te lossen probleem kunnen vormen.

(ii) EW-gestuurde druppelvorming wordt op dit moment kwantitatief maar beperkt begrepen. Hierdoor moeten druppelvorming fasediagrammen gemeten worden en kunnen ze niet voorspeld worden wanneer een nieuw systeem wordt ontworpen.

(iii) Voor een EW-gestuurd TPF platform is het nodig dat de gedispergeerde fase geleidbaar is. Dit is de reden dat alleen W/O systemen, en geen O/W systemen, zijn bestudeerd in dit proefschrift. Een veelbelovende ontwikkeling is echter dat ionische vloeistoffen steeds meer toegepast worden, mede voor EW. Dit zou een mogelijkheid kunnen bieden om EW-gestuurde TPF platformen te gebruiken voor O/W of O/O systemen.

Ongeacht deze uitdagingen is het al mogelijk om toepassingen zoals celonderzoek, biochemische analyses, deeltjessynthese, etc. uit te voeren met ons EW-gestuurde TPF platform. Deze aspecten geven een indicatie hoe dit proefschrift onderzoek in de toekomst uitgebreid kan worden.

Process Documents

I Fabrication of SU-8 mold

<table>
<tr><th>Step</th><th>Process</th><th>Parameters</th><th>Comments</th></tr>
<tr><td>1</td><td>Substrate
Silicon <100>
OSP P+</td><td>NL-CLR-Wafer Storage Cupboard
Orientation: <100>
Diameter: 100 mm
Thickness: 475 µm
Polished: Single side
Resistivity: 0.0015-0.019 Ωcm
Type: p</td><td>Type of silicon is not crucial. Other types also can be used for this purpose.</td></tr>
<tr><td>2</td><td>Cleaning
Standard</td><td>NL-CR-WB14
Standard Silicon wafer cleaning procedure
• beaker 1: fumic HNO_3 (99%), 5 min
• beaker 2: fumic HNO_3 (99%), 5 min
• Quick Dump Rinse > 12 MΩ
• beaker 3: boiling (95°C) HNO_3 (69%), 10 min
• quick Dump Rinse > 12 mΩ
• spin drying</td><td></td></tr>
<tr><td>3</td><td>Lithography - Dehydration bake SU-8</td><td>NL-CLR-WB24
• Hotplate
• Dehydration bake (120 °C): 10 min</td><td></td></tr>
<tr><td>4</td><td>Lithography - Coating SU-8 50</td><td>NL-CLR-WB24
• SüssMicroTec Spinner Delta 20 (30 sec)
<table><tr><th>Type</th><th>rpm</th><th>Thickness (µm) ±8%</th></tr><tr><td>SU-8 100</td><td>2000</td><td>200</td></tr><tr><td>SU-8 50</td><td>3000</td><td>50</td></tr><tr><td>SU-8 5</td><td>1000</td><td>13.6</td></tr></table></td><td>Real thickness of SU-8 mold in each case is 190 µm, 52 µm and 15 µm, separately.</td></tr>
</table>

<table>
<tr>
<td>5</td>
<td>Lithography - Prebake SU-8</td>
<td>NL-CLR-WB24
• Hotplate
<table>
<tr><th>Thickness (µm)</th><th>Baking</th></tr>
<tr><td>200</td><td>• 30 min @ 65 °C
• 90 min @ 95 °C</td></tr>
<tr><td>50</td><td>• 6 min @ 65 °C
• 20 min @ 95 °C</td></tr>
<tr><td>13.6</td><td>• 2 min @ 65 °C
• 8 min @ 95 °C</td></tr>
</table></td>
<td></td>
</tr>
<tr>
<td>6</td>
<td>Lithography - Alignment & Exposure SU-8</td>
<td>NL-CLR-EV620 Maskaligner
• Contact mode
<table>
<tr><th>Thickness (µm)</th><th>Time (s)</th></tr>
<tr><td>200</td><td>68</td></tr>
<tr><td>50</td><td>24</td></tr>
<tr><td>13.6</td><td>13</td></tr>
</table></td>
<td></td>
</tr>
<tr>
<td>7</td>
<td>Lithography - Post exposure bake SU-8</td>
<td>NL-CLR_WB24
Hotplate
<table>
<tr><th>Thickness (µm)</th><th>Baking</th></tr>
<tr><td>200</td><td>• 8 min @ 65 °C
• 18 min @ 95 °C</td></tr>
<tr><td>50</td><td>• 1 min @ 65 °C
• 5 min @ 95 °C</td></tr>
<tr><td>13.6</td><td>• 1 min @ 65 °C
• 3 min @ 95 °C</td></tr>
</table></td>
<td></td>
</tr>
<tr>
<td>8</td>
<td>Lithography - Development SU-8</td>
<td>NL-CLR-WB24
Developer: PGMEA (RER600, ARCH Chemicals)
• Time: 10 min for 200 µm, 3:30 min for 50 µm and 1 min for 13.6 µm with spray-gun
• Rinse with RER600</td>
<td></td>
</tr>
</table>

		• Rinse with IPA • Spin dry • Check result and perform extra cycles if not complete	
9	Lithography - Hard bake SU-8	NL-CLR-WB24 • Hotplate • 25 °C • 10 min @ 50 °C • 10 min @ 65 °C • 10 min @ 100 °C • 2 hrs @ 120 °C • 5 °C/10 min down to 25 °C	

II ITO Etching

Step	Process	Parameters	Comments
1	Substrate Commercial ITO glass	Supplier: Präzisions Glas & Optik GmbH www.pgo-online.com • Type: polished float glass substrate • Product code: CEC080P • Thickness of substrate: 0.4 mm • Thickness of ITO film: 25 nm • Surface resistivity: ≤80 Ω/cm • Diameter: 101.6 mm ± 0.25 mm	Etching time depends on thickness of ITO film
2	Cleaning HNO_3 99 %	NL-CLR-WB 9 or 10 • Removal of organic residue • Beaker : HNO_3 (99%) • Time: variable • Quick Dump Rinse <0.1 μS • Spin drying	
3	Lithography - Priming (liquid)	NL-CLR-Primus coater WB21 Hotplate 120 °C HexaMethylDiSilazane (HMDS) • Dehydration bake (120 °C): 5 min • Spin program: 4 (4000 rpm, 20 sec)	

4	Lithography - Coating Olin Oir 907-17	NL-CLR-WB21/22 • Primus spinner • Hotplate 95 °C • Olin 907-17 • Spin Program: 4 (4000 rpm, 20 sec) • Prebake (95 °C): 90 sec	
5	Lithography - Alignment & Exposure Olin OiR 907-17	NL-CLR- EV620 Electronic Vision Group 620 Mask Aligner • Hg-lamp: 12 mW/cm ^{2} • Exposure Time: 4 sec	
6	Lithography - Postbake Olin OiR resist	NL-CLR-Hotplate 120 °C WB21 • Time: 10 min	
7	Lithography - Development Olin OiR Resist	NL-CLR-WB21/22 • Developer: OPD4262 • Hotplate 120 °C • After Exposure Bake (120 °C): 60 sec Development: • Time: 30 sec in Beaker 1 • Time: 15 - 30 sec in Beaker 2 • Quick Dump Rinse > 10 MΩ • Spin drying • After development hard bake (120 °C):10 min	
8	Etching exposed ITO part	• Hydrochloric acid (HCl, 18%) • Time: ~3 min (check conductivity by multimeter and perform extra time of etching if needed) • Rinse with Milli-Q water • Dry by N_2 gun	In a general lab, not in the cleanroom
9	Dicing of the etched glass wafer	NL-CLR-Disco DAD dicing saw • Laminate of Nitto STW T10 dicing foil on glass wafer and wafer holder Parameters dicing: • Feed speed: 5 mm/sec • X, Y values: correspond respectively to Ch1 and Ch2 and those values are determined by mask layout	

		• Saw type TC300 • Select in blade menu: 2.187-12A Blade info: • Width: 300 um • Spindle revolutions: 25. 000 rpm	
10	Removing photoresist	• Rinse with acetone • Ultrasonic cleaning (acetone, 15min) • Dry by N_2 gun and ready for Teflon AF 1600 dip-coating	In a general lab

III Dip-coating of Teflon AF 1600

Step	Process	Parameters	Comments
1	Cleaning of substrates	• Ultrasonic cleaning in Milli-Q water with the detergent (1 mL Mucasol / 100 mL water) for 15 min • Ultrasonic cleaning in Milli-Q water successively for 3 times, each time 5 min • Ultrasonic cleaning in ethanol successively for 15 min • Ultrasonic cleaning in acetone successively for 15 min • Ultrasonic cleaning in isopropanol (IPA) successively for 15 min • Rinsing with milli-Q water and IPA • Drying by N_2 gun	During ultra-sonic cleaning, the beaker was covered by aluminum foil to prevent contamination.
2	Dip-coating	• Cleaning the container with perfluorinated solvent (FC-75) and then drying by N_2 gun • Filling 6 % Teflon AF 1600 in the container Dip-coater setting: • Speed up: 3 (15 cm/min) • Speed down: 5 (25 cm/min) • Travel distance: 3.2 cm (depends on the length of substrate) Note: in this case, thickness of Teflon AF layer is 3.2 μm.	The thickness of Teflon AF layer mainly depends on speed-up.

3	Baking	Baking in an oven • 15 min @ 110 °C • 15 min @ 160 °C • 30 min @ 340 °C (under vacuum) • Switching off the oven to let substrates cool down to room temperature	

Acknowledgements

After four and half years of my PhD study in the Physics of Complex Fluids group at the University of Twente in the Netherlands, my thesis has been finished. I would like to express my sincere gratitude to everyone who helped me along the way, professionally and personally. Without your support and encouragement, it would not have been possible.

First of all, I would like to thank my promotor, Prof. Frieder Mugele, for offering me the opportunity to pursue my PhD study in PCF group. I really appreciate for giving me the freedom and the trust to follow my own ideas and the guidance necessary to bring those ideas come to fruition. I learned a lot from your broad knowledge and attitude in scientific researches.

I am also grateful to Dr. Michel H. G. Duits who is my daily supervisor for the last one and half year of my PhD study. Dear Michel, we have regular work discussion almost every week. Also you are always available for discussion when I just pop in your office. Thank you very much for helping me in the lab work and in writing the articles. You gave me a lot of active suggestions in the research.

In the first and second years of my PhD, I had the opportunity to work with Dr. Florent Malloggi and Dr. Siva A. Vanapalli. Dear Florent, thank you very much for your continuous support for my lab work and the amount of time you spent on the discussion. Dear Siva, you always have innovative ideas for science, I really appreciate your suggestions for my research during our discussion.

I am really lucky to meet all nice colleagues in the PCF group who make my stay in PCF group a wonderful memory. Annelies, thank you for all your kind help in the administrative work. Dirk, I appreciate your suggestions for my research during the discussion. Chandra and Daniel, thanks for helping me in the lab (cleanroom) work. I would also like to thank my former and present office mates: Eko, Jane, Olga, Pablo, Omkar, Daniel, Agata and Dhirendra. We have shared a lot of joyful time together. My appreciations are also extended to Burak, Dileep, Mariska, Dieter, Jolet, Rielle, Sisi and Jung. I am especially grateful to Jolet and

Dieter for accepting to be my paranimfen. I'd also like to thank Jolet for translating my Summary into Samenvatting. Last but not least, I want to express my thanks to all the former PCF members for the supports and accompany during coffee breaks and outings especially Adrian, Helmut and Gor (we played football games a lot around two years ago. I really enjoy that time), Cock, Fahong, Arun and Tarun.

Besides that, I also would like to thank my collaborators. Kevin, thanks for teaching me to fabricate SU-8 device. Lingling, thanks for the assistance in designing the chip holder although I did not use it successfully with my work. Wim, I am indebted to you for helping me to use Matlab and also super high speed camera.

I would like to thank all the friends I met during my stay in Enschede, who help me a lot and shared a lot of wonderful and important moments with me. Piet and Janny, Carel and Kicki, I really cherish your presence at my wedding in China! Tian and Xin, being friends and neighbors we have so much fun together! For In Yee and Xing Yi, our trips to Greece and Berlin were great! Zheng and Xiao, distance is never a problem for friendship. Jing, Weihua and Qiwei, Qi and Yujie, Chien-Ching and Kaifan, Priscilla and Ype, Wei and Wei, Sinie, Shan and Yuguo, Rui, Hongmei, Jung Seok and the family, Chunlin, Weiqing, and many others, we had a lot of enjoyable time together and thank you all for your friendship!

I would like to thank all the other promotion committee members who read the thesis and provide me valuable advices. My acknowledgement also go to the MicroNed programme from Dutch government for financial support, as well as the research institutes IMPACT and MESA+ at Twente University.

Finally and most importantly, I would like to thank all my family members. I express my deepest gratitude to my grandmother Tang Caixian, my parents Gu Youjian and Zhang He, and my beloved wife Yang Lanti and daughter Gu Yuehan for their endless love, support and encouragement.

Hao Gu

February, 2011

Publications

Related to this thesis

Peer Reviewed Publications

H. Gu, C.U. Murade, M.H.G. Duits, F. Mugele, "A microfluidic platform for on-demand formation and merging of individual droplets using electric control", Biomicrofluidics, in press

H. Gu, M.H.G. Duits, F. Mugele, "A hybrid microfluidic chip with electrowetting functionality using ultraviolet (UV)-curable polymer", Lab on a Chip, **10**, 1550 (2010)

H. Gu, F. Malloggi, S.A. Vanapalli, F. Mugele, "Electrowetting-enhanced microfluidic device for drop generation", Applied Physics Letters, **93**, 183507 (2008)

F. Malloggi, H. Gu, A.G. Banpurkar, S.A. Vanapalli, F. Mugele, "Electrowetting – A versatile tool for controlling microdrop generation", The European Physical Journal E, **26**, 91 (2008)

F. Malloggi, S.A. Vanapalli, H. Gu, D. van den Ende, F. Mugele, "Electrowetting-controlled droplet generation in a microfluidic flow-focusing device", Journal of Physics: Condensed Matter, **19**, 462101 (2007)

H. Gu, M.H.G. Duits, F. Mugele, "Droplet in two-phase flow microfluidics", International Journal of Molecular Sciences, submitted (invited review)

H. Gu, M.H.G. Duits, F. Mugele, "Interfacial tension measurement with microfluidic tapered channel", in preparation

Conference Proceeding

H. Gu, M.H.G. Duits, F. Mugele, "Controlled drop generation for digital microfluidic systems by means of electrowetting", Proceeding of the 14th international conference on micro total analysis systems, 2010, 1808-1810.

About the author

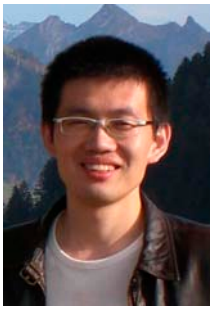

Hao Gu was born on June 11, 1979 in Beijing, P. R. China. After graduating from Beijing Jingshan School, he entered the Chemistry and Chemical Engineering Department, Shanghai Jiao Tong University in 1997. In 2001, he obtained his Bachelor's degree and then started working as sales engineer in Shanghai until 2003. After that, he decided to study abroad and later obtained his MSc degree under the supervision of Prof. Johan Engbersen in the Polymer Chemistry & Biomaterials group, University of Twente in 2006. From Sep. 1st 2006, he started his PhD studies in the group of Prof. Frieder Mugele, University of Twente, the Netherlands. His PhD work focused on the development of a novel concept of hybrid microfluidic chips which combines the strengths of pressure-driven channel-based microfluidics with the unique control possibilities offered by electrowetting-based discrete microfluidics. The results of his research are described in this thesis.